Distribution Agreement

In presenting this thesis or dissertation as a partial fulfillment of the requirements for an advanced degree from Emory University, I hereby grant to Emory University and its agents the non-exclusive license to archive, make accessible, and display my thesis or dissertation in whole or in part in all forms of media, now or hereafter known, including display on the world wide web. I understand that I may select some access restrictions as part of the online submission of this thesis or dissertation. I retain all ownership rights to the copyright of the thesis or dissertation. I also retain the right to use in future works (such as articles or books) all or part of this thesis or dissertation.

Signature:

_____ _____

Weijie Li Date

Interacting Excitons and Electrons in van der Waals Heterostructures

Weijie Li
Doctor of Philosophy

Phyiscs

Ajit Srivastava, Ph.D.
Advisor

Justin C. Burton, Ph.D.
Committee Member

Hayk Harutyunyan, Ph.D.
Committee Member

Tianquan Lian, Ph.D.
Committee Member

Sergei Urazhdin, Ph.D.
Committee Member

Accepted:

Kimberly Jacob Arriola, Ph.D.
Dean of the James T. Laney School of Graduate Studies

Date

Interacting Excitons and Electrons in van der Waals Heterostructures

By

Weijie Li
B.S. University of Science and Technology of China, 2017

Advisor: Ajit Srivastava, Ph.D.

An abstract of
A dissertation submitted to the Faculty of the
James T. Laney School of Graduate Studies of Emory University
in partial fulfillment of the requirements for the degree of
Doctor of Philosophy
in Phyiscs
2023

ABSTRACT

Layered materials, such as 2D semiconducting transition metal dichalcogenide (TMD), have garnered tremendous excitement for investigating physics in two dimensions. Photoexcitations in TMDs—excitons, can provide deep insights into the rich electronic properties of the host crystals. In this dissertation, we explore the interplay among excitons and electrons in TMD based van der Waals heterostructures. These low-dimensional systems have been shown to enhance few-body and many-body interactions among excitons, electrons, and exciton-electron mixture. To study these interactions, we focus on optical excitations in TMD heterostructures, viz. interlayer excitons (IXs), where electrons and holes are spatially separated into different layers due to type-II band alignment, giving rise to a permanent out-of-plane dipole moment. We observed dipole-dipole repulsive interaction-induced single photon nonlinearity for localized IXs in $WSe_2/MoSe_2$[1]. Furthermore, at large exciton densities, we observed many-exciton exchange interaction-induced out-of-equilibrium magnetic field, which enables optical control of valley Zeeman splitting[2].

In addition, in an electron-doped TMD heterostructures, the interactions between electrons and localized IXs allow for local sensing of electron distribution. We used localized IXs to optically probe the charge orders of correlated electronic states in TMD heterostructures $WSe_2/MoSe_2/WSe_2$ with a high spatial resolution ($\sim$10 nm)[3]. More recently, we observed a new quasiparticle in a heterotrilayer ($WS_2/WSe_2/WS_2$)—quadrupolar exciton, a superposition of oppositely orientated dipolar IXs. We further observed quadrupolar to dipolar IX transition involving the modification of its internal structure, through electric field and many-body interactions[4]. This series of works related to dipolar IXs reveal the rich physics of interactions in TMD van der Waals heterostructures.

Interacting Excitons and Electrons in van der Waals Heterostructures

By

Weijie Li
B.S. University of Science and Technology of China, 2017

Advisor: Ajit Srivastava, Ph.D.

A dissertation submitted to the Faculty of the
James T. Laney School of Graduate Studies of Emory University
in partial fulfillment of the requirements for the degree of
Doctor of Philosophy
in Phyiscs
2023

ACKNOWLEDGEMENT

First and foremost, let me thank my advisor Prof. Ajit Srivastava who teach me how to conduct research on physics and how to think as a physicist. He discusses physics with me everyday and introduces me to the rich universe of condensed matter physics. It is lucky for me to have such an erudite as my advisor, from whom I also know hard work will pay off. Our research field is very competitive and himself works hard to produce fantastic results. With the strict training in our lab, I have the confidence to become an outstanding researcher in the future.

Next, particular thanks go to Dr. Xin Lu for her patience in teaching me how to do experiments and act mentally strong against experimental failures. It has been a hard time for me to adapt myself into the working style of our lab. She helped me a lot during the process. I could not have become an independent researcher at the end of my PhD without her help. I also want to thank my colleagues Dr. Sudipta Dubey, Dr. Xiaotong Chen, Qiang Yao, Luka Devenica, and talented undergradutes Zach Hadjri, Jiatian Wu, Tony Li, who have constituted important parts of my research daily life.

In addition, I would like to thank Prof. Sergei Urazhdin who let me know strong mind and perseverance are required for finding new physics. I am thankful that Prof. Justin Burton and Prof. Hayk Harutyunyan give me good examples to simultaneously do good science and service for the department or the public. I would also like to thank Prof. Tim Lian for his scientific rigor, which let me revisit my research and deepen my understanding.

Moreover, I would like to thank Prof. Luiz Santos for the profound discussion about condensed matter theory as well as theoretical collaborators Prof. Ángel Rubio, Dr. Jin Zhang, and Dr. Yang Zhang. Discussion with people in other groups is very important to solve my research problem. Likewise, I would like to thank Dr. Patrick Knüppel, Dr. Jie Gu, Dr. Zhurun Ji and Dr. Xi Wang, from whom I learned a lot.

Besides, I would like to thank my roommates Wei Li, Qihan Liu and Jian Wang. We had interesting discussions about life, work and the world everyday. I feel fortunate to have senior PhD students Dr. Yixuan Han, Dr. Guanxiong Chen, Dr. Chentao Li, Dr. Wenxuan Xu and Dr. Yonglun Jiang to help me when I came across problems in my daily life and make my life much easier.

Furthermore, I would like to thank my middle school teacher Mrs. Xiaohui Zeng, who taught me to be confident and strong mind. With her encouragement, I formed my personality to overcome the difficulties and pursue my dream to become a scientist.

Last but not least, I would like to thank my parents, my little sister and my wife Ruoming Zhang for their unconditional support and love.

It has been a long and fruitful march for me to finish the PhD and luckily I have arrived at the milestone with the help of my colleagues, friends, and family.

LIST of PUBLICATIONS

[1] **Weijie Li**, Zach Hadjri, Luka M Devenica, Jin Zhang, Song Liu, James Hone, Kenji Watanabe, Takashi Taniguchi, Angel Rubio, and Ajit Srivastava. Quadrupolar excitons in a tunnel-coupled van der Waals heterotrilayer. *arXiv preprint arXiv:2208.05490*, 2022.

[2] **Weijie Li**, Luka M Devenica, Jin Zhang, Yang Zhang, Xin Lu, Kenji Watanabe, Takashi Taniguchi, Angel Rubio, and Ajit Srivastava. Local sensing of correlated electrons in dual-moiré heterostructures using dipolar excitons. *arXiv preprint arXiv:2111.09440*, 2021.

[3] **Weijie Li**, Xin Lu, Jiatian Wu, and Ajit Srivastava. Optical control of the valley Zeeman effect through many-exciton interactions. *Nature Nanotechnology*, 16(2):148–152, 2021.

[4] **Weijie Li**, Xin Lu, Sudipta Dubey, Luka Devenica, and Ajit Srivastava. Dipolar interactions between localized interlayer excitons in van der Waals heterostructures. *Nature Materials*, 19(6):624–629, 2020.

[5] Xin Lu, Xiaotong Chen, Sudipta Dubey, Qiang Yao, **Weijie Li**, Xingzhi Wang, Qihua Xiong, and Ajit Srivastava. Optical initialization of a single spin-valley in charged WSe_2 quantum dots. *Nature nanotechnology*, 2019.

[6] Sergei Urazhdin, **Weijie Li**, and Lydia Novozhilova. Magnetic freezing transition in a CoO/permalloy bilayer revealed by transverse ac susceptibility. *Journal of Magnetism and Magnetic Materials*, 476:75–85, 2019.

[7] Wenting Zhang, Yue Lin, Qi Wang, **Weijie Li**, Zhifeng Wang, Jiangluqi Song, Xiaodong Li, Lijie Zhang, Lixin Zhu, and Xiaoliang Xu. Well-hidden grain boundary in the monolayer MoS_2 formed by a two-dimensional core–shell growth mode. *ACS nano*, 11(10):10608–10615, 2017.

ABBREVIATIONS

3D: Three-dimensional

2D: Two dimensional

vdW: van der Waals

ML: Monolayer

BL: Bilayer

TMD: Transition metal dichalcogenides

hBN: Hexagonal boron nitride

CW: Continuous-wave

IX: Interlayer excitons

IXX: Interlayer biexcitons

LIX: Localized interlayer excitons

PL: Photoluminescence

PDMS: Polydimethylsiloxane

PC: Polycarbonate

CCD: Charge-coupled device

DFT: Density-functional theory

SOC: spin-orbital coupling

Contents

List of Figures

List of Tables

Chapter 1

Introduction

In the physical world, we perceive in two relevant aspects: one is dimensionality and the other one is scale. Dimensionality of objects can be classified into zero-, one-, two-, and three-dimensional. We know that a point is 0D, a line is 1D, a surface is 2D and anything touchable in daily life is 3D. For scale, it is known that dust is small and universe is large. They are relevant in the sense that we can consider dust as a 0D point in the scale of universe, however, if we zoom into the dust using a microscope, we can find it has complicated structures and is indeed a 3D particle. This is the same case for the 2D surface of any object, which has fine structures while zoomed in. This implies that we need to define a basis of scale to study the properties of objects and related physical laws, as different physical laws dominate at different scales. For the scale as large as the universe, gravity is very important to study while it is ignored at small scales. In contrast, quantum phenomena, which apparently disappear at large scales start to be dominant at small scales. In order to study quantum phenomena in solid state platform, researchers have tried to make nanometer scale (10^{-9} m) materials since last century. They successfully fabricated quantum dots (quasi-0D), quantum wires (quasi-1D) and thin film of single crystals (quasi-2D). It should be noted that the "quasi-" comes from the fact that it does not

reach the atomic limit (sub-nanometer), which is the smallest scale in the study of solid-state physics.

Further development occurred a decade ago, wherein a humble adhesive tape was the main contributor, by exfoliating a 3D bulk crystal (graphite) into an atomic 2D monolayer (graphene), reaching the real 2D limit. This dissertation focuses on such atomically thin materials. Besides the quantum phenomena manifested at the nanometer scale, with the reduced dimensionality and thus reduced screening, real 2D materials have enhanced interactions between particles in the system. Furthermore, due to the reduced volume, the electric/magnetic field and carrier density in the system can be easily modified, which therefore easily tune the interactions – another strength of 2D materials. With strong and tunable interactions in 2D materials, they have consequently become an ideal platform to study interactions – the most important theme of current physical research. In the past few years, it was discovered that interactions are further enhanced with stacked 2D materials—twist moiré heterostructures [6]. In the 2D heterostructure, small twist angle or lattice mismatch between the two layers generates periodically modulated potential—moiré potential with a period of $\sim$10 nm. This long period potential compared to lattice constant (sub-nm) suppresses the kinetic energies of particles and manifests the interactions between them, which gives rise to strongly correlated electronic states, for example, Mott insulator and superconductivity [7, 8]. Those states have similar phase diagrams as cuprates, well known as high-temperature superconductors, which could lead to insights into the physics behind them.

The methods to probe the properties of 2D materials can be either electrical or optical, depending on the bandgap. For a 2D metal or semimetal without bandgap, electrical measurements are commonly used to study strongly correlated electronic states. However, for a 2D semiconductor with a bandgap, optical measurements are preferred as the Schottky barrier prevents good electrical contact. Optical excitations

create an excited quasiparticle called exciton in 2D semiconductors, comprised of a negatively charged electron and positively charged hole. The exciton is like a hydrogen atom in the 2D semiconductor with a large binding energy (0.5 eV). It has corresponding Rydberg states and contains material information such as band structures.

The main theme of this dissertation is to study exciton related interactions by their optical response. Similar to hydrogen atoms, excitons can have interactions between each other, including spin-independent dipolar interactions (Chapter 4) and spin-dependent exchange interactions (Chapter 5). As two hydrogen atoms can hybridize to form a molecule, two excitons can form hybridized excitonic states—quadrupolar excitons by tunneling of their constituents (electron or holes) (Chapter 7). Besides the similarity between hydrogen atoms and excitons, the main difference between them is that the excitons are driven-dissipative systems while hydrogen atoms are stable systems. It should also be noted that doping electrons or holes into the 2D semiconductors is much easier than into the atoms, which makes exciton a good candidate to study fermion-boson interactions, i.e., electron-exciton interactions in our system (Chapter 6).

1.1 Scope of the Dissertation

In this dissertation, we will show how optical spectroscopy along with nano-fabrication plays a powerful role in studying exciton-exciton interactions, exciton-electron interactions as well as hybridized excitons in 2D materials, as structured below:

Chapter 2 is a basic introduction to the properties of the van der Waals semiconductor family, specifically transition metal dichalcogenides (TMDs), including WSe_2, $MoSe_2$, WS_2 and etc. I will first introduce the monolayer TMD and then TMD heterostructures.

Next, I will introduce the experimental techniques for sample fabrication and optical measurements in Chapter 3, which are the bases of all the observations.

Chapter 4 will introduce the observation of single-photon nonlinearity due to dipolar interactions in $WSe_2/MoSe_2$ heterobilayer. We find the presence of a single excitation results in energy shifts far exceeding the linewidth of quantum emitters. This quantifies the on-site Hubbard interaction (U) which is important for quantum simulation of Bose-Hubbard models. First, the optical measurements identify the existence of the localized interlayer excitons (IXs) by excitation resonance and electric field tunability. Next, with increased incident excitation power, the optical spectra show the presence of the first exciton (photon) increases the second exciton (photon) energy in the same trap by 2 meV, which is the repulsive dipolar interaction energy between them and one order of magnitude larger than linewidth. This strong on-site nonlinearity of photons in 2D semiconductors instead of cold atom systems is firstly demonstrated by our research.

In Chapter 5, I will introduce the observation of many-body interactions amongst optical excitations, which leads to an effective magnetic (exchange) field in a bosonic system in $WSe_2/MoSe_2$ heterobilayer. In TMDs, the degenerate energy extrema in momentum space can be labeled as another degree of freedom, valley pseudospin, which can couple to circularly polarized light. The IXs in the valley coupled to circularly polarized light, have higher density and higher energy, compared to those in the opposite valley. The magnitude of Zeeman splitting between two valleys increases with power and saturates at 4 meV corresponding to 6 Tesla magnetic field. This can be explained by that the exchange interactions between the excitons in the same valley are repulsive and raise their energy, due to the fermionic nature of the exciton constituents (electrons and holes). This research firstly proves the effective spin-spin interactions between bosons in a driven-dissipative system, which is a necessary ingredient for quantum magnetism. It paves the way for the dynamical optical generation

of the effective magnetic field up to several tesla under low continuous-wave incident power within exciton lifetime (nanoseconds).

Chapter 6 describes another aspect of the interactions, which is the interactions between electrons and excitons. These interactions enable the optical detection of correlated electrons in 2D heterostructures with moiré-based quantum sensors in an all-2D platform ($WSe_2/MoSe_2/WSe_2$ heterotrilayer). To fabricate high-quality samples, I was engaged in building the pick-up setup placed inside the glovebox. I will introduce how to use the setup to stack the $WSe_2/MoSe_2/WSe_2$ heterotrilayer with the dual gates and contact, where I observed stable localized interlayer exciton PL emission with instrument limited linewidth. With doped electrons into the sample, reproducible correlated red- and blue-shifts of the exciton energies are observed across the whole sample at rational fractional fillings. It is because the correlated electron lattice reconfigures at certain electron filling fractions. The reconfiguration changes the surrounding electrons near the exciton and electron-dipole interaction energy accordingly. Classical Monte Carlo simulation shows qualitatively similar features to the experiments. Since the localized IXs are in the length scale of 10 nm, this gives high resolution sensing of the electron lattice with sampling technique, instead of scanning the whole sample. Another feature of the localized IXs is that the degree of circular polarization (DCP) of emission is enhanced by as small magnetic field as $\sim$mT, useful to detect local small magnetic field. This research establishes a method to detect exotic phases and their dynamics.

Chapter 7 is about my most recent research, where we observe quadrupolar exciton to dipolar exciton transition, which involves the modification of internal structure of excitons, through electric field and many-body interactions. The creation of quadrupolar excitons is achieved in $WS_2/WSe_2/WS_2$ heterotrilayer through a quantum superposition of oppositely oriented dipolar excitons, where the electron wavefunction are layer-hybridized between two WS_2 layers while the hole is localized in

WSe_2 layer. With high out-of-plane electric field or high quadrupolar exciton densities, the nonlinear Stark shift of quadrupolar excitons becomes linear, signaling a transition to dipolar excitons. This research explores a new route for the exciton wavefunction engineering in van der Waals heterostructures.

Chapter 8 is a short summary and outlook to the whole dissertation, which lists a few of the challenges we all face and possibly suggest 2D materials as a good platform to solve them.

Chapter 2

VdW Semiconductors: Background

This chapter describes the important optical and electronic properties of group-VI transition metal dichalcogenides (TMD) semiconductors—the most notable van der Waals (vdW) semiconductor from theoretical and experimental aspects.

2.1 Monolayer Semiconductors–Transition Metal Dichalcogenides

TMDs have emerged as a highly attractive platform for fundamental physical research and applications owing to their abundant properties. TMDs have a chemical formula of MX_2, where M is a transition metal atom and X is a chalcogenide atom (sulfur (S) or selenium (Se), or Tellurium (Te)). There are more than 60 types of TMD compounds, depending on the selection of transition metal atoms and chalcogenide atoms[9]. More than 40 of them have layered structures, which have strong intralayer covalent bonds and weak interlayer vdW force (scaled as $\sim 1/r^6$), a typical feature of vdW materials (a similar example is graphite or hexagonal boron nitride (hBN)). This allows for exfoliation by adhesive tapes to be thin films or monolayers. Due to the diversity of the TMD vdW materials, we can have 2D TMDs with distinct electronic properties,

such as $NbSe_2$ with superconducting states, WTe_2 with ferroelectric states, TaS_2 with charge density wave and semiconductor MoS_2 with strong light-matter interactions. As an optics group, we are interested in semiconducting group-VI monolayer (ML) TMDs with an optical bandgap (M is Molybdenum (Mo) or Tungsten (W)), including $MoSe_2$,WSe_2, MoS_2 and WS_2. Although the above four TMDs have two X atoms to be the same, the two X can be different chalcogenide atoms. The TMDs with such a structure are called Janus TMDs[10], beyond the scope of this dissertation. Hereafter, we refer TMDs to the group-VI TMDs in this dissertation.

2.1.1 Lattice structure of ML TMDs

In order to understand the properties of ML TMDs, we start with their lattice structure. TMDs have two common lattice structures: 2H and 1T crystal phases. In the 2H phase, two chalcogenide atoms in different atomic planes align to each other perpendicular to the layer (ABA), forming a trigonal prismatic unit cell of M and two X atoms (Fig. 2.1a). In contrast, two chalcogenide atoms in the 1T phase are located at different positions relative to the metal atom (ABC), arranged in distorted octahedral coordination (Fig. 2.1b). We focus on the 2H TMDs $MoSe_2$,WSe_2 and WS_2, which are thermodynamically stable compared to their 1T phases. For the monolayer 2H TMDs with a hexagonal lattice in Fig. 2.1a, it has mirror symmetry σ_h (the metal atom plane as the mirror) and 3-fold rotation symmetry (120° rotation using the metal atoms/chalcogenide atoms/hexagonal centers as the rotation centers and perpendicular to the plane as the axis) without inversion symmetry, i.e., D_{3h} point group. If we consider a 2H TMD bilayer, it possesses inversion symmetry resulting from the 180° rotation between the adjacent layers (D_{3d} point group) as shown in Fig. 2.1c. The hexagonal lattice of monolayer TMDs with different atoms at A, B sites leads to a hexagonal reciprocal lattice with inequivalent Brillouin zone corners labeled as K and K' in the momentum space (k space) (Fig. 2.1d).

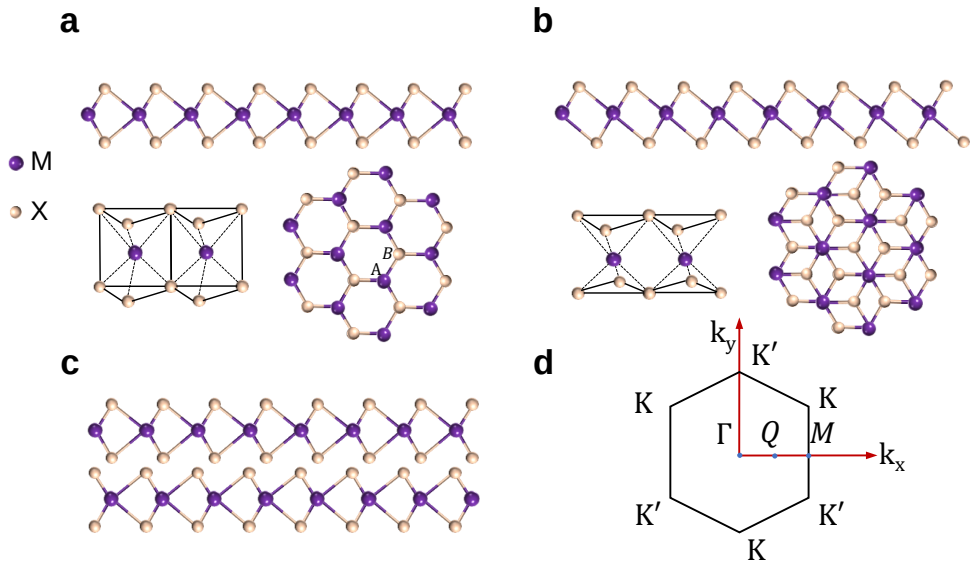

Figure 2.1: ML TMD lattice structure. **a-b.** Side view and top view of 2H phases **(a)** and 1T phases **(b)**. **c.** Side view of a 2H bilayer. **d.** Brillouin zone of ML 2H TMDs in the momentum space.

2.1.2 Electronic structure of ML TMDs

For the electronic structure, the different masses of M and X atoms at A, B sites induce a bandgap between the conduction band and valence band. This can be understood by the tight-binding model of the hexagonal lattice with two atoms per unit cell. To begin with, the lattice periodicity and Bloch theorem tell us that the real space wavefunction of the whole crystal lattice can be written as

$$\psi_{\mathbf{k}}(\mathbf{r}) = \sum_m \frac{e^{i\mathbf{k}\cdot\mathbf{R}_m}}{\sqrt{N}}[c_A(\mathbf{k})e^{i\mathbf{k}\cdot\mathbf{d_1}}\phi_A(\mathbf{r}-\mathbf{R_m}-\mathbf{d_1}) + c_B(\mathbf{k})e^{i\mathbf{k}\cdot\mathbf{d_2}}\phi_B(\mathbf{r}-\mathbf{R_m}-\mathbf{d_2})] \tag{2.1}$$

where $\mathbf{R_m}$ is the unit cell coordinate and $\mathbf{r}$ is the electron position. $\mathbf{d_1}$ and $\mathbf{d_2}$ are the two atom coordinates relative to the unit cell center. ϕ_A and ϕ_B are the atomic orbitals. The part in the bracket is the real space wavefunction in each unit cell

called Wannier function. If $\begin{pmatrix} c_A(\mathbf{k}) \\ c_B(\mathbf{k}) \end{pmatrix}$ is the eigenvector and only nearest neighbors are considered, the tight-binding Hamiltonian is written as

$$\mathcal{H}(\mathbf{k}) = \begin{pmatrix} E_A & -Vf(\mathbf{k}) \\ -Vf^*(\mathbf{k}) & E_B \end{pmatrix} \tag{2.2}$$

where E_A, E_B are the self-energy of A, B atoms, relevant to the mass of the atoms. V is relevant to the overlap (or hopping integral) between electron wavefunction at A, B sites. The relative phase between the A, B atoms is described by $f(\mathbf{k})$ and its Hermitian conjugate $f^*(\mathbf{k})$, with $f(\mathbf{k}) = e^{i\mathbf{k}\cdot\mathbf{n_1}} + e^{i\mathbf{k}\cdot\mathbf{n_2}} + e^{i\mathbf{k}\cdot\mathbf{n_3}}$. $\mathbf{n_1}, \mathbf{n_2}, \mathbf{n_3}$ are the real space unit vectors:

$$\begin{aligned} \mathbf{n_1} &= \frac{a}{\sqrt{3}}\hat{\mathbf{x}}, \\ \mathbf{n_2} &= \frac{a}{\sqrt{3}}(-\frac{1}{2}\hat{\mathbf{x}} + \frac{\sqrt{3}}{2}\hat{\mathbf{y}}), \\ \mathbf{n_3} &= \frac{a}{\sqrt{3}}(-\frac{1}{2}\hat{\mathbf{x}} - \frac{\sqrt{3}}{2}\hat{\mathbf{y}}). \end{aligned} \tag{2.3}$$

The lattice constant a of the monolayer TMDs is about 0.319-0.356 nm. The band structure of the tight-binding model for the periodic lattice, viz, the Bloch band, is calculated to have both conduction band minimum (CBM) and valence band maximum (VBM) at the K or K' points with a bandgap of $|E_A - E_B|$ (Fig. 2.2a). In ML TMDs, different masses of A, B atoms induce such a bandgap, compared to gapless graphene with same A, B atoms. In other words, we can consider TMDs as gapped graphene appropriate for optical measurements.

More realistic DFT calculation of its band structure involving more bands and orbital contributions is shown in Fig. 2.2b[11]. The CBM is at K point mainly contributed from transition metal d_{z^2} orbital whereas the VBM is also at K point mainly

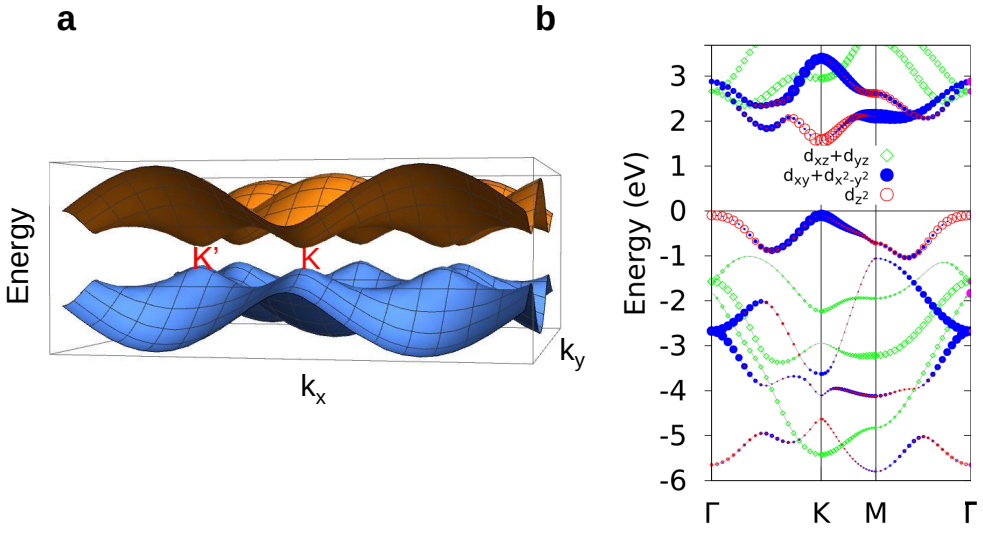

Figure 2.2: ML TMD band structures. **a.** Tight-binding model calculated bands. The yellow (blue) energy landscape is the conduction (valence) band. **b.** DFT calculated bands adapted from Ref.[11].

contributed from the transition metal $d_{xy} + d_{x^2-y^2}$, consistent with the direct bandgap picture from the tight-binding model. This direct bandgap of 1.7-2 eV enables high radiative recombination, that is, photoluminescence (PL) emission, in the visible to near-infrared range, so PL measurements are powerful tools to measure its properties. Contrasted to monolayer TMDs, thin TMD films with two or more layers, the CBM lies at the Q point and the VBM lies at the Γ point. The momentum mismatch between the CBM and VBM requires an additional phonon scattering process for the PL emission process to satisfy the momentum conservation. Therefore, the bilayer and thicker TMDs have much weaker PL compared to the monolayer.

2.1.3 Valley physics in ML TMDs

As both the CBM and VBM are located at either K or K' points, the low energy physics is determined by physical properties near K and K' points, which we call "valley physics". Two inequivalent valley indices K and K' are related through time-

reversal operation, since they are opposite momentum ($k \xrightarrow{\mathcal{T}} -k$). Without external magnetic field, time-reversal symmetry requires $E_\uparrow(K) = E_\downarrow(K')$. Due to the broken inversion symmetry in the monolayer TMDs, the nonzero crystal electric field with the intrinsic strong spin-orbit-coupling (SOC) of the transition metal atom d orbitals cause spin splitting ($E_\downarrow(K) \neq E_\downarrow(K')$)[12, 13]. The energy splitting ($E_\uparrow(K) - E_\downarrow(K)$) between the two conduction (valence) bands is about tens (hundreds) of meV. The large splitting between the two valence bands with opposite spins enforces the low energy state in K (K') valley to be spin-up (down), so-called spin-valley locking.

To shed insight into the valley physics, we expand the tight-binding Hamiltonian around K or K' valley ($\mathbf{k} = \pm\mathbf{K} + \mathbf{k}$), which dictates the two-band $k \cdot p$ effective Hamiltonian as below[14]:

$$\mathcal{H}(\mathbf{k}) = \begin{pmatrix} \Delta/2 & at(\tau k_x - ik_y) \\ at(\tau k_x + ik_y) & -\Delta/2 \end{pmatrix} = \begin{pmatrix} \Delta/2 & atke^{-i\tau\phi_k} \\ atke^{i\tau\phi_k} & -\Delta/2 \end{pmatrix} \tag{2.4}$$

where $\Delta = (E_A - E_B)$, t is the effective hopping integral. $\tau = \pm 1$ is the valley index, $k = \sqrt{k_x^2 + k_y^2}$, and $\tan\,\phi_k = \frac{k_y}{k_x}$. The eigenvalue of the Hamiltonian is $\varepsilon(k) = \pm\sqrt{\Delta^2 + a^2t^2k^2}$, where - is the valence band and + is the conduction band. The eigenstates are given as,

$$u_v(\mathbf{k}) = \begin{pmatrix} e^{i\tau\phi_k}\sin\frac{\theta_k}{2} \\ -\cos\frac{\theta_k}{2} \end{pmatrix}, \qquad u_c(\mathbf{k}) = \begin{pmatrix} \cos\frac{\theta_k}{2} \\ e^{-i\tau\phi_k}\sin\frac{\theta_k}{2} \end{pmatrix}, \tag{2.5}$$

where $\theta_k = \cos^{-1}(\Delta/2\varepsilon(k))$. The phase $e^{i\tau\phi}$ in the eigenstates indicates that the conduction band has a winding of -1 (+1) at K (K'), while the valence band has a winding of +1 (-1) at K (K'). This phase winding is only present when k is finite around K and K' valley.

For the Bloch bands and wavefunctions in TMDs, we have the freedom to add a

phase before the wavefunction, which introduces a gauge-freedom in k-space. This is a fundamental property of the Bloch bands, that is, the geometry, usually discussed in the context of Berry phase and Berry curvature[15]. The Berry phase or geometric phase is defined as,

$$\phi_k = \int_c \mathcal{A}(\mathbf{k}) d\mathbf{k} \tag{2.6}$$

where $\mathcal{A}$ is the Berry connection or Berry vector potential given by,

$$\mathcal{A}(\mathbf{k}) = i\langle u(\mathbf{k})|\nabla|u(\mathbf{k})\rangle \tag{2.7}$$

c is a closed path for the integral. The Berry connection can be understood as the magnetic vector potential in the k-space, so we can further define a gauge invariant magnetic field tensor in k-space called Berry curvature by

$$\mathbf{\Omega}(\mathbf{k}) = \nabla_{\mathbf{k}} \times \mathcal{A}(\mathrm{k}) \tag{2.8}$$

In ML TMDs, Berry curvature $\mathbf{\Omega}(\mathbf{k}) = -\tau \frac{2a^2t^2(\Delta - \tau s_z \lambda)}{[(\Delta - \tau s_z \lambda)^2 + 4a^2t^2k^2]^{\frac{3}{2}}}$, where s_z is the spin and 2λ is the SOC splitting[14]. The Berry curvature has opposite sign in K ($\tau = 1$) and K' ($\tau = -1$) valleys and also opposite in conduction and valence bands, since $\mathbf{\Omega}(\mathbf{k}) = -\mathbf{\Omega}(-\mathbf{k})$ under the time reversal operation. If there is inversion symmetry, $\mathbf{\Omega}(\mathbf{k}) = \mathbf{\Omega}(-\mathbf{k}) = 0$. Thus Berry curvature is nonzero only when time-reversal symmetry or inversion symmetry is broken, which is the case for ML TMDs. Berry curvature is directly related to the valley physics, for example, the valley Hall effect, where the carriers in the opposite valleys shift to opposite edges as a result of the Berry curvature induced anomalous velocity $\mathbf{v} = -\dot{\mathbf{k}} \times \mathbf{\Omega}(\mathbf{k})$.

Another property relevant to the broken inversion symmetry in ML TMDs is valley-related orbital magnetic moment. It arises from the winding of the electron

wavefunction and is defined as,

$$\mathbf{m}_n(\mathbf{k}) = -i\frac{e\hbar}{2m^2}\sum_{i\neq n}\frac{\mathbf{P}_{n,i}(\mathbf{k})\times\mathbf{P}_{i,n}(\mathbf{k})}{E_n^0(\mathbf{k})-E_i^0(\mathbf{k})} = \tau\frac{2a^2t^2(\Delta-\tau s_z\lambda)}{(\Delta-\tau s_z\lambda)^2+4a^2t^2k^2}\frac{e}{2\hbar}\hat{\mathbf{z}}, \qquad (2.9)$$

where $\mathbf{P}$ is the interband transition matrix, i, n label different energy bands[16]. For conduction and valence bands with the same valley and spin indices, the valley-related orbital magnetic moment is the same.

2.1.4 Optical excitations in ML TMDs—exciton complexes

After we discuss the electronic ground states of ML TMDs, we will explore the optically addressable excited states. When we shed light with energy above the bandgap, the single particle picture suggests that the lowest energy excitation is from VBM to CBM at K or K' valley. In other words, an electron is excited from VBM to CBM, leaving a hole in the VBM. This is not the case for all ML TMDs because the SOC splits the spin up and down bands in a different way for WX_2 and MoX_2. As shown in Fig. 2.3a, CBM has different spin from the VBM for WX_2 while CBM and VBM have the same spin for MoX_2. In order to conserve the spin during the optical transition, the lowest energy excitations are depicted in Fig. 2.3a. Another spin-allowed transition is between CBM and the lower valence band for WX_2 or between the higher conduction band and lower valence band for MX_2, which are hundreds of meV higher than the lowest energy one.

Since the optical transitions occur at K and K' valleys, they need to follow the optical selection rules imposed by valley physics. The valley-dependent optical selection rules are that σ^+-polarized light couples to K valley while σ^--polarized light couples to K' valley (Fig. 2.3a). The underlying mechanism is the optical transition matrix element $\langle u_c(\mathbf{k})|\hat{p}|u_v(\mathbf{k})\rangle$, where $u_v(\mathbf{k})$ is the initial state at the valence band, $u_c(\mathbf{k})$ is the final state at the conduction band, $\hat{p}$ is the momentum operator ($\hat{p}\propto\hat{v}$). There-

fore $\sigma^{\pm}$-polarized transition is corresponding to $\hat{p}_{\pm} = \hat{p}_x \pm i\hat{p}_y$, and the probability of them is then proportional to,

$$P_{\pm} = |\langle u_c(\mathbf{k})|\hat{p}_{\pm}|u_v(\mathbf{k})\rangle|^2 = \frac{m^2a^2t^2}{\hbar^2}(1 \pm \tau\frac{(\Delta - \tau s_z\lambda)}{\sqrt{(\Delta - \tau s_z\lambda)^2 + 4a^2t^2k^2}})^2, \tag{2.10}$$

where m is the electron mass. As $\Delta - \tau s_z\lambda \gg 2atk$ inside the light cone ($k \sim 10^{-3}4\pi/3a$), we can see that K(K') valley optical transition is almost fully $\sigma^{\pm}$ polarized. In the calculation of the optical transition matrix, there is a phase factor $e^{i(m-(w\mp1+3n)\phi_k)}$, where m is the angular moment of the transition, w is the phase winding (the same as τ in ML TMDs), and n is any integer number with a coefficient of 3 dictated by the 3-fold symmetry. This phase factor needs to be 1 or else the angular average of the matrix element will be zero, which means $m = w \mp 1 + 3n$[17]. In ML TMDs, $w = 1$, so m = 0 (s-state), -1 (p-state), 2 (d-state) are bright.

The above single particle picture describes the process to generate an electron-hole pair with light (photon) but ignores the Coulomb interactions between electron and hole. In the 2D limit, since there is less screening from the surrounding environment, Coulomb attractions between photoexcited electrons and holes are enhanced, resulting in strongly bound electron-hole pairs, called excitons (Fig. 2.3 b)[18, 19]. The excitons are basically "hydrogen atoms" in a crystal with a binding energy E_b of 150-650 meV and Bohr radius a_B of 1-2 nm, so they also have Rydberg states, such as 1s, 2s etc. Nevertheless, due to the spatially dependent dielectric screening (for example, 2s exciton is screened less than 1s exciton, Fig. 2.3c), the screened Coulomb electron-hole interaction is described by the Keldysh potential,

$$V_{eh}(r) = -\frac{\pi e^2}{2r_0}\left[H_0(\frac{r}{r_0}) - Y_0(\frac{r}{r0})\right]. \tag{2.11}$$

where H_0 and Y_0 are Struve and Bessel functions and r_0 is the screening length [18, 19]. The difference between V_{eh} and unscreened Coulomb potential is increased

with reduced electron-hole separation (r), producing a non-Hydrogenic spectrum. Furthermore, the ratio between Bohr radius (1-2 nm) and the lattice constant (0.3 nm) is in the range of 3-6, implying that the TMD exciton states are practically Wannier-Mott exciton states which are the superposition of many k electron-hole states ($\delta k \sim 1/a_B$). In other words, excitons contain not only the K or K' point information but also the K+k or K'+k point information. Thereafter, we need to consider excitons as the optical excitations in ML TMDs instead of transition between CBM and VBM.

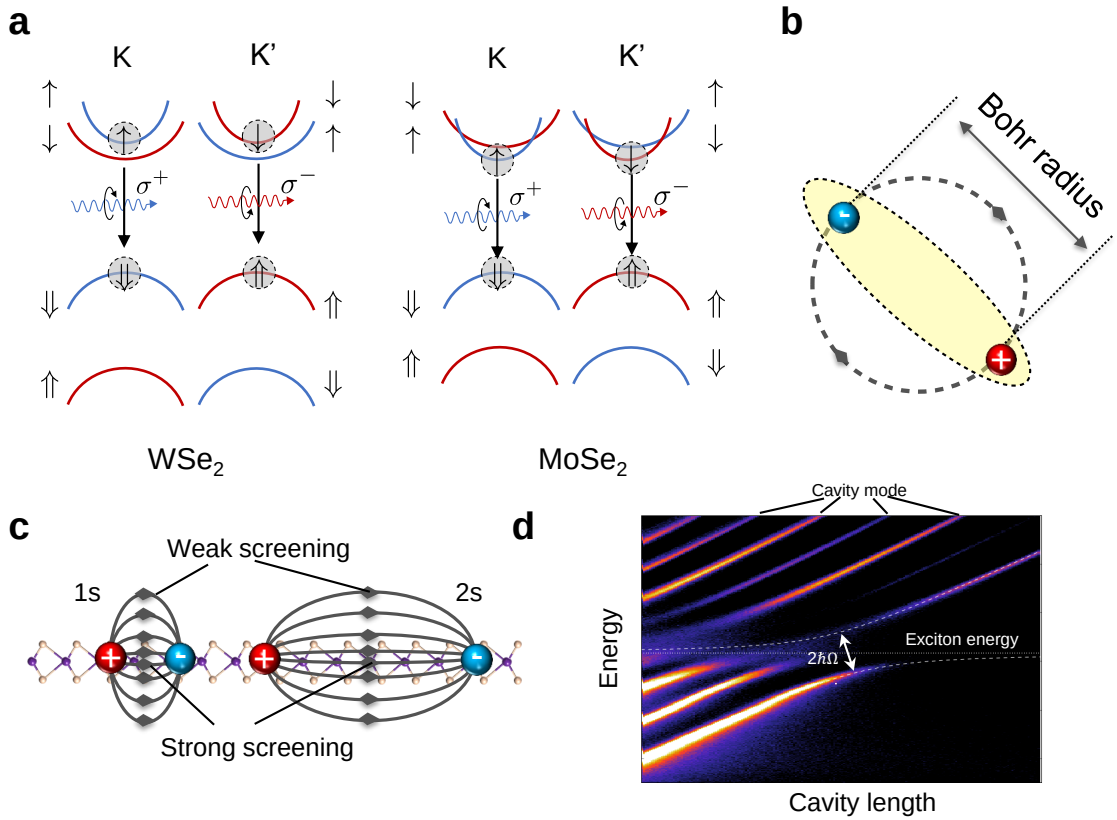

Figure 2.3: Excitons in ML TMDs. **a.** Single particle band for WSe_2 (left) and $MoSe_2$ (right) **b.** An tightly bound exciton. **c.** Strong screening in the TMD layer and weak screening in the environment, adapted from Ref[18, 19]. **d.** Strong light-matter coupling in ML TMDs, adapted from Ref.[20]

If we use optical measurements to study ML TMDs, a natural question arises

how strong the light-matter coupling is in ML TMDs. This can be measured by placing the ML TMD into a cavity. The cavity mode (cavity electric field strength g) can couple to the exciton resonance in ML TMD (dipole moment d) through light-matter coupling. The strength of the coupling is characterized by the Rabi splitting $2\hbar\Omega = 2dg = 2d(\frac{\hbar\omega}{\epsilon_0\epsilon_r V})^{\frac{1}{2}}$, where d is the oscillating dipole and V is the volume of the confinement. The coupling strength is 30–40 meV, which is larger than the decay rate (a few meV) and in the strong coupling regime [21, 22, 20, 23].

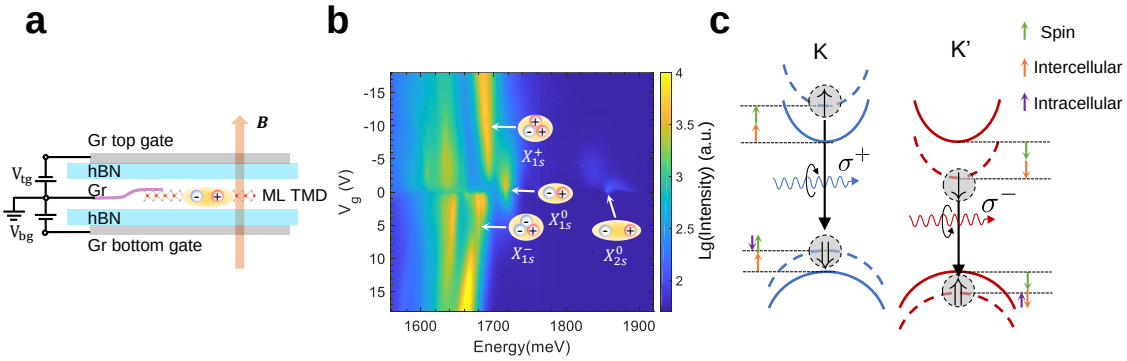

Figure 2.4: Gate and magnetic field control of TMD excitons. **a.** The schematic of the dual-gated sample. **b.** Gate dependent PL of ML WSe_2. The excitation is 20 μW HeNe laser. **c.** Magnetic field induced conduction and valence band energy shift.

In addition to the strong light-matter coupling, another advantage of ML TMDs is that we can easily apply gate voltage or magnetic field to change the exciton properties. The gate control is achieved by fabrication of such a device with two graphite gates as shown in Fig. 2.4a. The details of fabrication will be discussed in Chapter 3. Considering a parallel capacitor model, the negative gate voltage introduces holes into the sample while the positive voltage dopes electrons into the sample. The neutral excitons X^0 then bind an additional electron or hole to form charge excitons, called trions. As plotted in the Fig. 2.4b, we observed both positive and negative trions with a binding energy of 20-30 meV. It is worthy noting that there are both 1s and 2s excitons as we discuss above. Besides the gate control, we can have magnetic field

manipulation due to the spin, valley-related orbital magnetic moment (intercellular contribution) and atomic orbital magnetic moment (intracellular contribution) of the conduction and valence bands (Fig. 2.4c). We have introduced the first and second components which are the same for conduction and valence bands and cancel out for exciton optics. As for the atomic orbital magnetic moment, the conduction band (d_{z^2} orbital) $m_c = 0$, whereas the valence band ($d_{x^2-y^2} + i\tau d_{2xy}$ orbital) $m_v = 2\tau$ opposite in two valleys. As a result, the exciton energy in two valleys is split by $\sim 4\mu_B$ under the out-of-plane magnetic field, known as valley Zeeman effect[24, 25, 26, 27].

In the end, we will introduce localized ML excitons, which are created by excitons confined by defect or strain potential. Localized ML excitons are characterized by sharp PL emission (∼40-90 μeV) as in Fig. 2.5 as a result of their long lifetime (ns compared to ps without confinement). The confinement in real space corresponds to larger k range in the momentum space, which has components outside the light cone and effectively increases the lifetime of excitons. More importantly, localized excitons are single photon emitters with anharmonic spectra, because the confinement makes the exciton energy discrete and an extra exciton will modify the energy[28, 29].

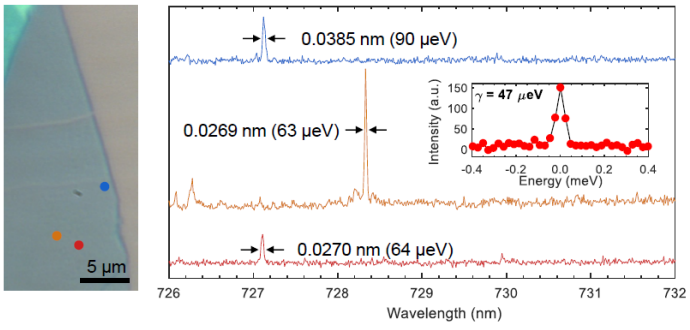

Figure 2.5: PL spectra of localized ML TMD excitons at different sample spots. The localized excitons have different emission energies and linewidths depending on the local potential landscape.

2.2 VdW Heterostructures

As an inverse process of exfoliation, stacking ML TMDs to be highly customized vdW heterostructures has stimulated great interest in the physics society. The research on vdW heterostructure distinct from ML TMDs can be probably classified into three parts: (1) twist angle dependent superlattice potential (moiré potential) induced strongly correlated many-body effects[30, 31, 32, 33, 34, 35, 36, 37, 38, 39]; (2) the band alignment controlled optoelectronics, such as electrically controllable interlayer exciton[40, 41, 42, 43, 44], charge dynamics[45, 46]; (3) Proximity effect especially for coupled magnetic or ferroelectric TMD materials[47, 48, 49]. We will investigate the first two parts in this dissertation.

2.2.1 Artificial supercell–moiré superlattice

When we stack ML TMDs layer by layer, we have multiple tunable parameters for the stacking process, in contrast to natural bilayer or multilayer TMDs, which are 2H stacking (180°) with aligned M and X atoms (Fig. 2.1c). Those tunable parameters include twist angle, interfacial sliding, and various TMD material choices with diverse lattice and electronic properties. Based on the lattice constant for group-VI TMDs (Table 2.1), we can categorize the vdW heterostructures into two types: one is heterobilayers with negligible lattice mismatch such as $WSe_2/MoSe_2$, WS_2/MoS_2 and all homobilayers comprised of two same ML TMDs; the other one is heterobilayers with large lattice mismatch including WSe_2/WS_2, WSe_2/MoS_2, $MoSe_2/WS_2$ and $MoSe_2/MoS_2$. As shown in Fig. 2.6a, the first case can twist a small angle between the two layers to form a superlattice structure called moiré lattice, resulting from the moiré interference between the constituent layers. The period of the moiré lattice is then called moiré length with a scale of $\sim$10 nm, much larger than the intrinsic lattice constants. Due to the broken inversion symmetry, there are two kinds of stacking de-

pending on the twist angle: AA stacking (or R stacking, close to 0°) as in Fig. 2.6a left panel and AB stacking (or H stacking, close to 60°, same to 180° by a 120° rotation) as in Fig. 2.6a right panel. The difference between them is the atomic configurations (registries) at the high symmetry points (Fig. 2.6e, f). As for the second case (Fig. 2.6c), it can form the moiré lattice even without a twist and have similar highly symmetric registries. Though the superlattice structures and electronic properties are comparable for the two cases, the twist angle dependence of moiré length is quite different. For a small twist angle θ, the moiré length $a_M \approx \frac{a_0}{\sqrt{\theta^2+\delta^2}}$, where a_0 is the intrinsic lattice constant and δ is the lattice mismatch $\frac{\Delta a_0}{a_0}$. Using this formula, the first case with negligible lattice mismatch has a moiré length much more sensitive to the twist angle and almost divergent at marginally aligned structures (Fig. 2.6b, d), which is not realistic as discussed below.

The preceding discussion is based on the fact that the ML TMD lattices are rigid and hard to change. However, in reality, the superlattice structures will relax and reconstruct to maximize the stable registries and minimize the total energy as confirmed in the theoretical calculations[50, 51], especially for the negligible lattice mismatch case. This relaxation and reconstruction induced corrugated moiré lattice is also corroborated experimentally by imaging the moiré pattern by piezoresponse force microscopy (PFM)[52] and conductive atomic force microscopy (C-AFM)/transmission electron microscopy(TEM) [53]. Besides, for almost zero twist angle homobilayers, interfacial ferroelectricity was observed because the reconstruction creates MX and XM domain structures [54, 55]. This relaxation changes the moiré pattern but not the moiré length, so the length scale is still much larger compared to the lattice constant. More importantly, this also proves the coupling between the two layers. Another method to prove the coupling is the real-space imaging of the bandgap modulation (i.e., moiré potential) using scanning tunneling microscopy and spectroscopy (STM/S). STM/S measurements show periodic moiré potential with stack-

ing order dependent potential minima (traps) at different registries. For AA stacking MoS_2/WSe_2, the moiré potential varies 200 meV with potential minima at the MM and MX [56]. For AB stacking $WSe_2/MoSe_2$, a valence band potential trap of 300 meV and conduction band potential trap of 150 meV are both at MX site[57]. A simple explanation for moiré potential formation is that charge transfer between the two constituent layers varies for different registries (for example, M tends to lose electrons to X) and creates potential difference among them. These two evidences unambiguously support the layer coupling and thus the existence of moiré effect as discussed in the next section.

Table 2.1: Lattice constants and band alignment of TMDs [5]

TMD	Lattice constants (Å)	VBM (eV)	CBM (eV)
MoS_2	3.16	-6.42	-3.71
$MoSe_2$	3.29	-5.75	-3.38
WSe_2	3.28	-5.49	-2.92
WS_2	3.15	-6.19	-3.28

2.2.2 Moiré bands and strongly correlated electrons

When a moiré superlattice is formed, the low energy physics is set by the moiré period scale a_M, as opposed to the high energy physics set by intrinsic lattice constant a_0. In real space, each moiré potential minimum can be considered as an available site for electrons. As a consequence, the total available sites (moiré density) are on the order of a_M^{-2} (10^{12} cm^{-2}). Therefore, we can dope several electrons per site with relatively low electron density before reaching the breakdown voltage of the dielectric. In other words, if we consider the different energy states at each site as different orbitals, corresponding to different moiré bands in k-space, we can dope to separate moiré bands to study their electronic properties.

Furthermore, the relatively large moiré period a_M reduces the hopping integral (or kinetic energy) between nearest-neighbors, which is the bandwidth of the moiré

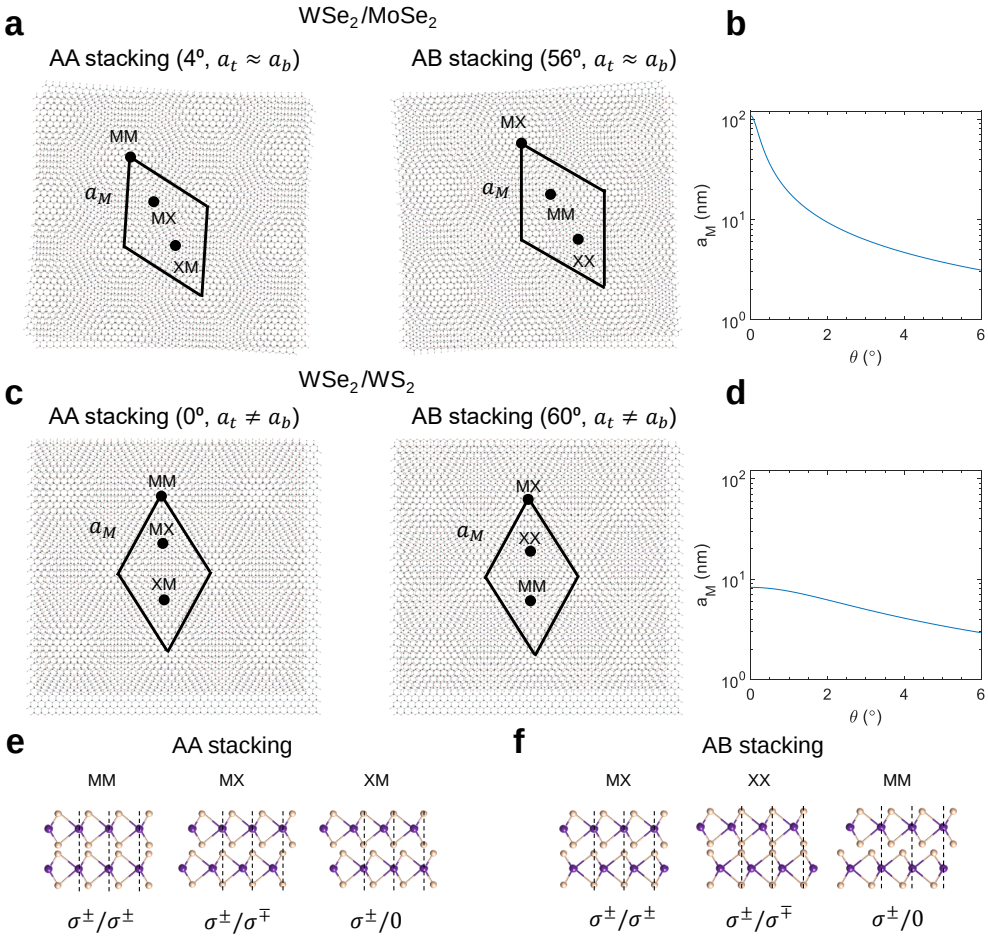

Figure 2.6: Moiré superlattice and optical selection rules. **a.** AA and AB stacking moiré superlattice with zero lattice mismatch and a small twist angle ($WSe_2/MoSe_2$). **c.** Calculated moiré length a_M with respect to the twist angle for $WSe_2/MoSe_2$ **c.** AA and AB stacking moiré superlattice with a small lattice mismatch and zero twist angle (WSe_2/WS_2). **d.** Calculated moiré length a_M with respect to the twist angle for WSe_2/WS_2. **e-f.** High symmetry registries and corresponding optical selection rules for AA (**e**) and AB stacking (**f**). M is the transition metal atom and X is the chalcogenide atom. σ^+/σ^+ ($\sigma^+/0$) means that σ^+ excitation generates σ^+ (no) emission.

bands ($W \propto a_M^{-2}$). The Coulomb repulsion between two electrons in the same site (on-site repulsion) $U \propto a_M^{-1}$. $U \gg W$, that is, interaction energy is much larger than the kinetic energy, can be satisfied at large a_M, indicating electrons in the strongly correlated regime.

To formulate the prior discussion, we can start with the continuum model for AA stacking $WSe_2/MoSe_2$ following Ref.[58]. The continuum model is to ignore the details of commensurability between the moiré pattern and atomic lattice. To a good approximation, we can consider the electrons (or holes) with effective mass (M) moving in a smooth periodic moiré potential $\Delta(\mathbf{r})$. Bloch's theorem for the electronic bands can still be applied to the folded mini-Brillouin zone (mBZ, its reciprocal lattice vector $|\mathbf{G}| = \frac{4\pi}{\sqrt{3}a_M}$). We obtain the moiré valence band Hamiltonian:

$$\begin{aligned} \mathcal{H} &= -\frac{\hbar^2\mathbf{k}^2}{2m^*} + \Delta(\mathbf{r}), \\ \Delta(\mathbf{r}) &= \sum_{\mathbf{G}} V(\mathbf{G}) e^{i\mathbf{G}\cdot\mathbf{r}}, \end{aligned} \tag{2.12}$$

where $-\frac{\hbar^2\mathbf{k}^2}{2m^*}$ is the hole kinetic energy and $\mathbf{G}$ includes six moiré reciprocal lattice vector in the first Brillouin zone. The C_3 rotation symmetry requires $V(\mathbf{G}) = V^*(-\mathbf{G}) = Ve^{i\phi}, V(\mathbf{G}) = V(\hat{C}_3\mathbf{G}) = Ve^{i\phi}$. The moiré potential in AA stacked $WSe_2/MoSe_2$ can be plotted as in Fig. 2.7a using the parameter in Ref.[58]. The moiré Bloch bands are calculated by diagonalizing the Hamiltonian on a plane-wave basis. The total Bloch function Fourier series and the diagonalized terms are

$$\begin{aligned} \psi_{\mathbf{k}}(\mathbf{r}) &= \sum_{\mathbf{G}} C_{\mathbf{k}+\mathbf{G}} \frac{e^{i(\mathbf{k}+\mathbf{G})\cdot\mathbf{r}}}{\sqrt{\Omega}} = \sum_{\mathbf{G}} C_{\mathbf{k}+\mathbf{G}} |\mathbf{k}+\mathbf{G}\rangle, \\ \langle \mathbf{k}+\mathbf{G}|\mathcal{H}|\mathbf{k}+\mathbf{G}'\rangle &= -\frac{\hbar^2(\mathbf{k}+\mathbf{G})^2}{2m^*}\delta_{\mathbf{G},\mathbf{G}'} + V(\mathbf{G}-\mathbf{G}'), \end{aligned} \tag{2.13}$$

The Schrödinger equation becomes:

$$[-\frac{\hbar^2(\mathbf{k}+\mathbf{G})^2}{2m^*} - E_{\mathbf{k}+\mathbf{G}}]C_{\mathbf{k}+\mathbf{G}} + \sum_{\mathbf{G}'\neq\mathbf{G}} V(\mathbf{G}-\mathbf{G}')C_{\mathbf{k}+\mathbf{G}'} = 0. \tag{2.14}$$

The calculated valence bands for 2.5° twisted $WSe_2/MoSe_2$ are shown in Fig. 2.7b with the highest moiré valence band separated from other bands. The bandwidth of the isolated band is 20 meV, which is much smaller than the depth of moiré potential and considered as a flat band. The calculated density of states (DOS) is enhanced and maximized at the moiré band saddle points (Fig. 2.7c). For the real space wavefunction, we can construct the Wannier function from the isolated band's Bloch states and find that it is localized at moiré potential minima with spatial extent $a_W \sim 2$ nm. Therefore, we can use a tight-binding model to describe this flat band:

$$\mathcal{H} = \mathcal{H}_0 + \mathcal{H}_1,$$

$$\mathcal{H}_0 = \sum_{\tau}\sum_{\mathbf{R},\mathbf{R}'} t(\mathbf{R}-\mathbf{R}')c^\dagger_{\mathbf{R},\tau}c_{\mathbf{R}',\tau} \tag{2.15}$$

$$\mathcal{H}_1 = \frac{1}{2}\sum_{\tau,\tau'}\sum_{\mathbf{R},\mathbf{R}'} U(\mathbf{R}-\mathbf{R}')c^\dagger_{\mathbf{R},\tau}c^\dagger_{\mathbf{R}',\tau'}c_{\mathbf{R}',\tau'}c_{\mathbf{R},\tau}, \tag{2.16}$$

This is called Hubbard model with hopping t and on-site repulsion U illustrated in Fig. 2.7d. The hopping t is fitted to be the nearest-neighbor (NN) hopping t_1 = 2.57 meV, next nearest-neighbor (NNN) hopping t_2 = -0.52 meV and the third nearest-neighbor hopping t_2 = -0.27 meV (see Appendix A). Regarding the repulsion, on-site $U \approx \frac{e^2}{4\pi\epsilon_0\epsilon_r a_W} \approx$ 100-200 meV and the NN repulsion $V \approx \frac{e^2}{4\pi\epsilon_0\epsilon_r a_M} \approx$ 50-100 meV. Therefore, TMD moiré physics is in a strong interaction regime $U > V > W$. It should be noted that we have not included interactions in the single particle band calculation. The strong interactions between particles at the same or different sites can be comparable to the single-particle bandgap so the single-particle description is inaccurate.

When the highest valence band is half-filled ($\nu = 1$), that is, electrons occupy all available sites, the on-site U opens a Mott gap and the vdW heterobilayer becomes a correlated insulator. This was observed as an incompressible state at $\nu = 1$ both by transport and optics measurement[34]. If the filling is at some commensurate fractional filling such as $\nu = 1/2$ or $2/3$, the strong interaction U and V will stabilize charge-ordered states, called general Wigner crystals (Fig. 2.7e) [35, 59, 60]. Direct imaging of the flat bands [61, 62] and charge-ordered states[38] has been obtained by STM/S measurements. Besides, if slightly doped away from $\nu = 1$, WSe_2/WSe_2 homobilayer shows zero-resistance states, which could be unconventional superconductivity [63]. Despite the fact that the moiré bands are non-topological in the Hub-

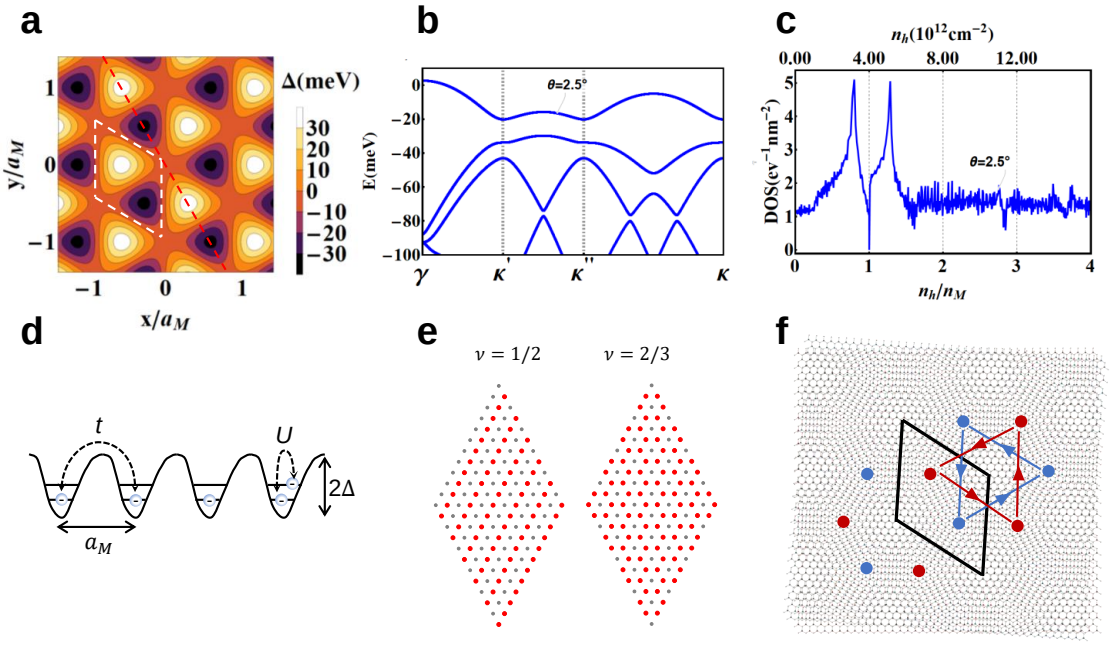

Figure 2.7: Moiré superlattice and optical selection rules. **a.** Moiré potential landscape for twisted $WSe_2/MoSe_2$. **b-c.** Calculated hole moiré bands (**b**) and density of states (DOS) (**c**) for $WSe_2/MoSe_2$ with a twist angle of 2.5°. $\kappa, \kappa', \kappa''$ are the moiré Brillouin zone corners. κ' is adjacent to κ'' and opposite to κ. **d.** Schematic of moiré potential filled by electrons with nearest-neighbor hopping t and on-site repulsion U. **e.** General Wigner crystal at quarter filling ($\nu = 1/2$) and one-third filling ($\nu = 2/3$). Red dots are occupied sites and gray dots are unoccupied sites. **f.** Illustration of Kane-Mele-Hubbard model in a honeycomb lattice.

bard model, they can be topologically nontrivial captured by Kane-Mele model[64]. Considering an AA stacking homobilayer, the large SOC separates the spin-up and spin-down bands, so we can focus on the spin-up valence-band states in K valley, producing the two-band $k \cdot p$ Hamiltonian as,

$$\mathcal{H}(\mathbf{k}) = \begin{pmatrix} -\frac{\hbar^2(\mathbf{k}-\kappa_+)^2}{2m^*} + \Delta_b(\mathbf{r}) & \Delta_T(\mathbf{r}) \\ \Delta_T^\dagger(\mathbf{r})) & -\frac{\hbar^2(\mathbf{k}-\kappa_-)^2}{2m^*} + \Delta_t(\mathbf{r}) \end{pmatrix}, \tag{2.17}$$

where $\kappa_\pm$ are the moiré Brillouin zone corners. $\Delta_{b,t}(\mathbf{r}) = 2V \sum_{j=1,3,5} \cos(\mathbf{G}_j \cdot \mathbf{r} \pm \phi)$ is the bottom/top layer dependent energies, respectively. $\Delta_T = w(1 + e^{-i\mathbf{G}_2\cdot\mathbf{r}} + e^{-i\mathbf{G}_3\cdot\mathbf{r}})$ is the interlayer tunneling, which is the key difference contrary to previous Hubbard model. The wavefunctions in the bottom and top layers are concentrated near MX and XM sites separately. Accordingly, the tight-binding model will have two orbitals, written as,

$$\mathcal{H} = \sum_{l,s} \sum_{\mathbf{R},\mathbf{R}'} t_0 c^\dagger_{\mathbf{R}ls} c_{\mathbf{R}'(-l)s} + \sum_{l,s} \sum_{\mathbf{R}} \sum_{\mathbf{a_M}} t_1 e^{is\kappa_l \cdot \mathbf{a_M}} c^\dagger_{\mathbf{R}+\mathbf{a_M}ls} c_{\mathbf{R}ls},$$

where $l = \pm$ is the orbital localized at the bottom (MX)/top layer (XM),$s = \pm$ is the spin index at K/K' valley. This Hamiltonian captures both the NN interlayer hopping (first part) and NNN intralayer hopping (second part) (Fig. 2.7f), equivalent to Kane-Mele model. If we fully fill the first band, we can get topological (Chern) insulator or quantum spin Hall insulator. When we fill up to certain fractional filling, the strong interaction could lead to spontaneous time-reversal symmetry breaking, giving rise to quantum anomalous Hall or fractional quantum anomalous Hall states. In fact, the quantum anomalous Hall states[37] and signature of fractional quantum anomalous Hall states[65] were discovered in TMD vdW materials recently.

2.2.3 Interlayer excitons and moiré exciton complexes

For a vdW heterobilayer, the band alignment engineering is a knob to tune the carrier type in the constituent layers[66, 67]. Table 2.1 shows the band edges for WX_2 and MoX_2, generating two sets of band alignment, viz, type-II band alignment ($WSe_2/MoSe_2$, Fig. 2.8a) and type-I band alignment ($WS_2/MoSe_2$, Fig. 2.8b). For type-II band alignment, electrons and holes are located on different layers as the CBM and VBM are at different layers, for example, holes in WSe_2 layer and electrons in $MoSe_2$ layer for the $WSe_2/MoSe_2$ heterobilayer. In contrast, type-I band alignment forces the electrons and holes on the same layer, for example, only $MoSe_2$ layer for the $WS_2/MoSe_2$ heterobilayer. Consequently, optical excitations are interlayer excitons (IXs) in $WSe_2/MoSe_2$ and intralayer excitons (ML excitons) in $WS_2/MoSe_2$. What's more, the IXs have lower energy compared to the intralayer resonance according to the band edges (Fig. 2.8a, d). The IX real space picture is shown in Fig. 2.8 c with the electron and hole spatially separated into two layers, which form a permanent out-of-plane dipole pointing from $MoSe_2$ to WSe_2. The dipole energy can be tuned by external electric field, which will cause red- (or blue-) shifts when the E field is aligned or anti-aligned to the dipole, as shown in Fig. 2.8e. However, as a result of the layer separation, the electron and hole overlap of IXs is quite small compared to intralayer excitons, and thus the oscillation strength (optical absorption and emission rate) is two orders of magnitude smaller than the intralayer ones[68] and lifetime is two orders of magnitude longer ($\sim$ ns)[40]. Therefore, we usually generate IXs by exciting at the intralayer resonances and ultrafast charge transfer (< 50 fs) brings electrons or holes to the lower energy layer to form IXs[45, 69]. As we can observe in Fig. 2.8f, both $MoSe_2$ and WSe_2 intralayer resonances generate high density of IXs. During the charge transfer process, the valley index is usually conserved, and hence the IXs are valley polarized with a long valley lifetime[41, 70]. One of current application of the IXs is the excitonic circuit, which relies on the fact that spatially

varied E field coupled to the IX dipole moment can create a potential gradient to transport the IXs[42, 44, 71, 72].

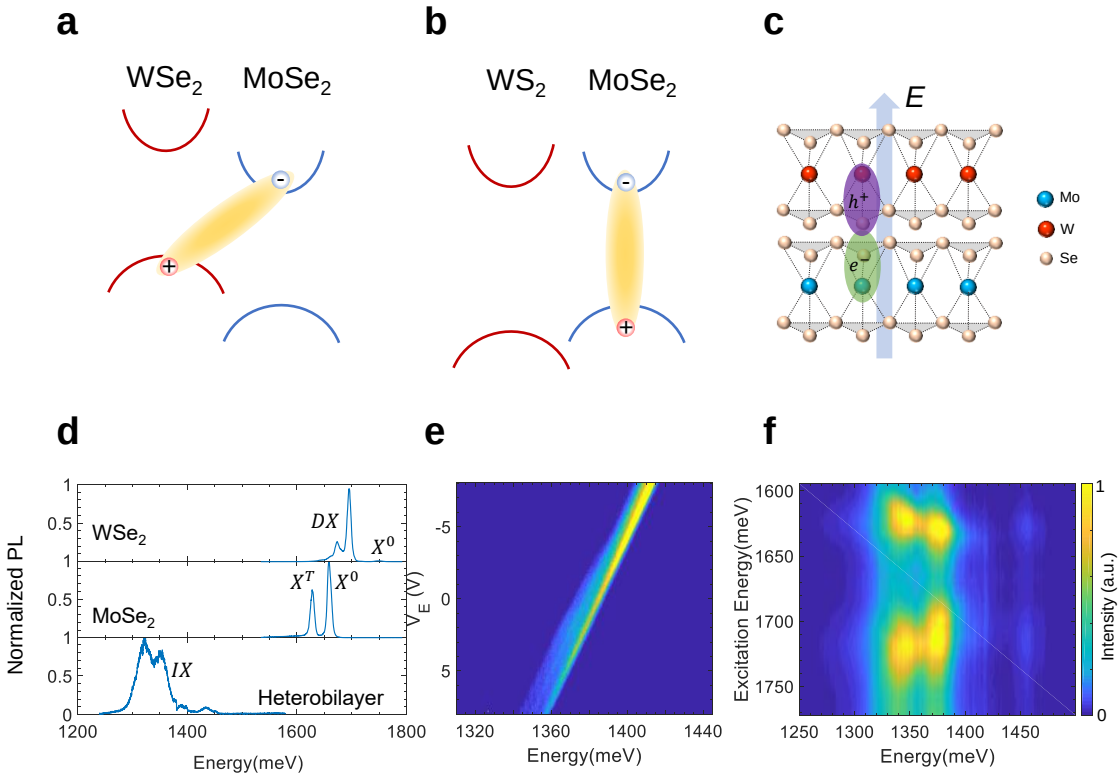

Figure 2.8: Interlayer excitons. **a.** Type-II alignment for $WSe_2/MoSe_2$. **b.** Type-I alignment for $WS_2/MoSe_2$. **c.** Real space exciton in $WSe_2/MoSe_2$ heterobilayer. The electron and hole in the exciton are separated in $MoSe_2$ and WSe_2, respectively, forming a permanent out-of-plane dipole. The dipole energy is tunable by out-of-plane electric field E. **d.** Normalized photoluminescence (PL) spectra. Top: Emission from defect band (DX) and exciton X^0 (∼1750 meV) dominates in WSe_2. Middle: Monolayer $MoSe_2$ shows two prominent peaks at 1658 meV and 1628 meV, corresponding to neutral exciton X^0 and trion X^T, respectively. Bottom: Emission from interlayer excitons appears at lower energy (1250 - 1450 meV). **e.** The electric field dependence of the IX PL emission energy. **f.** Photoluminescence excitation (PLE) spectroscopy of IXs show $MoSe_2$ intralayer resonance (1640 meV) and WSe_2 intralayer resonance (1730 meV).

Next, we need to include the moiré effect on the excitonic states for vdW heterostructures with small twist angle or lattice mismatch. As the conduction and valence bands are both subjected to the moiré potential, the optical excitations from

band edge transitions will be also modulated, yielding moiré excitonic bands. Depending on the modulated conduction and valence bands are from the same layer or individual layers, the moiré intralayer and interlayer excitons are formed. The exciton Hamiltonian for both cases are simplified as,

$$\mathcal{H} = \mathcal{H}_0 + \Delta(\mathbf{r}) \tag{2.18}$$

where $\mathcal{H}_0$ is the intralayer or interlayer exciton low-energy effective Hamiltonian without moiré potential, $\Delta(\mathbf{r}) = \sum_{j=1}^{6} V(\mathbf{G}_j) e^{i\mathbf{G}_j \cdot \mathbf{r}}$ is the effective moiré potential. The low energy effective Hamiltonian includes exciton transition energy constant $\hbar\Omega_0$ and the kinetic energy $\hbar^2\mathbf{Q}^2/2M$, where $\mathbf{Q}$ is the exciton center-of-mass momentum and $M = m_e + m_h$ is the total exciton mass. The explicit form is:

$$\begin{aligned} Intra : \mathcal{H}_0 &= \left(\hbar\Omega_0 + \frac{\hbar^2\mathbf{Q}^2}{2M}\right)\tau_0 + J|\mathbf{Q}|\tau_0 + J|\mathbf{Q}|[\cos(2\phi_{\mathbf{Q}})\tau_x + \sin(2\phi_{\mathbf{Q}})\tau_y], \\ Inter : \mathcal{H}_0 &= \left(\hbar\Omega_0 + \frac{\hbar^2\mathbf{Q}^2}{2M}\right), \end{aligned} \tag{2.19}$$

The additional term for intralayer exciton is the electron-hole $(e-h)$ Coulomb interaction exchange part J, which is quenched for interlayer excitons because of small $e-h$ overlap[73]. τ_0, τ_x, τ_y are the Pauli matrices for valley pseudospin and $\phi_{\mathbf{Q}}$ is the angle between $\mathbf{Q}$ and $\hat{\mathbf{x}}$.

We first focus on the intralayer exciton Hamiltonian which has a distinct form from the electronic one (Equation (2.12)). In order to diagonalize the total Hamiltonian, we adopt plane wave representation as in the Equation (2.13). After plugging the DFT fitted potential $V_1 = V(\mathbf{G_1}) = Ve^{i\phi}$, $(V, \phi) = (1.4$ meV, $98.6^\circ)$ and $M = 1.3\ m_0$ for AA stacked WS_2/MoS_2 into the equation, we can obtain the moiré intralayer excitonic band in Fig. 2.9a[74]. Then we can calculate the optical absorption (conductivity)

using the following equation:

$$Re\sigma(\omega) \approx \frac{1}{2} Re\sigma^{(0)}(\Omega_0) \sum_n |\sum_{\alpha=\pm} \langle \chi_n | K_\alpha^{(0)} \rangle|^2 \frac{\eta^2}{\hbar^2(\omega-\omega_n)^2+\eta^2},$$

where the $|K_\alpha^{(0)}\rangle$ and $Re\sigma^{(0)}(\Omega_0)$ are the valley K_α exciton eigenstates and optical conductivity with zero twist angle. ω_n and χ_n are the eigenvalues and eigenstates at γ point and η is the linewidth. The calculated optical conductivity in Fig. 2.9b also shows multiple resonances, labeled as red dots in Fig. 2.9a. These new resonances appearing at higher energy can be understood by the exciton Umklapp process that brings the momentum finite excitons into the light cone at γ point, which has been observed in WSe_2/WS_2 heterobilayer as shown in Fig. 2.9d[32, 30].

Next, we calculate the interlayer excitonic bands following the same procedure. By substituting the potential $(V, \phi) = (12.4 \text{ meV}, 81.5°)$ and total exciton mass $M = 0.76\ m_0$ into the IX Hamiltonian, the calculated bands are shown in Fig. 2.9c[75, 76] with the similar multi-resonance feature at γ point. Besides, the optical selection rules are also modulated to be registry-dependent as the optical transition is mediated by the interlayer coupling that depends on the local registries[77, 78, 75]. There are three high-symmetry points in AA or AB stacking samples where the IXs can couple to light through distinct optical selection rules (Fig. 2.6e, f)[43, 50, 77, 78]. Furthermore, the magnetic field dependence of the IX energies (i.e., Zeeman effect, quantified by Landé g factor) also depends on stacking order and registries. For example, MX (MM) in AA stacking has a g factor of 6 (-6) while MX in AB stacking has a g factor of -16 [31, 43, 50]. The much larger g factor of AB stacking is because the spin and valley-related orbital magnetic moment are not canceled out for CBM and VBM in opposite valleys.

Previous discussions on moiré excitons suppose that electron and hole parts are in the same potential trap, so we can apply continuum model to the moiré excitons.

However, the large-scale first principle calculation unveils both charge-transfer intralayer (Fig. 2.9e)[79] and interlayer excitons (Fig. 2.9f)[80], where electron and hole wavefunctions are localized at different registries. The charge-transfer interlayer excitons can further bind neighboring charges to form an intercell moiré excitons[80].

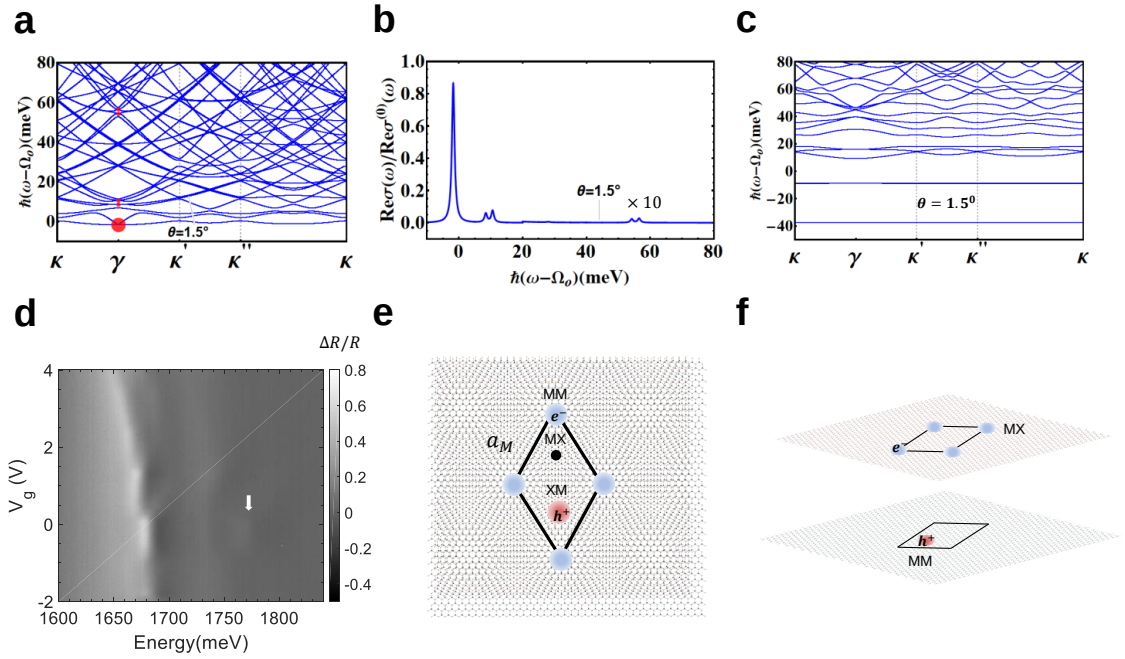

Figure 2.9: Moiré excitons. **a, b.** Calculated moiré intralayer exciton bands (**a**) and optical absorption (**b**) for 1.5° twisted WS_2/Mo_2. The red dots are bright excitons. The Umklapp process brings momentum dark intralayer excitons to be bright. **c.** Calculated moiré interlayer exciton bands for 1.5° twisted WS_2/Mo_2. The Umklapp process brings momentum dark interlayer excitons to be in the light cones. **d.** The doping dependent reflectance contrast spectra show multi intralayer exciton resonances in AA stacked WSe_2/WS_2. **e.** Schematic of the electron and hole wavefunction for the highest-energy intralayer exciton resonance (∼1770 meV, white arrow peak in **d**), signifying a charge-transfer intralayer exciton. **f.** Schematic of the electron and hole wavefunction for interlayer excitons in AB stacked WSe_2/WS_2, suggesting a charge-transfer interlayer exciton.

2.2.4 Excitonic insulator

We note that optically excited excitons are non-equilibrium states. Equilibrium excitons are strongly bound electrons and holes at ground states. Such ground state

excitons were proposed to form in two regimes: small band overlap semimetals with negative charge gap (Bardeen–Cooper–Schrieffer regime) and small bandgap semiconductors with positive charge gap (Bose-Einstein condensate regime)[81]. As charges are bound to be excitons, the whole system is in a non-conducting state, called an excitonic insulator. In the first regime, at a certain Fermi level, one band is filled with electrons and the other band is filled with the same amount of holes so that all electrons and holes are bound to be neutral excitons and the system is insulating. In the second regime, the bandgap is smaller than the binding energy of excitons so that the fully filled valence band is unstable against the formation of excitons, leading to the excitonic insulator phase.

The excitonic insulator phase can be created in vdW heterostructures through electrostatic injection, either by both electron and hole injection (doping) into two separate layers[82, 83] or by particle-hole transformation [84, 85, 86] (Fig. 2.10). Both methods use a thin hBN to suppress the single particle tunneling. The first method attains a charge gap smaller than the exciton binding energy by applying an electric field E and a voltage bias V_b (Fig. 2.10a, b). E changes the band alignment and V_b changes the chemical potential. The charge gap of interlayer excitons is then reduced to be smaller than the binding energy, inducing an excitonic insulator state. The second method is realized in a Coulomb-coupled moiré-monolayer system at a total filling factor of $\nu_{total} = 1$ (Fig. 2.10c). Applying an out-of-plane E field allows the hole filling to be 1-δ in the moiré bilayer and δ in the monolayer. Consider the hole filling $\nu = 1$ in moiré bilayer as the new vacuum and particle-hole transform the empty sites in the moiré bilayer to be electrons, which bind the holes in the monolayer to be excitons. The exciton binding energy is the energy to dissociate an exciton by separating the hole and transformed electron, equivalent to placing a hole at the empty site and creating a doublon. In the limit of interlayer spacing much smaller than moiré length ($d \ll a_M$), the binding energy of such excitons can

be estimated as the on-site Coulomb repulsion (∼50 meV)[84]. The total filling of $\nu_{total} = 1$ is charge incompressible with electric field tunable exciton density, which is the thermodynamic evidence of excitonic insulators. Excitonic insulators are long-lived ground state excitons, promising for the investigation of Bose-Hubbard model and BCS-BEC crossover[87].

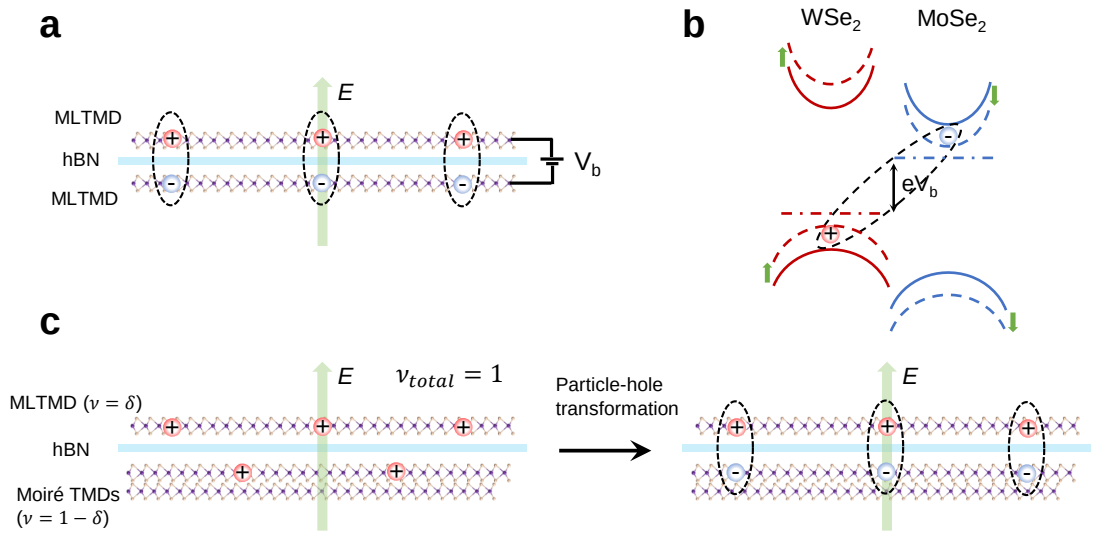

Figure 2.10: Excitonic insulators in vdW heterostructures. **a.** An excitonic insulator formed by electrons and holes injection into two layers separated by a thin hBN with both an electric field E and bias V_b. The hBN is used to suppress the electron and hole tunneling and thus their recombination. **b.** E (green arrow) changes the band alignment (dashed lines) and V_b changes the chemical potential (dash-dotted lines). The overall effect is the reduced charge gap of interlayer excitons. When the charge gap is smaller than the binding energy, an excitonic insulator is formed. **c.** An excitonic insulator formed by particle-hole transformation. The total hole filling is $\nu_{total} = 1$, with the hole filling 1-δ in the moiré TMD heterobilayer and δ in the ML TMD. In the moiré bilayer, consider the hole filling $\nu = 1$ as the new vacuum and convert the empty sites to electrons (filling δ) by particle-hole transformation. The holes in the ML TMD are bound to electrons in the moiré bilayer to form excitonic insulators with E-dependent exciton density δ. Figures are adapted from Ref. [82, 84].

Chapter 3

Experimental Methods

In this chapter, I will introduce the experimental and technical requirements for the experimental results presented in Chapter 4-7. A detailed description of sample fabrication and optical measurements is provided. Fabrication of reproducible high-quality samples is one of the most important things for vdW heterostructure research.

3.1 PDMS-based all dry transfer

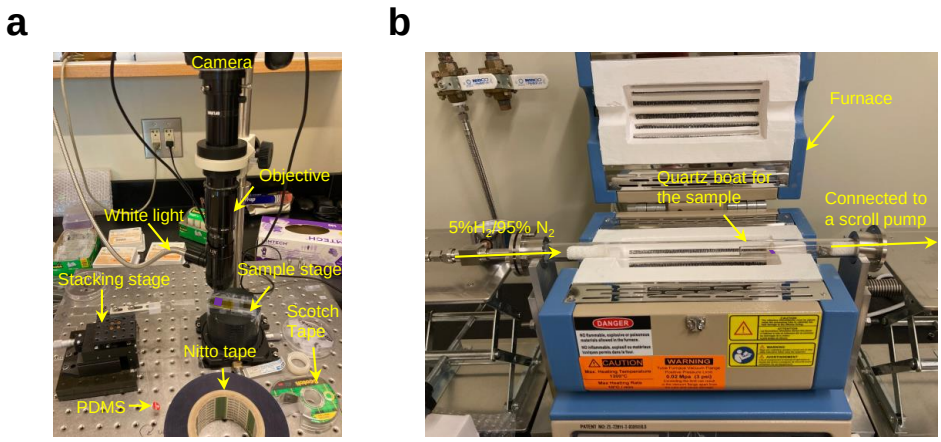

Figure 3.1: PDMS-based transfer (**a**) and annealing (**b**) setup.

The polydimethylsiloxane (PDMS)-based dry transfer is one of the first tech-

niques to stack the TMD vdW heterostructures[88]. The entire process includes TMD flake exfoliation, substrate preparation, TMD flake transfer and sample annealing (Fig. 3.1), as described below:

Step 1: Exfoliate TMD flakes on the PDMS film. Cut a PDMS square (1×1 cm) from the Gel-Pak PF film with 6.5 mil thickness and place it on a clean glass slide without bubbles. Next, use the blue Nitto tape to remove a small piece from bulk TMDs, graphite (NGS) or hBN and copy the small piece into a reasonable area. Press the blue tape on the PDMS and ensure the interface is flat. Wait several hours before peeling off the tape and check the exfoliated monolayer or few layers on the PDMS under the microscopy. The thickness of the flakes is identified by the optical contrast or AFM.

Step 2: Pattern the electrodes on the substrate by electron beam lithography (EBL). First, we need to spin coat the clean silicon (Si) substrate following two steps: (1) Dispense MMA onto the silicon substrate, rotate it on a spinner (3000 rpm 35 s/7000 rpm 5 s) and bake at 150 °C for one minute. (2) Dispense PMMA onto the silicon substrate, rotate it on a spinner (3000 rpm 35 s/7000 rpm 5 s) and bake at 150 °C for three minutes. After spin coating the polymer layers, use scanning electron microscopy (SEM) to determine the specimen current for different structures and also focus on the sample. EBL is then utilized to inject electrons into the polymer following the CAD-designed pattern. Thereafter, the silicon substrate is immersed into MIBK:IPA (1:1, or 3:1 for fine structures) developer for 15-18 seconds and cleaned by IPA to expose the pattern. In the end, utilize thermal evaporation to deposit 5 nm Cr/85 nm Au on the substrates and then put them into acetone to lift off the extra gold.

Step 3: Transfer the TMD flakes on the substrate with as-patterned electrodes. First, prepare the stamp with target flakes as in Fig. 3.3 a and fix it on the stacking stage as in Fig. 3.1a. Then, we attach the substrate to the rotatory sample stage.

Use the white light and camera to find the flakes and substrate, and keep tracking the distance between them when lowering the height of the flake stamp. When the stamp and substrate start to touch, slowly make the touch area cover the target flake. Wait for half an hour and then slowly level up the stamp until it is detached from the substrate. We can find the flakes are now transferred to the substrate. Repeat this transfer process until we have stacked all flakes. This transfer process follows a bottom-up order, starting from the bottommost flake to the topmost flake.

Step 4: Anneal the sample in 5% H_2/95% N_2 at 125°C for 2 h. This is to form a good interface between flakes as the polymer residue within the interface aggregates and leaves other parts clean. Without annealing, there is no interlayer exciton emission from the PDMS-stacked vdW heterostructures. The annealing is conducted in the furnace (Fig. 3.1 b). Assure to open the gas valve slowly so that the dust will not be blown to the substrate.

Step 5: Wire bond the electrodes to the chip carrier. A chip carrier consists of a copper plate fit to the piezoelectric stage and a printed circuit board (PCB) with soldered pins grounded on an anti-static foam. Sapphire is used to space the substrate and the chip carrier. The sample substrate is fixed on the sapphire by silver paste. Wait for the silver paste to be dry, and wire bond the electrodes on the substrate to the PCB.

3.2 PC-based pick-up technique

The polycarbonate (PC)-based pick-up technique is a new techinque[89] to fabricate vdW heterostructure with a much cleaner interface compared to PDMS-based transfer. The pick-up setup consists of the motorized stacking arm and sample stage with a temperature controller module in the glovebox (Fig. 3.2). Though PDMS-based transfer has no temperature requirements, the PC-based transfer requires elevated

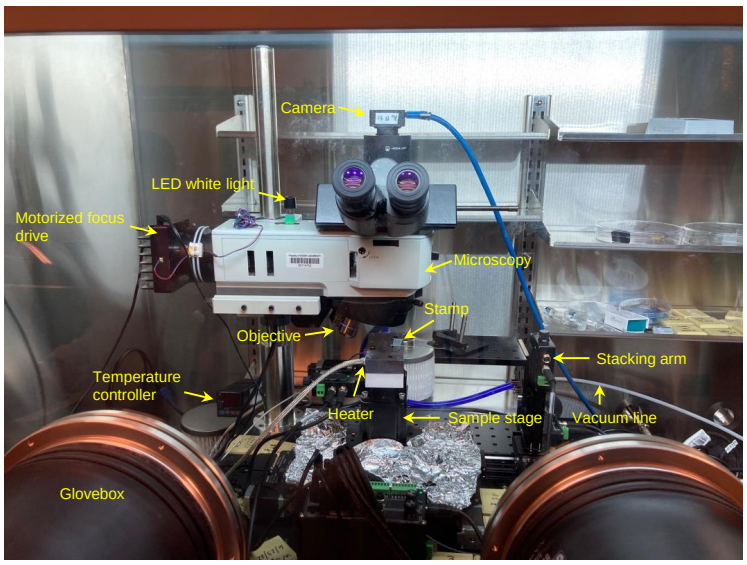

Figure 3.2: Pick-up transfer setup.

temperature so we need an additional temperature controller. The glovebox can avoid the degradation of TMD flakes in the atmosphere and prevent dust contamination. The complete procedure to fabricate a sample via PC-based pick-up technique is as below:

Step 1: Cut the silicon wafer using a diamond cut pen. Cut a clean scratch on the wafer edge and knock half of the wafer off on a glass slide along its edge. Use nitrogen to blow the silicon substrates without IPA or acetone. The Si substrate has 285 or 300 nm SiO_2 on top of the heavily p-doped Si (University Wafer).

Step 2: Exfoliate monolayer TMDs, few-layer graphite and 20-40 nm hBN on the clean Si substrate using Scotch tape. Press very hard for TMD flakes and heat at 100 °C for 3 minutes. Wait for the substrate to cool down to room temperature and then slowly peel off the tape.

Step 3: Pattern the electrodes on the substrate by EBL following the same procedure in PDMS transfer.

Step 4: Make a stamp with PC film on top of PDMS droplet or PPC droplet/PDMS square. The schematic of two kinds of stamps is shown in Fig. 3.3b, c. The PDMS

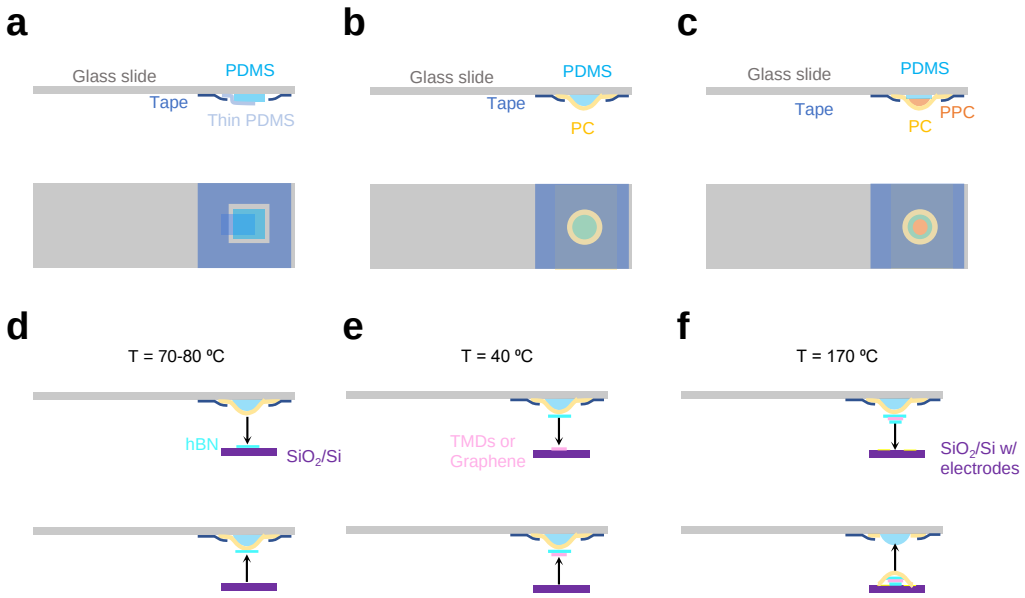

Figure 3.3: PDMS or PC based sample fabrication. **a.** The stamp for PDMS-based all-dry transfer technique. The exfoliated ML TMDs are on the thin PDMS, which is placed on top of the thick PDMS to produce a curvature. The Scotch tape is used to fix the thin PDMS. **b.** The PC/PDMS droplet stamp for pick-up. **c.** The PC/PPC droplet/PDMS stamp for pick-up. **d.** Schematic of picking up the top graphite or top hBN at 70-80 °C. **e.** Schematic of picking up the TMDs and other remaining layers at 40 °C. **f.** Schematic of dropping down the whole stack on the substrate with pre-patterned electrodes at 170 °C. The PC is melted on the stack, which needs to be removed in the chloroform bath.

droplet is made by heating mixed standard curing agent and base (1:10) in the oven (>150 °C) for > 30 mins. As for PPC droplet/PDMS square, PDMS square (1x1 mm) is from Gel-Pak PF film with 17 mil thickness and PPC droplet is obtained by heating the PPC solution (anisole, >20%) on the PDMS square for 1-3 min at 120 °C. To prepare the PC film, place a clean glass slide on the cleanroom paper, add a few drops of 6% PC solution (dissolved in chloroform, mass ratio), and then place another clean glass slide on top of the solution. After pressing slightly to spread the solution between the two slides, slide them apart and let dry for 10 mins. Use Scotch tape and a razer to select a circle or square of the PC film and attach it to the PDMS droplet or PPC droplet. Make sure to have enough tension when attaching the PC film, since large tension can help prevent ripples. If the PDMS droplet is not clean, use another commercial PDMS square on the PDMS droplet. Put the whole stamp into the vacuum chamber for several hours to avoid detachment during pick-up.

Step 5: Design the heterostructures using a vector graphics design software (InkScape) by extracting all the edges of the relevant flakes and placing them in the desired positions. Make sure the top graphite gate, bottom graphite gate and contact positions are reasonable. Separate top and bottom gates by TMDs and hBN could increase the accessible voltage range.

Step 6: Stack the vdW heterostructure onto the substrate with pre-patterned electrodes. In the beginning, pick up the bottom hBN (Fig. 3.3d, 70-80 °C for PC/PDMS and 60-70 °C for PC/PPC/PDMS) and bottom graphite (Fig. 3.3e, 40 °C), and drop them down on a Si substrate with pre-patterned electrodes(Fig. 3.3f, PC films detached at 130-150 °C, and peeled off at 170 °C or melted at 170 °C and then lift up with a faster speed μm/s). Immerse the dropped-down hBN and bottom graphite into chloroform to dissolve PC film and then anneal in 5% H_2/95% N_2 at 350°C for 3 hours to remove the PC residue. Afterward, pick top graphite/top hBN/other layers at 40 °C or room temperature and drop down the whole stack on the bottom hBN

and bottom graphite at 170 °C. After finishing the drop-down of the sample, dissolve the PC and PPC in the chloroform bath overnight and use a nitrogen gun to gently blow dry normally to the sample substrate to avoid accidental folding. During the pick-up, match the design in InkScape with 10% magnification to 20× in the camera with 100% magnification. It is better to keep the temperature the same during the pick-up process, or else the thermal expansion or contraction could deform the stamp (we can keep the substrate at the center of the sample holder to reduce this effect). After heating up to 80 °C, it could cause the deformation of the PPC stamp when we are trying pickup at that high temperature or wrinkles on the PC when returning to a lower temperature.

Step 7: Wire bond the electrodes to the chip carrier and load the sample into the cryostat for optical and electrical measurements. When we load the sample, ground ourselves to avoid static discharge and clean the chamber to ensure a clean high-vacuum environment for the measurements.

3.3 Cryogenic optical measurement setup

We use two home-built, low-temperature (∼4 K) microscope setups for optical measurements. One is a closed-cycle cryostat (AttoDry 800) with electrical connection (Fig. 3.4); another cryostat (BlueFors cryogenics) is with both magnetic field from -8 T to +8 T and electrical connection (Fig. 3.5). A piezoelectric controller (Attocube systems) is used to position the sample. We use an achromatic lens (NA = 0.42 for AttoDry 800 and NA = 0.63 for BlueFors cryogenics) to collect the PL emission or reflected white light and send it to a high-resolution (focal length: 500 mm for AttoDry 800 and 750 mm for BlueFors cryogenics) spectrometer (Princeton Instrument HR-500 for AttoDry 800 and Princeton Instruments SP-2750 for BlueFors cryogenics). The signal is dispersed by a 1200 g/mm (for localized excitons) or 300 g/m grating

(for free excitons) blazed at 750 nm. The PL detector is a charge-coupled device (Princeton Instrument PIXIS-400 CCD for AttoDry 800 and PyLoN CCD for Blue-Fors cryogenics). For continuous-wave (CW) photoluminescence (PL) measurements, the excitation laser is a MSquared mode-hop-free tunable CW Ti:Sapphire laser with a resolution of 0.1 pm or a HeNe laser with a fixed wavelength of 632.8nm. The Ti:Sapphire (HeNe) laser has a spot size of ~ 1 μm (~ 2 μm). For reflectance contrast measurements, a halogen lamp (Thorlabs SLS201L) or 740 nm LED (Thorlabs M740F2) serves as the white light source. The incident laser polarization is controlled by using a polarizer together with a quarter waveplate for Attodry setup, while it is controlled by using a polarizer together with a liquid crystal variable retarder for Bluefors setup. Polarization-resolved measurements are performed by using a $\lambda/4$ waveplate (achromatic, 690-1200 nm) placed before a Wollaston prism. Circularly polarized emission is converted into linearly polarized light through the $\lambda/4$ waveplate. The s- and p- components of linear polarized light are then displaced by the Wollaston prism. Another achromatic $\lambda/4$ waveplate is placed after the Wollaston prism to convert the linearly polarized light into a circularly polarized signal, in order to avoid the sensitivity to the grating efficiency.

For time-resolved PL measurements, typically for lifetime measurements, we use 640 nm ps pulse laser (Picoquant LDH-640) as the excitation. The PL emission is then spectral filtered and directed to an avalanche photodiode (APD). The APD electrical signal together with the pulse laser synchronization signal is sent to a time-correlated single photon counting system (TCSPC, PickHarp 300), in order to acquire the time evolution of emitted photon number and extract the lifetime.

In all measurements, the magnetic field B is applied perpendicular to the plane of the sample with a resolution of 1 mT. The DC voltage is applied to the graphite gates with Keithley 2400 sourcemeters. If we need to modulate the voltage input (AC+DC), we use an arbitrary waveform generator (Agilent 33220 A) to apply the

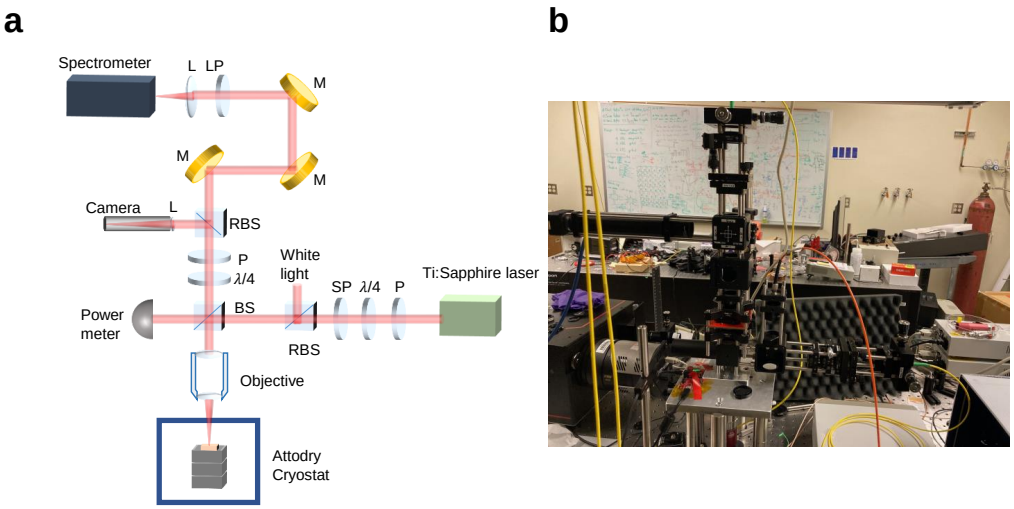

Figure 3.4: Attodry optical measurement setup. **a.** Schematic of optical setup. L is a lens, LP is a long-pass filter, SP is a short-pass filter, M is a mirror, BS is a beamsplitter, RBS is a removable beamsplitter, P is a polarizer, $\lambda/4$ is the quarter waveplate. **b.** Picture of the Attodry optical setup.

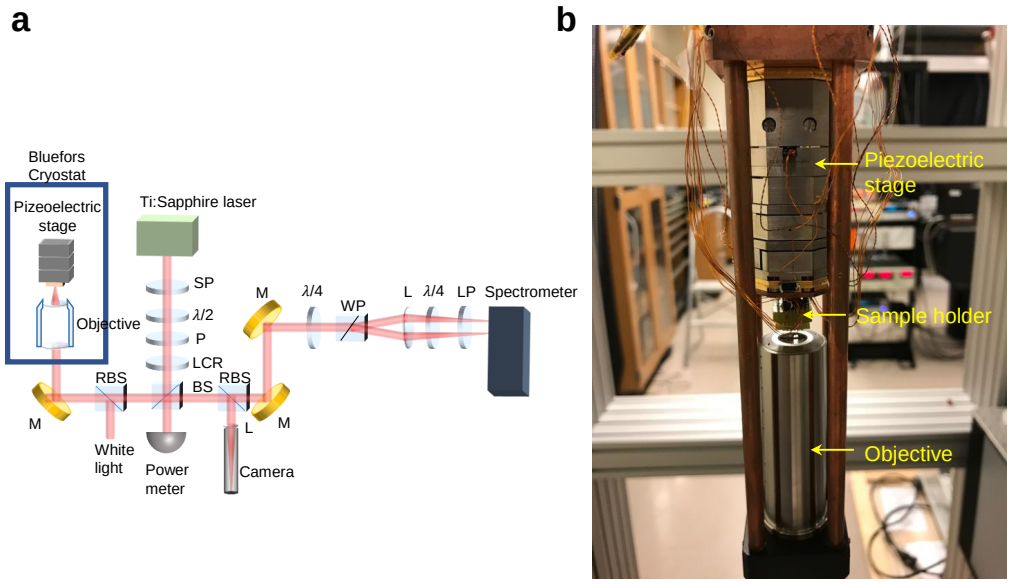

Figure 3.5: Bluefors optical measurement setup. **a.** Schematic of optical setup. $\lambda/2$ is a half waveplate, LCR is a liquid crystal retarder, and WP is a Wollaston prism. **b.** Picture of the optical setup inside the cryostat.

voltage to the sample, which is synchronized with a lock-in amplifier (SR830). The voltage modulated optical signal is collected by a photodiode and sent to the lock-in amplifier for high signal-to-noise ratio.

Chapter 4

Few-body Interactions in 2D Materials

In this chapter, I will present the experimental observation of few-body interactions in a $WSe_2/MoSe_2$ heterobilayer. By trapping the IXs to be localized dipoles, we find the repulsive dipole-dipole interactions between them are an order of magnitude larger than the emission linewidth, giving rise to strong quantum nonlinearity. The main findings presented in this chapter are published in Nature Materials[1].

4.1 Previous measurements on localized interlayer excitons

In Chapter 2, we have introduced that the localized intralayer exciton in ML TMDs is a single photon source with sharp linewidths, which however has no permanent out-of-plane dipole moment. On the other hand, interlayer excitons have permanent out-of-plane dipole moment, the energy of which is highly tunable by electric field. Combining these two ingredients, localized interlayer excitons (IXs) are good candidates to study few-body interactions between single dipoles with tun-

able emission energy in a perpendicular electric field. Recently, observation of localized IXs with sharp linewidth was reported in vdW heterostructures, especially in $WSe_2/MoSe_2$[31]. The stacking order dependent circular polarization and g factor (defined as $\frac{1}{\mu_B B}(E_K - E_{K'})$) suggest the IXs are moiré trapped excitons, instead of defect trapped excitons [31, 90]. As shown in Fig. 4.1, AA stacking produces localized IXs with cross-polarized emission and g factor of 6.86, while AB stacking produces localized IXs with co-polarized emission and g factor of -16.11. Furthermore, the second-order quantum coherence function $g^{(2)}$ shows anti-bunching with a value smaller than 0.5, indicating that localized IXs are single photon emitters[91].

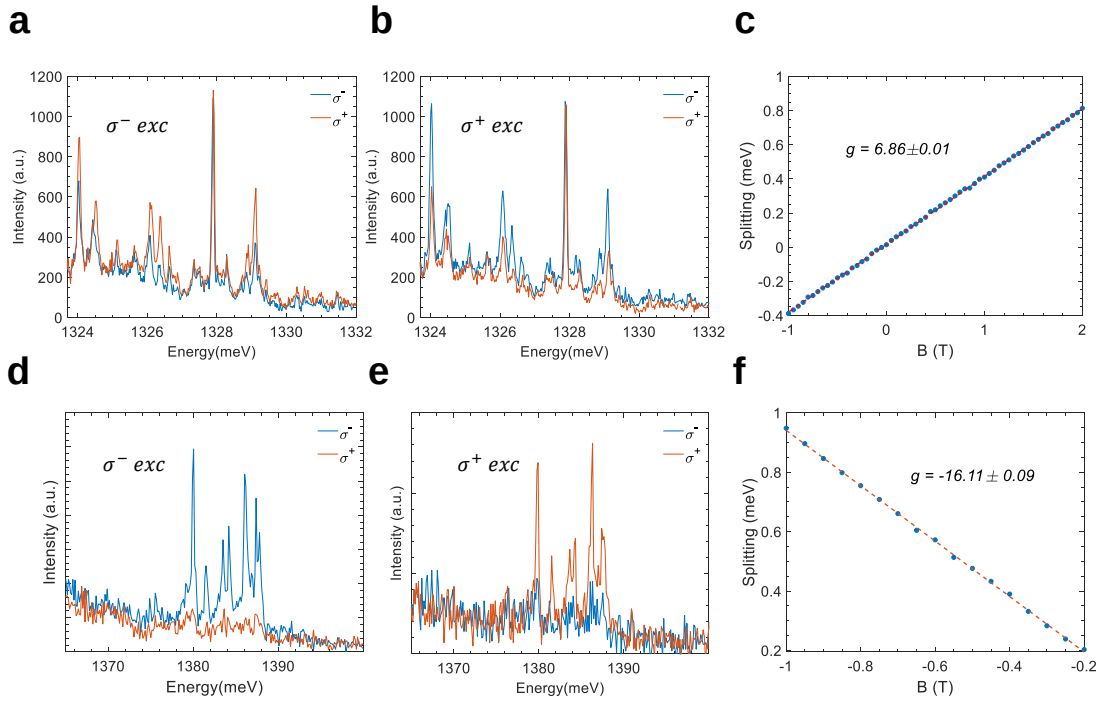

Figure 4.1: Polarization resolved and magneto-PL dependence of PL spectra in AA and AB stacking $WSe_2/MoSe_2$. **a, b.** σ^- (**a**) and σ^+-polarized (**b**) excitation show that the neutral top dipoles are cross-polarized at $B = 0$ for AA stacking. **c.** Zeeman splitting of a quantum emitter versus B yields a g-factor of 6.86 for AA stacking. (**d, e.**) σ^- and **d, e.** σ^- (**d**) and σ^+-polarized (**e**) excitation show that the neutral top dipoles are co-polarized at $B = 0$ for AA stacking. **f.** The Zeeman splitting versus B under linear excitation gives a g-factor of -16.11 for AB stacking. The excitation laser energy is at 1.70 eV and 100 nW for AA stacking and 600 nW for AB stacking.

4.2 Experimental details

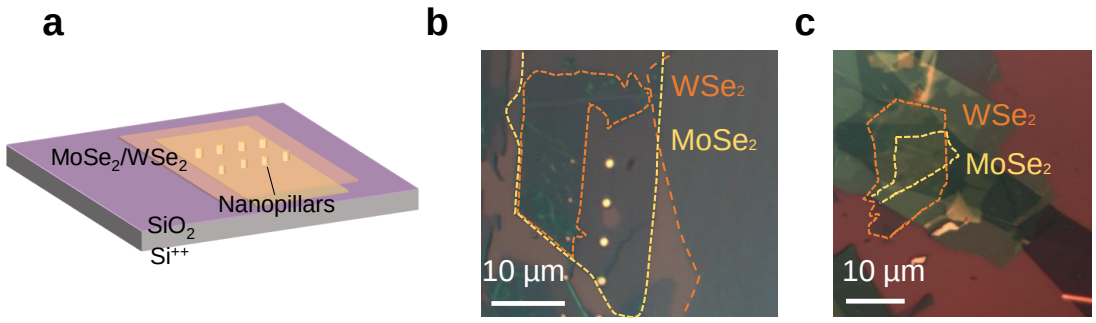

Figure 4.2: Sample design (**a**) and pictures (**b, c**). Monolayer WSe_2 ($MoSe_2$) is outlined in orange (yellow) dashed line.

In order to obtain localized IXs, we fabricated a $WSe_2/MoSe_2$ heterobilayer on top of nano-pillars (Fig. 4.2a). We use electron beam lithography and thermal evaporation to fabricate the pillar arrays (5 nm Cr/85 nm Au) on 300 nm SiO_2/Si substrates. A thin layer of SiO_2 (3 nm) is subsequently deposited on pillars by using atomic layer deposition as the spacer to avoid the quenching of the PL emission. We transfer the mechanically exfoliated samples by PDMS-based dry transfer method on the as-patterned pillars, with monolayer WSe_2 (HQ graphene) on top of monolayer $MoSe_2$ (HQ graphene) as shown in Fig. 4.2b. The $MoSe_2/WSe_2$ sample with electrical contacts is further encapsulated between two hexagonal boron nitride (HQ graphene) layers with graphite (NGS) top and bottom gates (Fig. 4.2c). After the stacking, both samples are annealed in 5% H_2/95% N_2 at 125°C for 2 h.

To find localized IXs in our samples, we conduct low-temperature ($\sim$ 4 K) PL measurements using quasi-resonant excitation close to the WSe_2 or $MoSe_2$ intralayer resonance. The excitation power is as low as $\sim$ nW, since single quantum emitters can easily saturate at μW. After spatially scanning the whole sample, we find localized emission in the IX emission energy range with as sharp linewidth as 110 μeV (Fig. 4.3a, b). Moreover, the time traces of these sharp emission peaks exhibit spectral

jittering that is characteristic of localized quantum emitters (Fig. 4.3c). Furthermore, the PLE measurement (Fig. 4.3d) and electric field induced Stark shift (Fig. 4.3e) are as expected for an IX, comprising electron in the $MoSe_2$ (bottom layer) and hole in the WSe_2 (top layer). The Stark shift rate of $\sim$400 meV/nm$\cdot$V^{-1} gives the dipole moment of 0.7 $e\cdot$nm, consistent with the interlayer distance. The above observations establish that we have observed localized IXs with out-of-plane dipole moments. Their energy can be tuned by more than 100 times their linewidth via applying E field, which is hard to realize for ML quantum emitters. We note that the localized IX emission energies are distributed in a range of 1250-1450 meV, possibly resulting from the local strain variation.

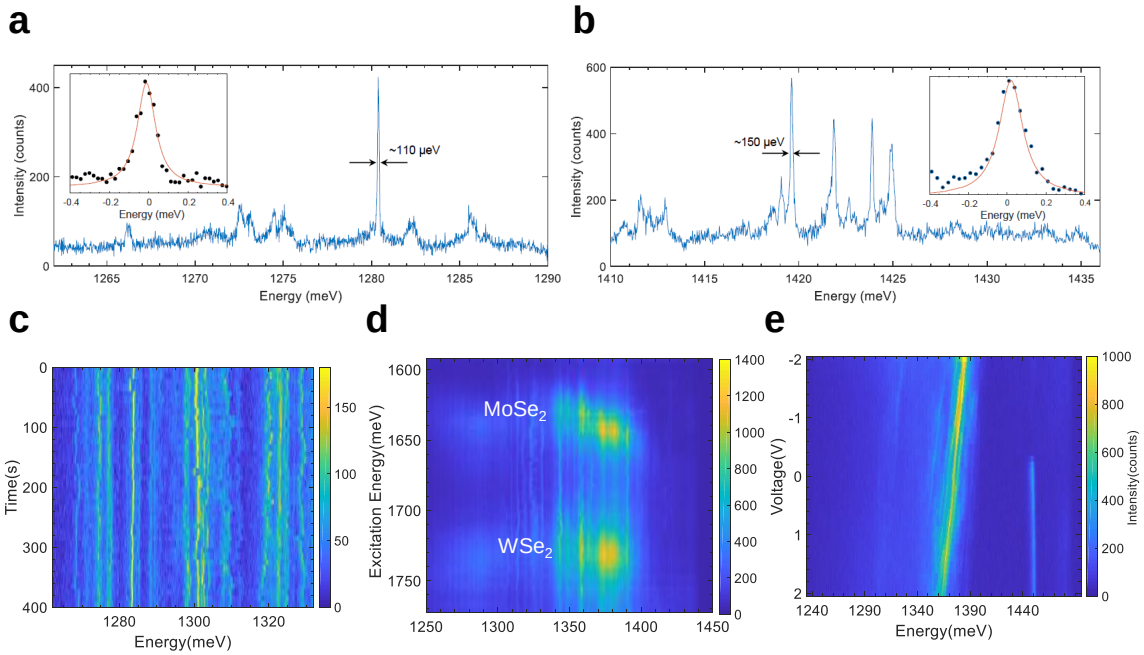

Figure 4.3: Localized IXs in $WSe_2/MoSe_2$ at low temperature. **a, b** PL spectra of localized IXs showing sharp linewidths of $\sim$110 μeV (**a**) and $\sim$150 μeV (**b**).**c,** Time dependent PL emission of localized IXs. **d,** PLE of localized emitters. All the quantum emitters show local resonances around $\sim$1640 meV ($MoSe_2$ resonance) and $\sim$ 1730 meV (WSe_2 resonance). **e,** Electric field tuning of a localized IX. As the gate voltage sweeps from -2 to +2 V, the localized IX at $\sim$1380 meV exhibits a red shift of $\sim$20 meV, confirming the existence of an out-of-plane dipole moment.

4.3 Observation of repulsive dipole-dipole interactions between localized IXs

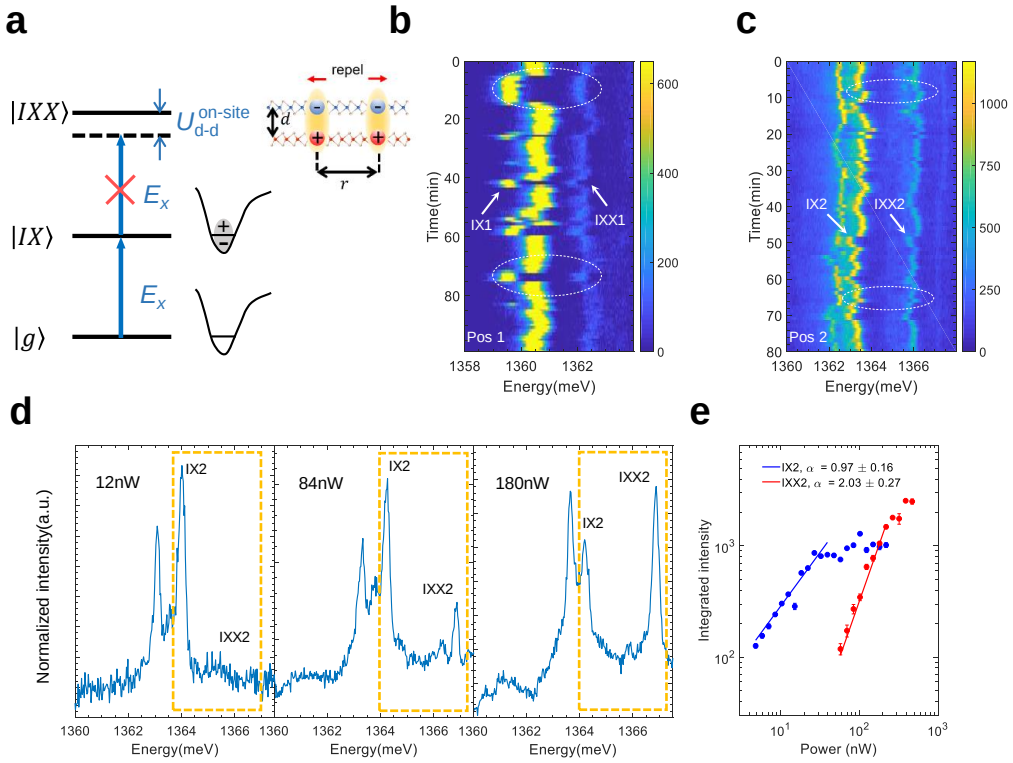

Figure 4.4: Dipole-dipole interactions between localized IXs. **a.** Energy diagram of localized interlayer optical excitation for single (IX) and double occupancy or biexciton (IXX) in a potential well. The energy of IXX ($|IXX\rangle \rightarrow |IX\rangle$) is increased by an on-site dipole-dipole interaction $U_{\mathrm{dd}}^{\mathrm{on-site}}$ compared to IX energy ($|IX\rangle \rightarrow |g\rangle$). **b, c.** Time dependence of PL emission from localized IX and IXX at two sample positions. White arrows and dotted circles highlight the same spectral jittering patterns from IX1-IXX1 (**b**) and IX2-IXX2 (**c**), indicating that they originate from the same potential well. **d.** PL spectra of IX2-IXX2 under different excitation powers. Only IX2 exists at low power (12 nW, left). Biexciton IXX2 shows up at intermediate power (84 nW, middle) and dominates at high power (180 nW, right). **e.** Power dependence of integrated PL intensity for IX2-IXX2. The fitting was done with a power law function, $I \propto P^{\alpha}$. α is 2.03 for IXX2, which is twice of 0.97 for IX2 and consistent with biexciton assignment. The excitation wavelength $\lambda = 745$ nm in panel **b-d**. Incident power $P = 20$ nW in panel **b**, and $P = 250$ nW in panel **c**.

As each localized IX is considered as a single dipole, we can investigate dipole–dipole interactions by adding one or more additional IXs into the same potential well. The

physical picture is illustrated in Fig. 4.4a. If we add one more IX in the trap occupied by another IX to form a biexciton state, compared to a single excitation ($|IX\rangle$) with energy E_X, there is an additional on-site energy cost ($U_{\mathrm{dd}}^{\mathrm{on-site}}$) arising from the repulsive dipole-dipole interaction between two IXs. Therefore, the magnitude of such interaction is manifested in the energy difference between the single and double occupancy states, given by

$$U_{\mathrm{dd}}^{\mathrm{on-site}} = \frac{1}{4\pi\epsilon_0\epsilon_r}\left(\frac{2e^2}{r} - \frac{2e^2}{\sqrt{r^2+d^2}}\right) \approx \frac{(ed)^2}{4\pi\epsilon_0\epsilon_r r^3}, \tag{4.1}$$

where d is the interlayer spacing and r is the inter-dipole distance. There is a contact term that we ignore here because we assume the distance between the two dipoles is much larger than the d (0.7 nm) (strongly bounded exciton), which is true for a moiré trap (5-10 nm). For certain tight confinement of IXs, we could reach a regime where effective dipole–dipole interaction(U_{dd}) is larger than the linewidth, reminiscent of dipole blockade in Rydberg atoms [92]. This implies a quantum nonlinearity where the presence of merely one additional exciton drastically modifies the optical response.

To test whether we are in such a regime, we increase the exciton densities by ramping up the excitation laser power. With increased excitation power, Fig. 4.4b, c are the time-trace PL emission at sample position Pos 1 and Pos 2, respectively. For both positions, two peaks with 2 meV energy spacing show the same spectral jittering pattern (∼1360 and ∼1362 meV for Pos 1, ∼1364 and ∼1365 meV for Pos 2), as highlighted by white arrows and dotted circles. This behavior suggests that the two peaks belong to the excitations in the same trap. A similar synchronized jittering feature with varied energy spacing from 1 to 5 meV is also observed in other positions (see Appendix B). However, this is not a shared feature by all the peaks in the spectra, as evident by the distinct jittering pattern of the lowest-energy peak in Fig. 4.4c. The simultaneously jittering two-peak structure can be exciton

complexes, such as charged exciton and biexciton, which can be distinguished by excitation power-dependence of emission intensity (Fig. 4.4d). The power-dependent PL spectra show that only the red peak exists at the lowest power (12 nW) and the blue peak appears at intermediate power (84 nW) and dominate at higher power, suggesting that the blue peak is possibly a biexciton. We thus assign the red and blue peaks as IX and IXX, respectively. We further plot the integrated intensity of each PL emission peak as a function of excitation power, and fit the data with a power law function, $I \propto P^{\alpha}$ (Fig. 4.4e). The red peak IX2 exhibits a linear power-law behavior with $\alpha_X = 0.97 \pm 0.16$ before the saturation, and the blue peak IXX2 shows a super-linear power dependence with $\alpha_{XX} = 2.03 \pm 0.27$. The super-linear power dependence of the blue peak ($I \propto P^{2\alpha_X}$) is consistent with our assignment that the blue peak is a biexciton.

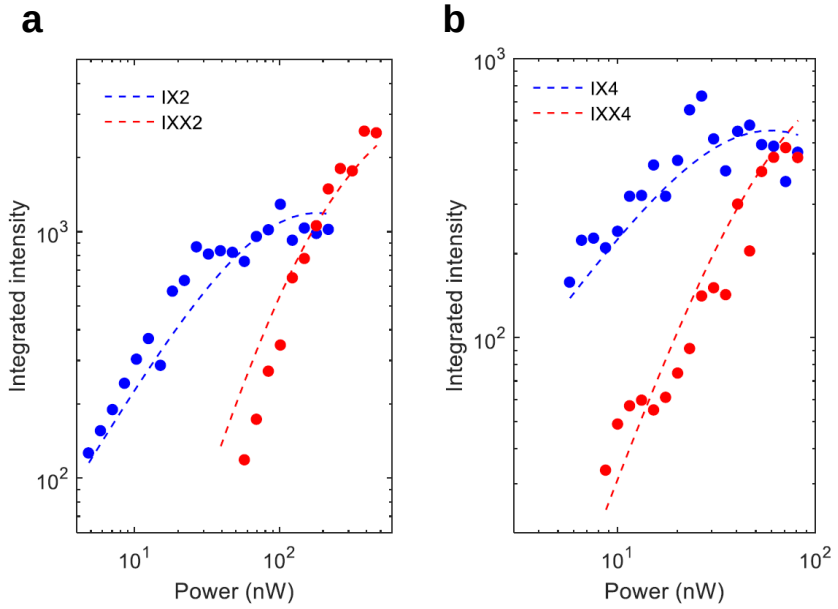

Figure 4.5: Fitted power-dependent intensities of IX2/IXX2 (**a**) and IX4/IXX4 (**b**).

Due to the limited data points before the saturation, we consider a three-level rate-equation model to capture the saturation behavior[93, 94]. The three levels are

the ground state (N_0), interlayer exciton state (N_{IX}) and biexciton state (N_{IXX}). As we are assuming the localized interlayer exciton to be a single photon emitter, the occupation number N_0, N_{IX}, N_{IXX} become occupation probability ρ_0, ρ_{IX}, ρ_{IXX}. Under excitation power P_{exc}, the rate equations that determine the probabilities of excitons IX and biexciton IXX are given by,

$$\frac{\partial \rho_{IX}}{\partial t} = -\frac{\rho_{IX}}{\tau_{IX}} - a\rho_{IX} + \frac{\rho_{IXX}}{\tau_{IXX}} + a\rho_0,$$
$$\frac{\partial \rho_{IXX}}{\partial t} = -\frac{\rho_{IXX}}{\tau_{IXX}} + a\rho_{IX},$$

where τ_{IX}, τ_{IXX} are the radiative recombination lifetimes of IX and IXX. a is the generation rate, which is proportional to P_{exc} through a scaling factor b such that, $a = bP_{\text{exc}}$. The total occupation probability is normalized to unity -

$$\rho_0 + \rho_{IX} + \rho_{IXX} = 1.$$

To capture the power dependence with a minimalistic model, we ignore any non-radiative decay. Solving the above equations for stationary states, we can get the PL intensity of IX and IXX as -

$$I(IX) = c\frac{\rho_{IX}}{\tau_{IX}} = \frac{ca}{1 + a\tau_{IX} + a^2\tau_{IX}\tau_{IXX}},$$
$$I(IXX) = c\frac{\rho_{IXX}}{\tau_{IXX}} = \frac{ca^2\tau_{IX}}{1 + a\tau_{IX} + a^2\tau_{IX}\tau_{IXX}},$$

where c relates the number of excitons/biexcitons to the experimentally measured intensities. Besides the scaling factors b and c, the only parameter in the model is the ratio of τ_{IX} to τ_{IXX} which is a free parameter and is assumed to be close to unity. In the low power regime (a is small), the intensities of IX and IXX scale with P_{exc} and P_{exc}^2, respectively. This is consistent with the power law fitting for IX2-IXX2 (Fig. 4.4e). In the high-power regime (a is large), the IX intensity saturates and starts

to decrease, while the IXX intensity increases at the expense of IX and eventually saturates as well. By taking adequate b, c and reasonable τ_{IX}, τ_{IXX} (~ 1), we find the calculated intensities from rate equations can reasonably fit our experimental results of IX2-IXX2 (IX4-IXX4) with $\tau_{IXX}/\tau_{IX} = 1.2$ (1.5) (Fig. 4.5), confirming our assignment of exciton and biexciton peaks.

Having confirmed that the red and blue peaks are single and double occupancy, the energy spacing between them is then the on-site dipole-dipole repulsion U_{dd} (Fig. 4.4a). U_{dd} $\sim$2 meV is one order of magnitude larger than the linewidth 0.1 meV, signifying that we are in the strong non-linearity regime. One interesting question arising from the blueshift is whether we can call such a double occupancy state as a biexciton. Qualitatively speaking, the motion of the two residing excitons gets correlated due to repulsive interactions so it is reasonable to call it as a biexciton. To be more specific, the centre-of-mass wavefunction of each exciton is squeezed to avoid overlap and lower the dipolar repulsion. The modified COM wavefunction of each exciton is no longer that of the ground state but has weight from higher energy excited states. The different energy spacing (1-5 meV) between exciton and biexciton (see Appendix B) indicates that the dipolar interaction varies among different localized interlayer excitons. As the dipole moment can be assumed to be constant given by the separation of 0.7 nm between the two monolayers, variation in U_{dd} must arise from difference in confinement lengths and consequently interexcitonic distances. To estimate the confinement length from U_{dd}, we assume that the interlayer excitons are confined in a harmonic trap with a width larger than the excitonic Bohr radius such that the dipoles can be treated as point particles and their dipole-dipole interaction is $U_{\mathrm{dd}} \approx \frac{(ed)^2}{4\pi\epsilon_0\epsilon_r r^3}$.

Our simple classical electrostatic model is based on the Ref. [95]. Both the kinetic energy and the overlap of the excitonic wavefunctions are neglected, so the total

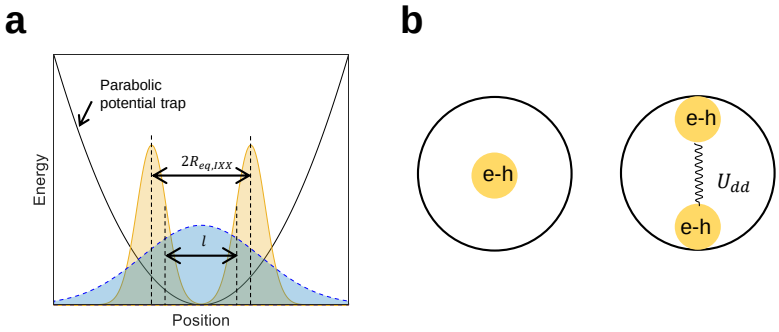

Figure 4.6: Configurations of exciton and biexciton in the harmonic potential well. **a.** Wave packet configurations of exciton and biexciton. l is the confinement length of the potential well. $R_{\mathrm{eq,IXX}}$ is the distance from center of the well to either exciton in the biexciton configuration. **b.** Point particle configurations of exciton and biexciton.

exciton energy in a parabolic trap is given by

$$E_{NIX} = NE^0_{IX} + \sum_i \frac{M\Omega^2}{2} r_i^2 + \sum_{i<j,i,j=1,\ldots,N} \frac{t^2}{4\pi\epsilon_0\epsilon_r r_{i,j}^3}, \tag{4.2}$$

where N is the number of excitons, E^0_{IX} is the optical energy of the exciton, Ω is the characteristic confinement frequency of an exciton in the trap. $M = m_e^* + m_h^*$ is the total exciton mass, $t = e \cdot d$ is the dipole moment, r_i is the coordinate of i-exciton, and $r_{i,j}$ is the distance between i-, j-exciton. In order to calculate the emission energy of biexciton, we only need to consider the single exciton and biexciton energies

$$E_{IX} = E^0_{IX} + \frac{M\Omega^2}{2} r_1^2,$$

$$E_{IXX} = 2E^0_{IX} + \frac{M\Omega^2 r_1^2}{2} + \frac{M\Omega^2 r_2^2}{2} + \frac{t^2}{4\pi\epsilon_0\epsilon_r r_{1,2}^3}.$$

The emission energies (or PL peak energies) of exciton and biexciton are given by the transition from the single exciton state to the ground state and the biexciton state

to the single exciton state, respectively,

$$\hbar\omega_{IX} = E_{10} = E_{IX,\min},$$

$$\hbar\omega_{IXX} = E_{21} = E_{IXX,\min} - E_{IX,\min},$$

where the $E_{IX,\min}$, $E_{IXX,\min}$ are the minima of E_{IX}, E_{IXX}, that is, the ground states of IX and IXX, respectively. As shown in Fig. 4.6, the ground state of IX means the exciton stays at the lowest potential energy; for the biexciton IXX, due to the repulsive on-site dipole-dipole interaction (U_{dd}) between two excitons, the ground state corresponds to a diatomic geometry with $r_1 = -r_2 = \frac{1}{2}r_{1,2} = R_{IXX}$,

$$E_{IX,\min} = E^0_{IX},$$

$$E_{IXX,\min} = 2E^0_{IX} + U_{\mathrm{dd}} = 2E^0_{IX} + 2\frac{M\Omega^2 R^2_{eq,IXX}}{2} + \frac{t^2}{32\pi\epsilon_0\epsilon_r R^3_{eq,IXX}},$$

where $R_{eq,IXX} = (\frac{3t^2}{64\pi\epsilon_0\epsilon_r M\Omega^2})^{\frac{1}{5}}$ is the solution for $\frac{dE_{IXX}}{dR_{IXX}} = 0$. Plugging the $R_{eq,IXX}$ into above equations, we can get

$$\hbar\omega_{IXX} = E^0_{IX},$$

$$\hbar\omega_{IXX} = E^0_{IX} + U_{\mathrm{dd}} = E^0_{IX} + [(\frac{3}{16})^{\frac{2}{5}} + (\frac{1}{6})^{\frac{3}{5}}][\frac{M^3\Omega^6 t^4}{(4\pi\epsilon_0\epsilon_r)^2}]^{\frac{1}{5}}.$$

Therefore, the energy spacing between the IX and IXX emission peaks is $\Delta E = \hbar\omega_{IXX} - \hbar\omega_{IX} = E_{21} - E_{10} = U_{\mathrm{dd}} = [(\frac{3}{16})^{\frac{2}{5}} + (\frac{1}{6})^{\frac{3}{5}}][\frac{M^3\Omega^6 t^4}{(4\pi\epsilon_0\epsilon_r)^2}]^{\frac{1}{5}}$.

In the $WSe_2/MoSe_2$ heterobilayer, $M = m^*_e + m^*_h \approx 1.15m_0$, where m_0 is the electron bare mass [58, 96], $t = 0.7$ e·nm [41], $\epsilon_r \approx (1 + 3.9)/2 = 2.45$ [19] for the SiO_2 substrate. Considering the energy spacings ΔE in Fig. 4.4b, c from main text are ~ 2 meV, we obtain the parabolic confinement frequency $\Omega \sim 2.51$ meV. The confinement frequency Ω is related to the confinement length l by $\Omega = \frac{\hbar}{Ml^2}$, so the

confinement length for our localized interlayer exciton is ~ 5.1 nm. The interexcitonic distance $2R_{eq,IXX}$ is calculated to be 7.1 nm using the same Ω. The Bohr radius a_B for IX is $\sim 1-2$ nm[76], smaller than the confinement length as well as the interexcitonic distance, which validates the model of rigid excitons.

4.4 Electric field tunability and valley dynamics

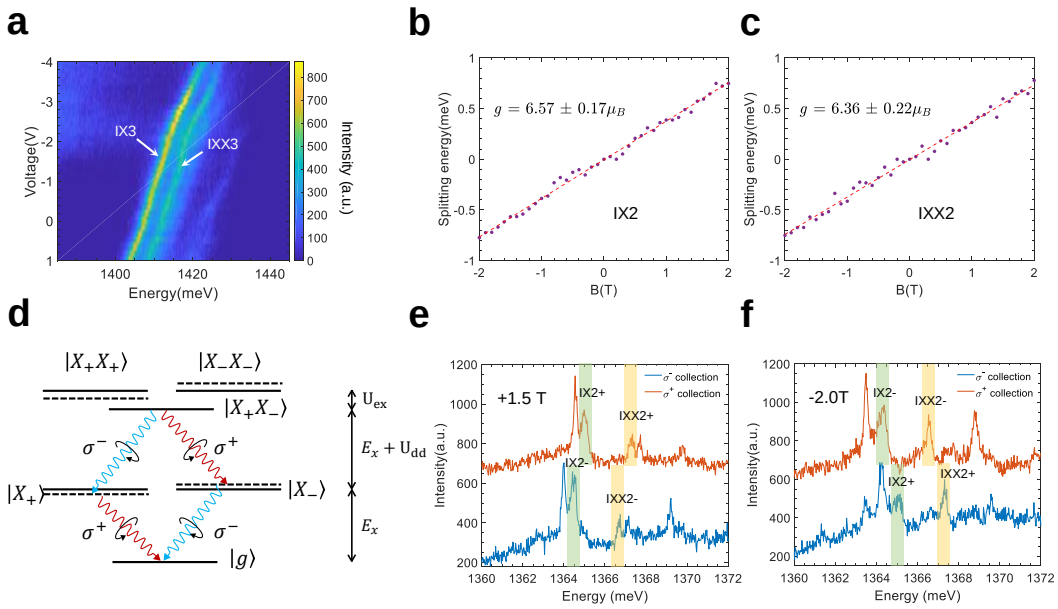

Figure 4.7: Dipole moment and spin-valley structure of localized interlayer excitons and biexcitons. **a.** Electric field dependent energy shifts of IX3 and IXX3. **b, c.** Magnetic field dependent splitting of IX2 (**b**) and IXX2 (**c**). **d.** Energy diagram and optical selection rule of IX and IXX. **e, f.** Polarization-resolved PL spectra of IX2 and IXX2 (highlighted in yellow dashed rectangles) at -2.0 T (**e**) and +1.5 T (**f**).

The aforementioned calculation assumes the localized biexciton and exciton carry the same dipole moment set by the interlayer distance. Though the relaxation and corrugation periodically modify the interlayer spacing, the variation (0.05 nm) is much smaller than the interlayer distance (0.7 nm), so we can consider biexciton and exciton carry similar dipole moment. The E field dependence in Fig. 4.7a shows that

localized interlayer exciton IX3 and biexciton IXX3 exhibit the same E-tuning rate, consistent with our assumption.

Besides an out-of-plane dipole, localized IXs and IXXs also have spin-valley degree of freedom. Similar g factor for IX2 (g_{IX}=6.57, Fig. 4.7b) and IXX2 (g_{IXX} = 6.36, Fig. 4.7c) suggests that they have the same magnetic moment coupled to spin-valley index. Depending on the two exciton spin-valley indices in the IXX, the optical transition helicity is varied. Following the optical selection rules[75, 76], localized IXs in K or K' valley ($|X_+\rangle$ or $|X_-\rangle$) couple to circularly-polarized light with opposite helicity ($\sigma^{\pm}$). Thus, IXX with opposite valley indices ($|X_+X_-\rangle$) have cross-polarized cascade emission when IXX with same valley indices ($|X_+X_+\rangle$ or $|X_-X_-\rangle$) emit co-polarized cascade photons (Fig. 4.7d). Furthermore, the same valley IXX species are triplet states with exciton-exciton exchange interaction, U_{ex}, while the opposite valley IXX species are singlet states without U_{ex}. The wavefunction of the lowest energy two-exciton state is antisymmetric in the spatial coordinates to minimize the dipolar repulsion. The bosonic nature of the exciton then implies that the antisymmetric singlet spin-valley configuration is more favorable. In other words, exciton-exciton exchange interaction U_{ex} is repulsive and raises the triplet energy (Fig. 4.7d). For a localized biexciton, U_{ex} is a two-body quantum exchange interaction, which can be estimated involving the excitonic wavefunctions as discussed in Ref.[76],

$$U_{\text{ex}} \sim \frac{1}{2\pi}(\frac{a_B^2}{w^2})E_b. \tag{4.3}$$

Using the binding energy E_b = 0.2 eV, Bohr radius a_B = 2 nm, interlayer spacing d = 0.7 nm, and previously calculated interexcitonic distance w = 7.1 nm, we have $U_{\text{ex}} \sim$ 2.5 meV. $|X_+X_+\rangle$ and $|X_-X_-\rangle$ energies are 2.5 meV above $|X_+X_-\rangle$, so they are unfavorable under thermalization at low temperature. As we only observe one biexciton peak, we tentatively suppose this peak is the lower energy $|X_+X_-\rangle$ biexciton.

To confirm that the biexciton peak corresponds to a spin-valley singlet configuration, we perform polarization-resolved measurements under magnetic field B. With a finite B, The degeneracy of $|X_+X_+\rangle$ and $|X_-X_-\rangle$, as well as X_+ and X_-, is lifted (dashed line in Fig. 4.7d), whereas $|X_+X_-\rangle$ state is hardly affected. Co-polarized emission is expected with all red (blue) peaks emitting σ^+ (σ^-) polarized light, as shown in the schematic of Fig. 4.7d. From polarization-resolved PL measurements (Fig. 4.7e, f), we observe that both red (IXX2$_-$) and blue peaks (IXX2$_+$) of IXX2 are co-polarized with the corresponding red (IX2$_-$) and blue (IX2$_+$) peaks of IX, consistent with the energy diagram in Fig. 4.7d.

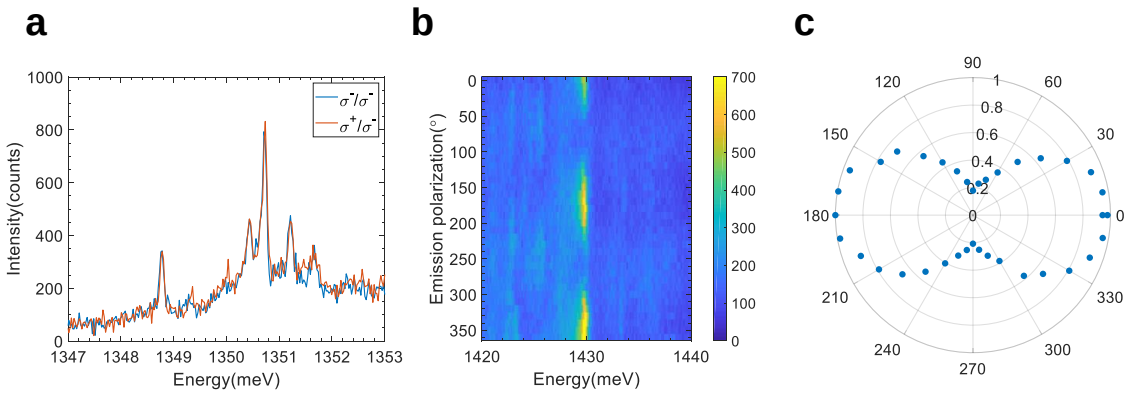

Figure 4.8: Polarization-resolved spectra of localized IXs under zero magnetic field. **a.** PL spectra of localized interlayer excitons show no dependence on incident circular polarization. **b.** Analysis of emission of localized interlayer excitons under linearly-polarized basis using a polarizer. **c.** Polar plot of total intensity of the sharp peak at ∼1430 meV in (**b**). The localized interlayer exciton shows a significant degree of linear polarization. Excitation is wavelength $\lambda = 745$ nm. Incident power $P =$ 100 nW and 50 nW in (**a**) and (**b**), respectively.

It should be noted that g factor of 6 is consistent with moiré trapped IXs in AA stacking $WSe_2/MoSe_2$ sample[31]. Nevertheless, the polarization of PL from localized IXs has a significant linearly polarized component (Fig. 4.8) instead of cross-polarized emission. This can be the consequence of the anisotropic strain in our heterostructures that reduces the symmetry of a pristine moiré pattern. Another possible trapping is the strain or defect potential on a length scale larger than interlayer exciton Bohr

radius [97]. The coexistence of these two effects can also not be ruled out[98], which requires high spatial resolution technique to pinpoint their roles in the formation of localized IXs.

4.5 Multi-exciton complexes and configurations

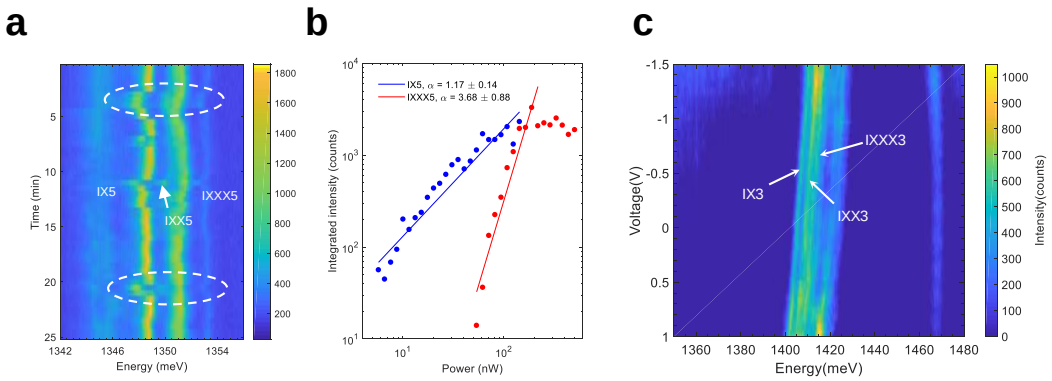

Figure 4.9: Multi-excitonic complex (triexciton) of localized interlayer excitons. **a.** Time-trace PL emission of interlayer exciton IX5, biexciton IXX5 and triexciton IXXX5. Dashed circles highlight the same spectral jittering patterns. Energy spacings between IX5 & IXX5 and IX5 & IXXX5 are ∼2.3 meV and ∼4.7 meV, respectively. **b.** Integrated intensity of emission peaks IX5 and IXXX5. We obtain $\alpha(IXXX5) \approx 3\alpha(IX5)$ from power-law fitting, indicating that IXXX5 is a triexciton. Error bars of power-law scaling coefficients arise from fitting. As the emission energy of IXX5 is very close to another uncorrelated strong peak (shown in a), we can not extract the power-dependent integrated intensity for IXX5. **c.** Electric field (E) tuning of exciton IX3, biexciton IXX3 and triexciton IXXX3 shows the same tuning rate as the bottom gate voltage changes from -1.5 V to +1 V.

We remark that biexciton is not the limit of exciton number that we can add into the same potential well. For another IX group, we observe three peaks with synchronized jittering. The highest energy peak has a power index 3 times of the lowest energy peak, probably a localized triexciton IXXX. Assuming the triexciton or multi-exciton can also be captured by the electrostatic model (Eq.(4.2)), we use the biexciton transition to estimate the confinement length l and then use this length to calculate the triexciton interexcitonic distance and transition energy. The calculated

lowest energy configuration is in Fig. 4.10a with a transition energy from IXXX to IXX $E_{32} = 3U'_{\mathrm{dd}} - U_{\mathrm{dd}}$. The calculated value without exchange interaction is the lower bound, since a localized triexciton inevitably has two excitons with the same valley index. $|X_+X_+X_-\rangle$ or $|X_-X_-X_+\rangle$ is the valley configuration with lowest exchange interaction energy. The triexciton transition energy $E_{32} = 3U'_{\mathrm{dd}} - U_{\mathrm{dd}} + U_{\mathrm{ex}}$ is calculated by plugging the interexcitonic distance $w = \sqrt{3}R_{eq,IXXX}$ into Eq.(4.3). This defines the high bound because further rearrangement by the exchange interaction makes IXXX asymmetric to lower the total energy and thus decreases E_{32}. We can further check the model with IX3-IXX3-IXXX3 group. Fig. 4.10b, c summarizes the consistency between the calculated and experimental value E_{32} for both groups, confirming the assignment of triexciton. More importantly, this analysis supports the existence of few-body exchange interaction, now that it is necessary to include to explain the energy spacing of multi-exciton. As expected for a triexciton, same Stark shift rate indicates that IXXX3 carries the same dipole moment as IX3, IXX3 (Fig. 4.9c). Finally, with increasing excitation power, systematic appearance of peaks to the higher energy of the parent red peak appear and dominate at the highest power, which is consistent with dipolar repulsion present in multi-excitonic states (see Appendix B).

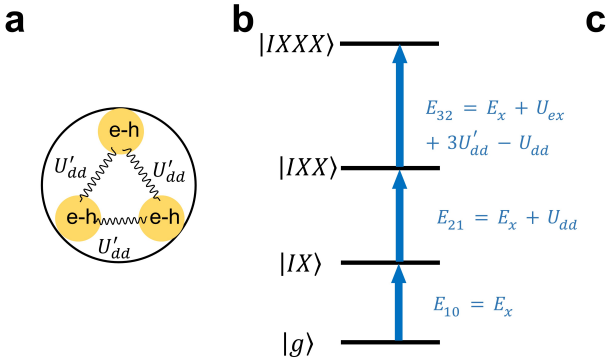

c

	Experiment		Calculation	
	$(E - E_x)$/meV	Splitting/meV	$(E - E_x)$/meV	
	E_{32}	$E_{32} - E_{21}$	E_{32} w/o U_{ex}	E_{32} w/ U_{ex}
IXXX5 → IXX5	4.7	2.4	3.1	5.5
IXXX3 → IXX3	6.2	2.7	4.7	8.7
	E_{21}	$E_{21} - E_{10}$		
IXX5 → IX5	2.3	2.3		
IXX3 → IX3	3.5	3.5		
	E_{10}			
	0			

Figure 4.10: Multiexcitonic complex configuration and energy diagram. **a.** Electrostatic configurations of triexciton. **b.** Energy diagram of triexciton. **c.** Comparison between experimental and calculated triexciton ($|IXXX\rangle$) to biexciton ($|IXX\rangle$) transition energy.

4.6 Conclusion and Outlook

In conclusion, we have observed repulsive dipole-dipole interactions between electric field-tuneable, localized interlayer excitons in $WSe_2/MoSe_2$ heterobilayer. The energy of localized biexciton, comprising two localized excitons with permanent out-of-plane dipole moment, is blue-shifted by ~ 2 meV due to dipole-dipole repulsion, corresponding to an inter-dipole distance of ~ 7 nm. At higher excitation power, multi-exciton complexes appear at systematically higher energies, consistent with the presence of few-body repulsive interactions. The magnetic field dependence of the emission polarization unveils spin-valley singlet biexciton state without exchange interaction, while multi-exciton complexes energy spacing provides the signature of few-body exchange interaction. Our finding paves the way to Wigner dipolar crystals with spin-valley spinor or Bose-Hubbard quantum simulator with on-site few-body interactions in vdW heterostructures.

Chapter 5

Many-body Interactions in 2D Materials

This chapter will discuss many-body interactions between IXs in a $WSe_2/MoSe_2$ heterobilayer. We show that the many-exciton exchange interaction induced valley Zeeman splitting up to 4 meV that corresponds to B $\approx$ 6 T. The relevant results are reported in Nature Nanotechnology[2].

5.1 Introduction

The many-body Coulomb interactions between delocalized IXs can be approximated by two terms: a valley-independent dipolar repulsion term and a valley-dependent exchange interaction term. Here we first focus on the interactions between two excitons and then use the mean-field approximation to calculate the density-dependent many-exciton interaction energies[41]. The general Coulomb interaction form of exciton-exciton interaction in a type-II TMD heterobilayer is

$$\hat{V}_{XX} = V_{e1,e2} + V_{h1,h2} - V_{e1,h2} - V_{e2,h1}$$
$$= V(\mathbf{r}_{e1} - \mathbf{r}_{e2}) + V(\mathbf{r}_{h1} - \mathbf{r}_{h2}) - V(\mathbf{r}_{e1} + \mathbf{d} - \mathbf{r}_{h2}) - V(\mathbf{r}_{e2} + \mathbf{d} - \mathbf{r}_{h1}),$$

where $\mathbf{r}_{e1}(\mathbf{r}_{e2})$ and $\mathbf{r}_{h1}$ $(\mathbf{r}_{h2})$ are the electron and hole xy-plane displacement vector for the first (second) exciton. $\mathbf{d} = d\hat{\mathbf{z}}$ is the interlayer separation (Fig. 5.1a). Here we consider electron-hole relative motion which is ignored in Eq.(4.1). $|X_{\tau_{e,1},\tau_{h,1},\mathbf{R}_1}(\mathbf{r}_{e1},\mathbf{r}_{h1})\rangle$ and $|X_{\tau_{e,2},\tau_{h,2},\mathbf{R}_2}(\mathbf{r}_{e2},\mathbf{r}_{h2})\rangle$ are the two exciton wave packets since many excitons at a high density have overlap and can not be considered as point particles.

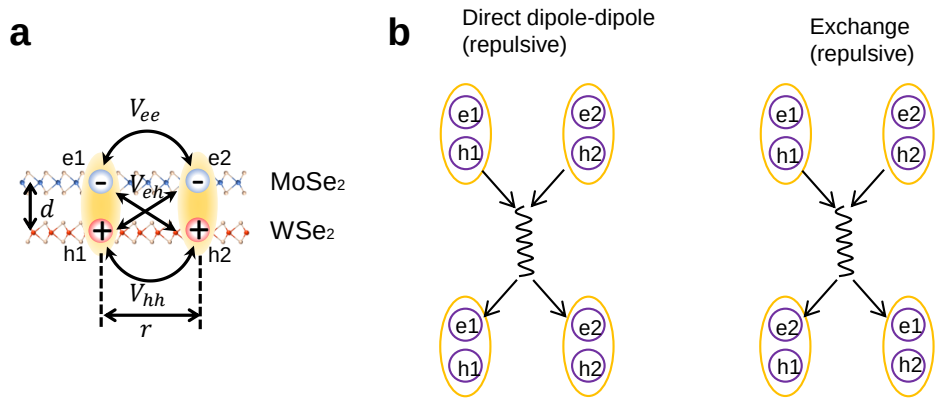

Figure 5.1: Exciton-exciton interactions. **a.** Schematic of Coulomb interactions between two excitons. **b.** Exchange process between two excitons.

The dipolar interaction is a direct exciton-exciton scattering process $(e1, h1) + (e2, h2) \rightarrow (e1, h1) + (e2, h2)$ (Fig. 5.1b, left). As long as the initial states are bright, regardless of spin-singlet or triplet states (discussed later), the final states are also bright, so this term is independent of valley indices of two excitons. The expectation value of direct Coulomb interactions in the two exciton wave packet basis is

$$
\begin{aligned}
&V_{\mathrm{dd}}(\mathbf{R}_1-\mathbf{R}_2)\\
&=\langle X_{\tau_{e2},\tau_{h2},\mathbf{R}_2}(\mathbf{r}_{e2},\mathbf{r}_{h2})|\langle X_{\tau_{e1},\tau_{h1},\mathbf{R}_1}(\mathbf{r}_{e1},\mathbf{r}_{h1})|\hat{V}_{XX}|X_{\tau_{e1},\tau_{h1},\mathbf{R}_1}(\mathbf{r}_{e1},\mathbf{r}_{h1})\rangle|X_{\tau_{e2},\tau_{h2},\mathbf{R}_2}(\mathbf{r}_{e2},\mathbf{r}_{h2})\rangle\\
&\approx\int|w(\frac{m_e\mathbf{r}_{e1}+m_h\mathbf{r}_{h1}}{m_e+m_h}-\mathbf{R}_1)w(\frac{m_e\mathbf{r}_{e2}+m_h\mathbf{r}_{h2}}{m_e+m_h}-\mathbf{R}_2)\Phi_I(\mathbf{r}_{e1}-\mathbf{r}_{h1})\Phi_I(\mathbf{r}_{e2}-\mathbf{r}_{h2})|^2\\
&\times(V(\mathbf{r}_{e1}-\mathbf{r}_{e2})+V(\mathbf{r}_{h1}-\mathbf{r}_{h2})-V(\mathbf{r}_{e1}+\mathbf{d}-\mathbf{r}_{h2})-V(\mathbf{r}_{e2}+\mathbf{d}-\mathbf{r}_{h1}))\\
&\times d\mathbf{r}_{e1}d\mathbf{r}_{e2}d\mathbf{r}_{h1}d\mathbf{r}_{h2},
\end{aligned}
$$

where $w(\mathbf{r}-\mathbf{R})$ denote the exciton center-of-mass wavefunction (or real-space wave packet) localized at $\mathbf{R}$, $\Phi_I(\mathbf{r}_e-\mathbf{r}_h)$ describe the electron-hole relative motion. Therefore, the first line inside the integral is the probability density of the two-exciton wavefunction and the second line is the form of Coulomb interactions. As the repulsion $V(\mathbf{r}_{e1}-\mathbf{r}_{e2})+V(\mathbf{r}_{h1}-\mathbf{r}_{h2})$ is always larger than the attraction $-V(\mathbf{r}_{e1}+\mathbf{d}-\mathbf{r}_{h2})-V(\mathbf{r}_{e2}+\mathbf{d}-\mathbf{r}_{h1}$, V_{dd} keeps positive, i.e., dipolar interactions are always repulsive in the vdW heterostructures.

The second term is exchange interactions, which requires the spin-valley indices to be the same for indistinguishable particles. Two excitons can be viewed as four constituent fermionic particles (Fig. 5.1a). The electron-hole overlap is negligible in type-II band alignment heterostructures, so electron-hole exchange is ignored here. As a consequence, we only need to consider electron-electron exchange and simultaneous hole-hole exchange process $(e1,h1)+(e2,h2)\rightarrow(e1,h2)+(e2,h1)$ (Fig. 5.1b, right). In other words, electrons are in the same valley ($\tau_{e1}=\tau_{e2}=\tau_e$) and holes are also in the same valley ($\tau_{h1}=\tau_{h2}=\tau_h$), though electron and hole can be in different valleys ($\tau_e=\tau_h$ or $\tau_e\neq\tau_h$). This picture is valid for the bright IX comprising electron and hole in opposite valleys (spin triplet) which has been observed in AB stacked $WSe_2/MoSe_2$[99, 100]. As shown in Fig. 5.2, spin-triplet and spin-singlet exciton both are bright and couple to opposite helicity of light. The energy splitting between

them is 24 meV, consistent with the $MoSe_2$ conduction band SOC splitting. The expectation value of the exchange interactions is calculated by switching two electron positions $\mathbf{r}_{e1}, \mathbf{r}_{e2}$ or two hole positions $\mathbf{r}_{h1}, \mathbf{r}_{h2}$ in the final states as below,

$$
\begin{aligned}
&V_{\text{ex}}(\mathbf{R}_1 - \mathbf{R}_2) \\
&= -\langle X_{\tau_{e2},\tau_{h1},\mathbf{R}_2}(\mathbf{r}_{e2},\mathbf{r}_{h1})|\langle X_{\tau_{e1},\tau_{h2},\mathbf{R}_1}(\mathbf{r}_{e1},\mathbf{r}_{h2})|\hat{V}_{XX}|X_{\tau_{e1},\tau_{h1},\mathbf{R}_1}(\mathbf{r}_{e1},\mathbf{r}_{h1})\rangle|X_{\tau_{e2},\tau_{h2},\mathbf{R}_2}(\mathbf{r}_{e2},\mathbf{r}_{h2})\rangle \\
&\approx \int w^*(\frac{m_e\mathbf{r}_{e2}+m_h\mathbf{r}_{h1}}{m_e+m_h}-\mathbf{R}_2)w^*(\frac{m_e\mathbf{r}_{e1}+m_h\mathbf{r}_{h2}}{m_e+m_h}-\mathbf{R}_1) \\
&\times w(\frac{m_e\mathbf{r}_{e1}+m_h\mathbf{r}_{h1}}{m_e+m_h}-\mathbf{R}_1)w(\frac{m_e\mathbf{r}_{e2}+m_h\mathbf{r}_{h2}}{m_e+m_h}-\mathbf{R}_2) \\
&\times \Phi_I^*(\mathbf{r}_{e2}-\mathbf{r}_{h1})\Phi_I^*(\mathbf{r}_{e1}-\mathbf{r}_{h2})\Phi_I(\mathbf{r}_{e1}-\mathbf{r}_{h1})\Phi_I(\mathbf{r}_{e2}-\mathbf{r}_{h2}) \\
&\times (V(\mathbf{r}_{e1}+\mathbf{d}-\mathbf{r}_{h2})+V(\mathbf{r}_{e2}+\mathbf{d}-\mathbf{r}_{h1})-V(\mathbf{r}_{e1}-\mathbf{r}_{e2})-V(\mathbf{r}_{h1}-\mathbf{r}_{h2})) \\
&\times d\mathbf{r}_{e1}d\mathbf{r}_{e2}d\mathbf{r}_{h1}d\mathbf{r}_{h2},
\end{aligned}
$$

The exchange interactions can occur only when the two exciton wavepackets have substantial overlap, or else w^* term will be exponentially small.

Next, we extend V_{dd} and V_{ex} to the mean-field potential seen by an IX at position $\mathbf{R}$ in K or K' valley,

$$
\begin{aligned}
\Delta E_{\pm}(\mathbf{R}) &= \int V_{\text{ex}}(\mathbf{R}-\mathbf{r})n_{\pm}(\mathbf{r})d\mathbf{r} + \int V_{\text{dd}}(\mathbf{R}-\mathbf{r})(n_+(\mathbf{r})+n_-(\mathbf{r}))d\mathbf{r} \\
&\approx n_{\pm}(\mathbf{R})\bar{V}_{\text{ex}} + (n_+(\mathbf{R})+n_-(\mathbf{R}))\bar{V}_{\text{dd}} \qquad (5.1)
\end{aligned}
$$

Where $n_{\pm}$ is IX density in K (K') valley, $n_{\pm}(\mathbf{R}) \approx \frac{\int V_{\text{ex}}(\mathbf{R}-\mathbf{r})n_{\pm}(\mathbf{r})d\mathbf{r}}{\int V_{\text{ex}}(\mathbf{R}-\mathbf{r})d\mathbf{r}} \approx \frac{\int V_{\text{dd}}(\mathbf{R}-\mathbf{r})n_{\pm}(\mathbf{r})d\mathbf{r}}{\int V_{\text{dd}}(\mathbf{R}-\mathbf{r})d\mathbf{r}}$ and $\bar{V}_{\text{dd/ex}} \equiv \int V_{\text{dd/ex}}(\mathbf{R}-\mathbf{r})d\mathbf{r}$ are constants if the mean-field approximation holds. In TMD vdW heterostructures,

$$V_{\text{dd}} = da_B E_b, \qquad (5.2)$$

$$V_{\text{dd}} = a_B^2 E_b. \qquad (5.3)$$

Both the dipolar and exchange interactions are repulsive, which cause energy blueshift and spatial diffusion of IXs. The dipolar interaction induced exciton diffusion[42, 72, 44] as well as energy blueshift[40] has been commonly reported in $WSe_2/MoSe_2$. Moreover, as circularly polarized light can selectively excite one valley, exchange interaction driven valley polarized exciton diffusion has also been observed in $WSe_2/MoSe_2$[41, 71].

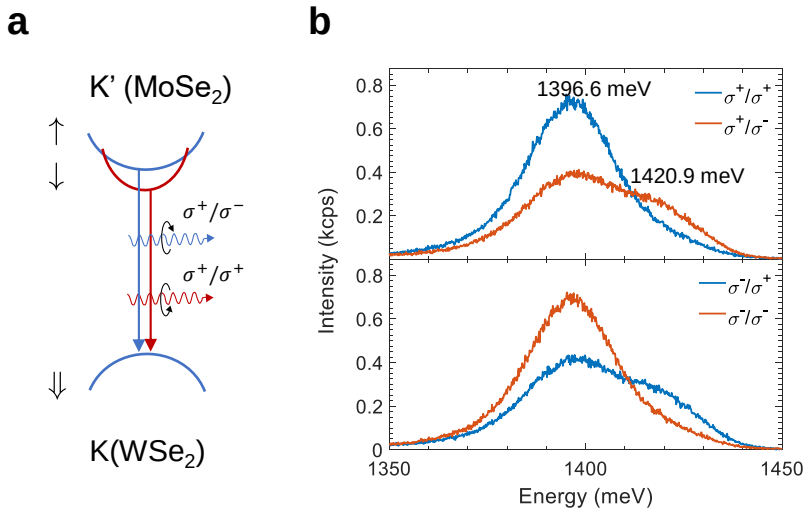

Figure 5.2: Spin triplet and singlet excitons in AB stacked $WSe_2/MoSe_2$ heterobilayer. **a.** Spin triplet (red) and spin singlet (blue) exciton couple to σ^+ and σ^- with interband transition from $MoSe_2$ K'-valley conduction band to WSe_2 K-valley valence band. The spin-triplet exciton is from low energy spin-flip transition while spin-singlet exciton is from low energy spin-conserved transition. **b.** PL emission spectra in AB stacked $WSe_2/MoSe_2$ at 65.3 K show both spin-triplet exciton (1396.6 meV, co-polarized) and spin-singlet exciton (1420.9 meV, cross-polarized) are bright excitons. The excitation energy is 1.72 eV and the power is 10 μW.

Here this chapter introduces a new scenario where the density imbalance between two valley IXs induces an energy splitting between the two species. It can be explained by Eq.(5.1) that the energy splitting between the two valley exciton species is,

$$\delta E(\mathbf{R}) = \Delta E_+(\mathbf{R}) - \Delta E_-(\mathbf{R}) \approx (n_+ - n_-)\bar{V}_{\mathrm{ex}}. \tag{5.4}$$

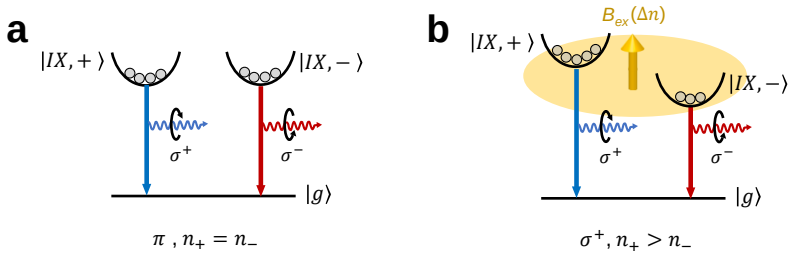

Figure 5.3: Schematic of IX valley energies under linear (π) (**a**) and circular (σ) excitation (**b**) in $WSe_2/MoSe_2$ heterostructure. The valley-IXs in the state $|IX,+\rangle$ ($|IX,-\rangle$) emit σ^+ (σ^-) light, and $|g\rangle$ is the exciton ground state. π excitation induces the same populations of these two kinds of excitons $n_\pm$ (left panel), while σ^+ excitation (right panel) induces an imbalance, $\delta n = n_+ - n_- > 0$. The imbalance under σ^+ excitation makes the exchange interaction between $|IX,+\rangle$ excitons larger when compared to that between $|IX,-\rangle$ excitons and gives rise to an energy splitting, corresponding to an effective exchange field $\mathrm{B_{ex}}(\Delta n)$, shown by the yellow shaded region and arrow.

Therefore, the calculated energy splitting is proportional to density imbalance $\delta n = (n_+ - n_-)$. As shown in Fig. 5.3a, if the two exciton species have the same density, for example, created by linear polarized light, time-reversal symmetry is unbroken and two valleys remain degenerate. For a finite density imbalance δn(Fig. 5.3b), created by circularly-polarized excitation (σ^+ as an example), the IXs in the valley coupled to the light ($|IX,+\rangle$) become majority while the other valley IX species ($|IX,-\rangle$) become the minority. As a result, the majority IXs have raised energy whereas the minority IXs have lowered energy, resulting in an exchange splitting. The prerequisite of such splitting is the existence of density imbalance of IXs, which are driven-dissipative systems. The overall effect is thus a many-exciton exchange interactions induced out-of-equilibrium magnetic field (B_{ex}).

5.2 Experimental details

We fabricate $WSe_2/MoSe_2$ and WSe_2/WS_2 heterobilayers to show the many-exciton exchange interaction induced splitting is a general behavior in vdW heterostructures with type-II band alignment. AB stacked $WSe_2/MoSe_2$ sample is fabricated by PDMS-based transfer method (Fig. 5.4a, left) whereas AB or AA stacked WSe_2/WS_2 sample is fabricated by PC-based pick-up technique (Fig. 5.4b, left). For the AB stacked $WSe_2/MoSe_2$, the lowest energy state IX is co-polarized spin-triplet state at a MX site, whereas the spin singlet state is cross-polarized at a higher energy. Similarly, AA stacked WSe_2/WS_2 has a lower energy spin-triplet IX state, contrary to AB stacked WSe_2/WS_2 which has a lower energy spin-singlet IX state. Both $WSe_2/MoSe_2$ and WSe_2/WS_2 are aligned along the 60° or 120° edges. The negligible lattice mismatch between WSe_2 and $MoSe_2$ reconstructs the lattice to form large domains ($\sim$ 100 nm) whereas the sizable lattice mismatch between WSe_2 and WS_2 generates periodic moiré potential trap for IXs. Therefore, IXs surfing on a $WSe_2/MoSe_2$ domain are basically free IXs without moiré potential[101], compared to IXs modulated by moiré potential in WSe_2/WS_2. Due to the spatial periodicity of excitonic moiré potential, we expect the IX wavefunction to be a delocalized Bloch state with the same periodicity as the moiré length. At a substantially high excitation power ($\sim \mu$W), only WSe_2/WS_2 exhibits a "biexciton state" of delocalized IXs (IXX) (Fig. 5.4b, right), which is an analog of the biexciton state of two localized IXs in Chapter.4. However, they are fundamentally different because IXXs are $|n > N\rangle$ state here instead of $|n = 2\rangle$ state in Chapter.4, where n is the exciton number and N is the number of available sites. The energy spacing between the IXX and IX can be effectively considered as the Mott gap opened by the on-site repulsion of IXs in the Hubbard model of IXs. Altogether, the interactions between free IXs in $WSe_2/MoSe_2$ domains or between moiré potential modulated delocalized IXs in WSe_2/WS_2 are many-body interactions in the vdW platform.

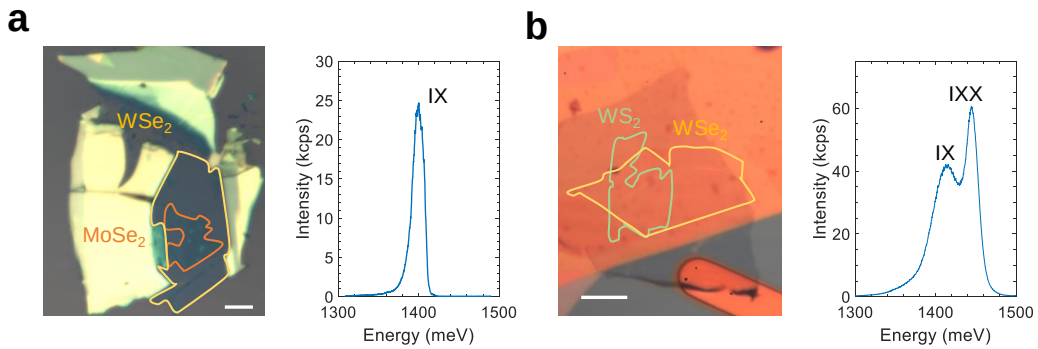

Figure 5.4: AB stacked $WSe_2/MoSe_2$(**a**) and WSe_2/WS_2(**b**) samples with corresponding PL spectrum at a high excitation power ($\sim \mu$W) and ~4K.

5.3 Observation of many-exciton exchange interactions induced splitting

Many-exciton exchange interactions are contact interactions, which require high exciton density. Furthermore, to observe exchange interactions induced splitting above the spectral resolution, we need to create a large imbalance δn. We hence conduct polarization-resolved photoluminescence excitation (PLE) spectroscopy with a circularly-polarized excitation in $WSe_2/MoSe_2$, which characterizes the density by the total intensity and the imbalance by the valley polarization or the degree of circular polarization (DCP) of PL. The total intensity (Fig. 5.5a) shows two prominent resonances at 1.64 eV and 1.72 eV, corresponding to monolayer $MoSe_2$ and WSe_2 intralayer exciton states. The DCP, which is defined as $(I_{\text{co}} - I_{\text{cross}})/(I_{\text{co}} + I_{\text{cross}})$, where I_{co} (I_{cross}) is the intensity of the co-polarized (cross-polarized) emission peak under circularly polarized excitation, strongly depends on the excitation energy. We use co-polarized to denote σ^+/σ^+ and σ^-/σ^-, because time reversal symmetry is conserved and σ^+/σ^+ or σ^-/σ^- produces the same results, which is the same reason to use cross-polarized to denote σ^+/σ^- and σ^-/σ^+. Fig. 5.5 shows that only excitation close to the WSe_2 resonance (1.72 eV) can create a large positive DCP, i.e.,

co-polarized excitons (counterpart of $|IX,+\rangle$) have much higher density than cross-polarized excitons (counterpart of $|IX,-\rangle$) leading to a large imbalance between two valleys. In contrast, $MoSe_2$ resonance (1.64 eV) produces negligible DCP, possibly implying substantial valley mixing during the relaxation from $MoSe_2$ exciton to IX (see Appendix.C). Thereafter, we use the circular excitation resonant with WSe_2 resonance to create pump-power varied imbalance δn. At low circular power (0.3 μW, Fig. 5.6a), helicity-resolved PL spectroscopy shows that the co-polarized emission has the same energy as the cross-polarized one within the spectral resolution. High circular power (10 μW, Fig. 5.6b) with a large δn, instead causes the co-polarized peak with high intensity blue-shifted ~4.5 meV more than the cross-polarized one with low intensity, consistent with our picture of exchange splitting. Such a splitting of ~4.5 meV is equivalent to B_{ex} ~6 Tesla based on the IX g-factor discussed below.

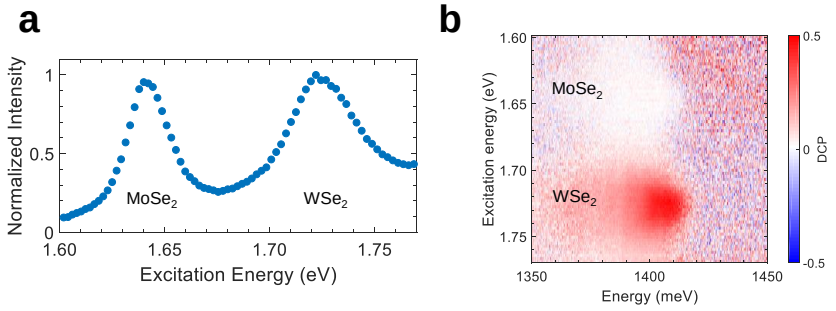

Figure 5.5: Polarization resolved photoluminescence excitation spectra. **a.** Photoluminescence excitation intensity plot, showing two prominent resonances 1.64 eV and 1.72 eV, corresponding to the monolayer $MoSe_2$ and WSe_2 intralayer exciton states. **b.** The excitation energy dependence of the degree of circular polarization (DCP) defined as $(I_{co} - I_{cross})/(I_{co} + I_{cross})$. I_{co} (I_{cross}) is the intensity of the co-polarized (cross-polarized) interlayer exciton (IX). An excitation at WSe_2 ($MoSe_2$) resonance ~1.72 eV (1.64 eV) creates a large (negligible) DCP, implying a large (negligible) imbalance between two valley-IX populations.

To further test our claim about B_{ex}, we perform systematic power dependence under circular and linear excitation at WSe_2 resonance. As the power rises, the integrated intensities increase and saturate (Fig. 5.6c) and peak energies are blue-

shifted (Fig. 5.6d). The integrated intensities are proportional to exciton steady-state density ($I \propto n/\tau$), if exciton lifetime τ is assumed to be the same for all powers. We can thus conclude that linear excitation results in negligible valley imbalance, and consequently no energy difference between two valley exciton peak energies. After switching to circular excitation, co- (cross-)polarized emission increases (decreases) its total intensity compared to the linear case, with raised (lowered) energies as expected. For circular excitation, we convert the difference in the integrated intensities (peak energies) into DCP (splitting) as shown in Fig. 5.6e. The DCP increases from 20% to 50% and saturates beyond 3 μW, with a similar trend for the splitting which increases from 0 to 4.5 meV. Theoretical relation between splitting and DCP is obtained using the Eq.(5.1) to Eq. (5.4),

$$\delta E = (\Delta E_+ + \Delta E_-) \times \mathrm{DCP} \times \frac{\bar{U}_{\mathrm{ex}}}{\bar{U}_{\mathrm{ex}} + 2\bar{U}_{\mathrm{dd}}} = (\Delta E_+ + \Delta E_-) \times \mathrm{DCP} \times \frac{a_B}{a_B + 2d}. \quad (5.5)$$

Based on the equation, the splitting δE follows the same trend as the DCP. Assuming a Bohr radius, $a_B = 2$ nm and interlayer distance $d = 0.7$ nm, the calculated energy splitting from the power dependence is shown in Fig. 5.7. The quantitative agreement between the calculated and experimental splitting at low power before the saturation power supports the fact that the splitting arises from the imbalance between $|IX, +\rangle$ and $|IX, -\rangle$. The deviation starting from the saturation power may come from a phase-space filling blue shift [70] beyond our model, which is spin-valley independent so $(\Delta E_+ + \Delta E_-)$ increases but δE keeps the same. Taking a binding energy, E_{b} = 200 meV, we estimate that a splitting of $\sim$ 4 meV arises from a $\delta n \sim 5 \times 10^{11}$ cm^{-2} and total density $(n_+ + n_-) \sim 1.16 \times 10^{12}$ cm^{-2}. On the other hand, we can estimate the density $n = \frac{10\%}{A} \times \frac{P}{h\nu} \times \tau \sim 10^{12}$ cm^{-2}, using an incident power $P \sim \mu$W, an absorption of $\sim$ 10% at WSe_2 resonance ($h\nu$ = 1.72 eV), a laser spot

size of 1 μm^2 and IX lifetime $\tau \sim$ ns. This consistency confirms our exciton density estimation, which is used to extract the strength of exciton-exciton interaction to be $\sim$0.8 μeV μm^2 ($\delta E/\delta n$), which is about an order of magnitude larger than that of monolayer TMDs[102, 103, 104, 105], but comparable to that of a heterobilayer TMD[72]. The saturation of the total intensity at large power is possibly a result of exciton-exciton annihilation (EEA). The estimated low EEA rate is in agreement with the negligible optical doping, and thus exciton-polaron plays a negligible role in our system (see Appendix C). Apart from the linear excitation, circular excitation resonant with $MoSe_2$ resonance also generates negligible imbalance, inducing zero exchange splitting as shown in Fig. 5.8. This indicates that exchange splitting is determined by exciton density imbalance, rather than circular excitation.

We remark that exchange field induced splitting is reproducible for another IX in $WSe_2/MoSe_2$ with larger DCP $\sim$0.6 and therefore larger splitting of $\sim$8 meV (Fig. 5.9). Since the exchange splitting model is not specific for $WSe_2/MoSe_2$, we also observed similar phenomena in IXX emission from AB stacked WSe_2/WS_2 (Fig. 5.10a, b) and IX emission from AA stacked WSe_2/WS_2 (Fig. 5.10c). For an AB stacked WSe_2/WS_2, IX emission is almost fully cross-polarized, implying that only one valley exciton species exist, labeled as $|IX,-\rangle$. Then the cross-polarized emission of IXX is from $|IX,-\rangle|IX,-\rangle$ states and the co-polarized emission of IXX is from $|IX,+\rangle|IX,-\rangle$ states. The exchange interactions within $|IX,-\rangle|IX,-\rangle$ triplet states lift their energy compared to $|IX,+\rangle|IX,-\rangle$ singlet states, an analog of the scheme in Fig. 4.7d for delocalized IXs.

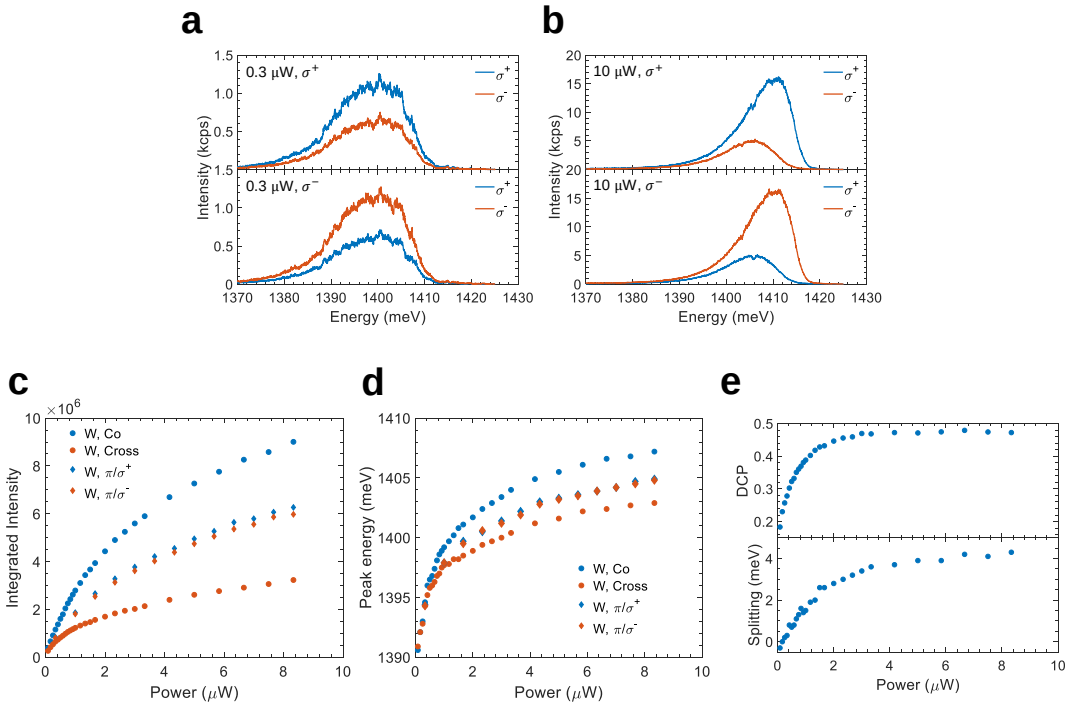

Figure 5.6: Power dependent integrated intensity, peak energy, DCP and splitting at circular and linear excitation. **a, b.** Helicity-resolved photoluminescence (PL) spectra of IXs under low (high) excitation power of 0.3 μW (10 μW) shown in **a** (**b**). The sample is excited with σ^+ (σ^-) light in the top (bottom) panel. The σ^+ (σ^-) component of the PL is shown in blue (red). At low power, (**a**), no apparent splitting between the σ^+ and σ^- components is observed, while an obvious splitting is observed at high power (**b**). The co-polarized peaks have higher intensity than the cross-polarized peaks. **c, d.** Integrated intensity (**c**) and peak energy (**d**) at the linear excitation (π/σ^+, π/σ^-) and circular excitation (co, cross) denoted by diamonds (circles). Linearly polarized excitation induces no imbalance and no energy splitting between σ^+ and σ^--polarized IXs. The peak intensity and energy at linear excitation lie between co- and cross-polarized cases. **e.** Power dependence of DCP (upper panel) and splitting (bottom) under circular excitation. The splitting energy is $E_{\text{co}} - E_{\text{cross}}$, where E_{co} (E_{cross}) is the energy of the co-polarized (cross-polarized) peak and follows the same trend as DCP, that is, increases with power and then saturates at high powers. The excitation energy is 1.72 eV in all panels. Panel **a, b** and Panel **c, d, e** are two sets of data collected in different setups and different thermal cycles.

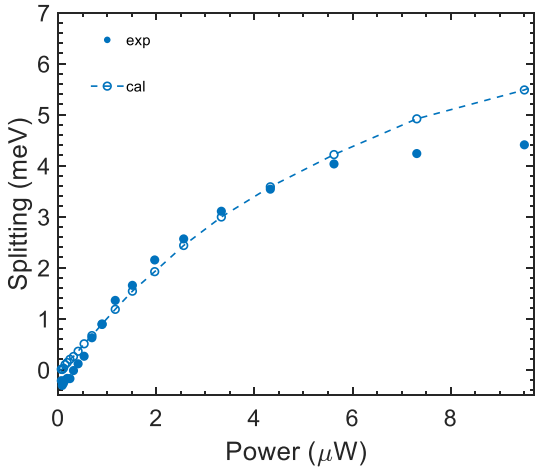

Figure 5.7: Calculated power dependence of the energy splitting. The calculated splitting (dash-circle lines) matches the experimental splitting (solid circles).

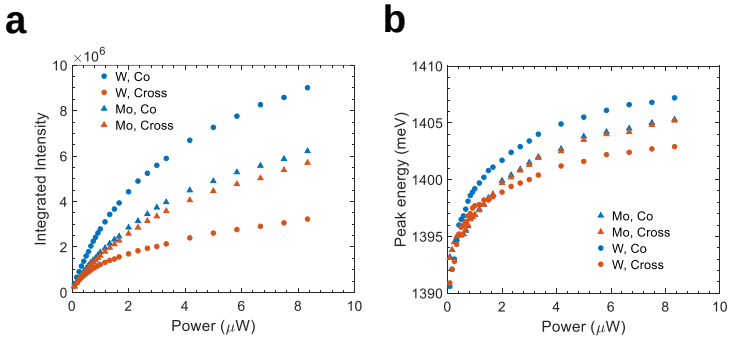

Figure 5.8: Power dependence of the integrated intensities (**a**) and peak energies (**b**) at the WSe_2 ($MoSe_2$) resonance denoted by circles (triangles). The co-polarized (cross-polarized) peak is shown in blue (red). At the WSe_2 resonance, the imbalance between intensities of co- and cross-polarized peaks and their peak energy splitting increase with power. No imbalance and energy splitting are observed for $MoSe_2$ resonance. The error bar in **b** is from the uncertainty of deciding the peak position.

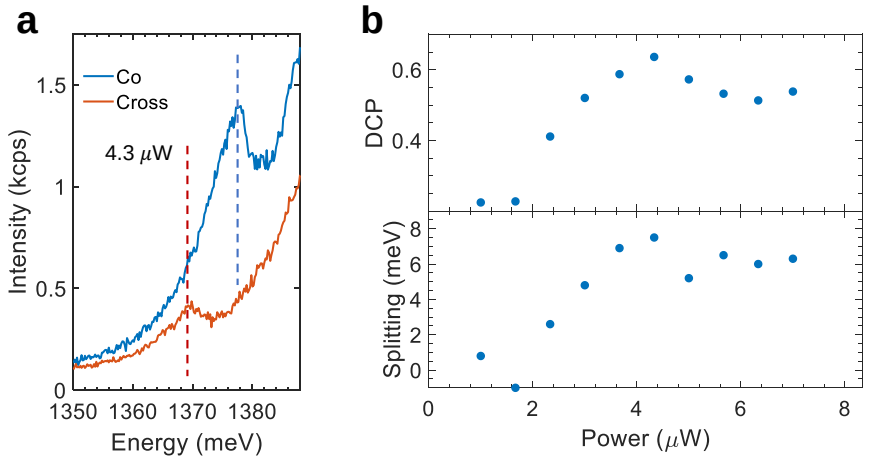

Figure 5.9: Power dependence of the degree of circular polarization and splitting for another interlayer exciton. **a.** Helicity-resolved PL spectra at 4.3 μW. The co-polarized excitons have higher intensity and higher energy than the cross-polarized excitons. **b.** The power-dependent DCP (upper panel) and splitting (bottom panel). Both the DCP and splitting increase with larger power and saturate about 4.3 μW. Excitation laser is circularly-polarized, with energy $h\nu = 1.72$ eV.

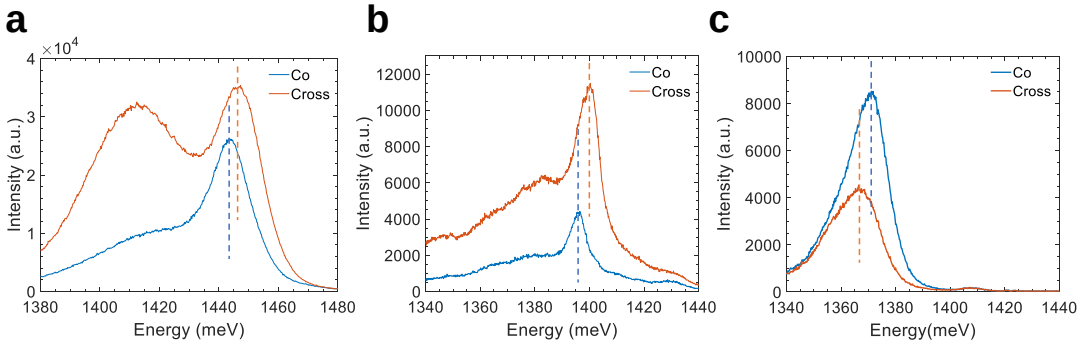

Figure 5.10: Exchange splitting in WSe_2/WS_2 heterobilayer. **a, b.** Exchange splitting for the double occupancy state in AB stacked WSe_2/WS_2 sample 1 (**a**) and 2 (**b**). **c.** Exchange splitting for the single occupancy state in an AA stacked WSe_2/WS_2 sample. Blue (orange) dashed line indicates the center energy of co- (cross-) polarized PL emission. For all the cases, the valley IXs with high intensity, i.e., high density, have higher energy.

5.4 Interplay between exchange field and external magnetic field

Having established the exchange field $B_{\mathbf{ex}}$, we perform magneto-PL spectroscopy to investigate the analogy between $B_{\mathbf{ex}}$ and an external B. At $B = 0$, σ^+ excitation induces the majority IX species $|IX, +\rangle$ has a higher energy than the minority IX species $|IX, -\rangle$ (Fig. 5.11a). When an external B is applied perpendicular to the sample ($B \neq 0$), it shifts the energies of the two valleys in opposite directions by the valley Zeeman effect [106, 100, 43]. The shift direction depends on the out-of-plane B direction, and thus one expects that an external B can cancel B_{ex} in one direction and enhance it in the other. When the B_{ex} is cancelled, the σ^+ and σ^- components have the same energy (Fig. 5.11b). To test this picture, we first characterize the Landé g-factor of our $WSe_2/MoSe_2$ by measuring the valley Zeeman effect under linearly polarized excitation. As shown in Fig. 5.11c, we measure a g-factor of -13.41, suggesting that the sample is AB stacked[106]. The fact that we observe only one co-polarized peak with a g-factor of -13.41 is consistent with optically bright spin triplet state at MX site, whereas the cross-polarized spin singlet state at the same site is a higher energy state, which is suppressed at low temperature (4K) and brightened at higher temperature (65.3 K, Fig. 5.2b)[50, 100]. Using g-factor of -13.41, we can estimate 4.5 meV splitting is corresponding B_{ex} *sim* 6 T.

Next, we measure the B-dependence of splitting of the peak energies ($E_{\pm}$) of the $\sigma^{\pm}$ components under circular excitation. The excitation power is chosen to be ~ 2 μW so as to avoid any effects of power saturation. From Fig. 5.11d we find that the effect of anomalous splitting at zero field is completely canceled by the external B $\sim$-6 T for σ^- excitation and the energies of $|IX, +\rangle$ and $|IX, -\rangle$ are flipped beyond -6 T. In other words, the $B_{\mathrm{ex}} \sim +6$ T, is consistent with the previous estimation. Remarkably, the ability to optically undo the effect of B up to 6 T with continuous-

wave power of $\sim\mu$W is attractive for spin-valley control, which has not been previously observed. Another evidence for the equivalence between B_{ex} and external B is shown

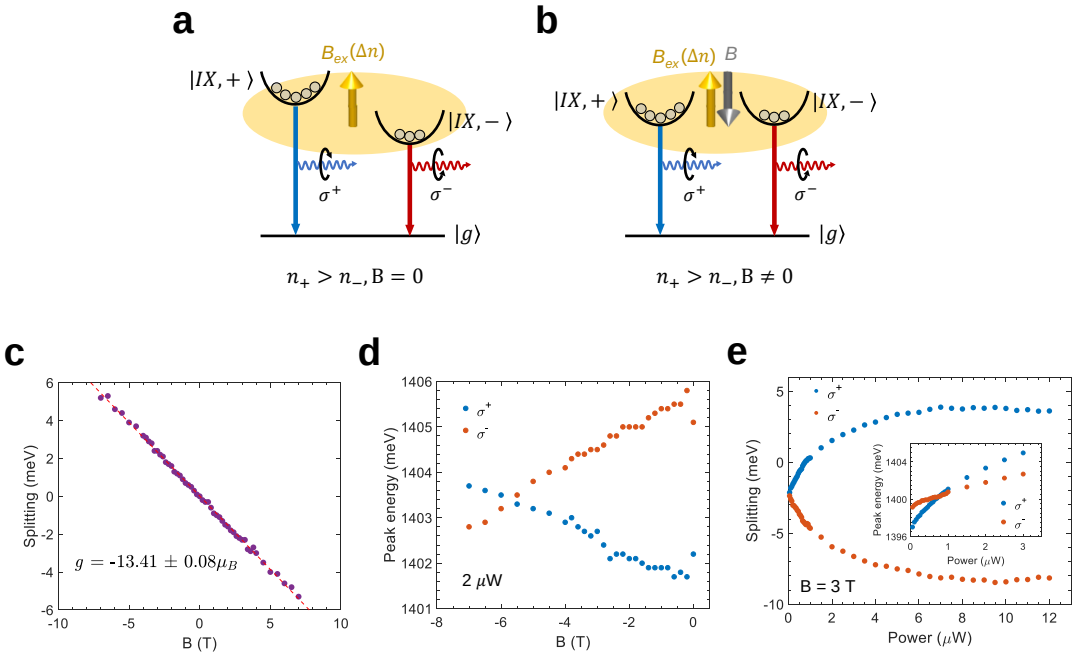

Figure 5.11: Equivalence between the exchange field and the external magnetic field. **a, b.** Schematic of valley-interlayer exciton (IX) energy levels at magnetic field (B) = 0 and $B \neq 0$ under σ^+ excitation. At $B = 0$ (**a**), the circular excitation creates an exchange field, B_{ex}, (yellow arrow) that lifts the degeneracy of the two valley-IXs. By applying an external B (**b**, gray arrow), B_{ex} can be cancelled. **c.** Magnetic field dependence of the Zeeman splitting energy ($E_{\sigma^+} - E_{\sigma^-}$) under linear excitation. The g factor of -13.41 is consistent with 60° stacking angle. The pink dashed line is the linear fitting of the data. The error bar is from the uncertainty of the linear fitting of the splitting. **d.** B dependence of the peak energies under σ^- excitation. The energy of the σ^+ (blue circles) and σ^- components (red circles) are flipped by the external B field of -6 T. Thus, σ^- excitation is equivalent to a positive B_{ex}. **e.** Power dependence of the splitting energies under circular excitation at $B = 3$ T. At low (high) powers, the splitting is roughly equal to (larger than) the Zeeman splitting under the linear excitation. The inset shows the peak energy shift with the excitation power of σ^+ excitation, showing a flip ~ 0.8 μW, which indicates that σ^+ excitation is equivalent to a negative B. The excitation energy is 1.72 eV in all the panels.

in Fig. 5.11e, where we fix the external B at +3 T and vary the circular excitation power. At very low powers, B_{ex} is negligible and the splitting of -2.3 meV is the same

as the Zeeman splitting under linear excitation at +3 T in Fig. 5.11c. When the power increases, the σ^+ excitation induced exchange field cancels the external B at $\sim$0.8 μW. The inset of Fig. 5.11e clearly shows that a flip in the energies of the two valleys at a positive B is caused by σ^+ excitation. Thus, we can conclude that σ^+ (σ^-) excitation results in B_{ex} acting as negative (positive) external B and that the B_{ex} and the external B are analogous as far as the splitting is concerned.

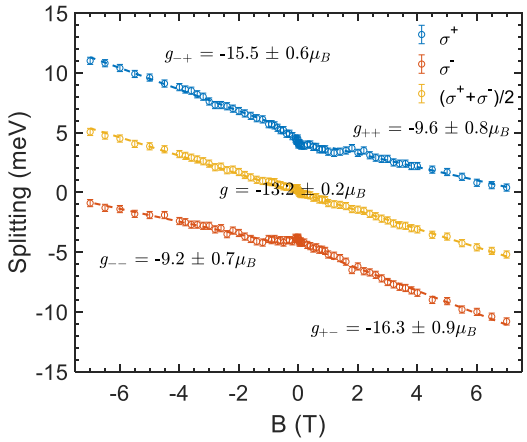

Figure 5.12: g-factor of different excitation polarization at an excitation power of 7.6 μW. g-factor of the σ^+ (σ^-) excitation under negative (positive) B is - 15.5 (-16.3), which is larger than the linear case. In contrast, σ^- (σ^+) excitation under negative (positive) B has a smaller g-factor of -9.2 (-9.6). The blue, red and yellow dashed lines are linear fits for σ^+, σ^- excitations, and the average of the two, excluding the dip near 0 T. The red dashed dot lines are parallel to the fitting curve of the averaged data which has a g-factor close to the linear case. The excitation energy is 1.72 eV in all the panels.

Different from the behavior below the saturation, the interplay between the B_{ex} and the external B above the saturation acts in a nonlinear fashion. Figure 5.12 shows that B-dependence of total splitting at 7.6 μW gives a larger g-factor for σ^+ excitation under negative B (g_{-+} = -15.5) and σ^- excitation under positive B (g_{+-} = -16.3). On the contrary, the g factors of σ^- excitation under negative B (g_{--} = -9.2) and σ^+ excitation under positive B (g_{++} = -9.6) are smaller. Such a helicity control of the

bare g-factor could be explained by the suppressed valley-mixing processes during the relaxation of intralayer exciton to IX with increasing B and at higher circular powers. With a lower depolarization rate at a higher B, the imbalance increases, so does B_{ex}, and thus induces a larger enhancement (g_{+-} or g_{-+}) or cancellation ((g_{--} or g_{++})) of the splitting.

5.5 Conclusion and Outlook

In conclusion, we have demonstrated that many-exciton exchange interactions in type-II TMD heterobilayer can generate exchange field up to several Tesla under steady-state condition. Such a large effective magnetic field, essential for the control of the valley-pseudospin, can be dynamically tuned on a timescale of IX exciton lifetime (nanoseconds). Strong many-body Coulomb interactions between long-lived IXs are responsible for the efficient generation of exchange field with very low continuous-wave incident powers ($\sim \mu$W) compared to previous schemes. In light of this, our results on many-body physics of excitons, focusing on the valley-pseudospin, make a strong case for investigating quantum magnetism in this rich materials platform. As the sign of the exchange interaction can be flipped by varying the interlayer space, we can achieve many-exciton ground states with aligned valley-pseudospin (ferromagnetic ordering), instead of antiferromagnetic ordering reported in this work.

Chapter 6

Quantum Sensing of Correlated Electrons in vdW Heterostructures

In this chapter, I will show localized interlayer excitons as a noninvasive charge sensor to detect the charge distributions in vdW heterostructures with a high spatial resolution ($\sim$ 10 nm). The localized interlayer exciton with sharp, non-jittering PL emission can probe the small local electric field from surrounding correlated electrons by its dipole energy shift. The results discussed in this chapter are reported in an arXiv preprint[3].

6.1 Introduction

6.1.1 Previous detection tools for correlated electronic states

The correlated electronic states with charge and spin ordering have been observed in moiré materials, with predictions for several other undiscovered exotic phases [107]. The experimental detection of such phases in semiconducting TMD moiré heterostructures is an ongoing endeavor that presents challenges but also unique opportunities. For example, while electronic transport measurements are plagued by high electrical

contact resistance [108, 109], inherently strong light-matter interactions have been successfully exploited in non-contact optical spectroscopic techniques to uncover correlated insulating states at several fractional fillings of the moiré lattice, including 2s exciton sensor[35, 110] and optically-detect resistance and capacitance (ODRC)[59]. The optical sensing using 2s exciton sensor is to assemble monolayer layer WSe_2[35] or $MoSe_2$[110] on top of the moiré sample with a hBN spacer (∼1nm) thinner than the Bohr radius (Fig. 6.1a, top). The dielectric screening for 2s exciton is modified by the charge compressibility in the sample, which induces 2s exciton bandgap renormalization and binding energy modulation. When carriers are filled to certain fractions, they form a general Wigner crystal, which is insulating and causes an energy blueshift of 2s exciton resonance (Fig. 6.1a, bottom). Figure 6.1b shows that ODRC is to detect the charge compressibility in the sample region (Region 1) by the optical response in another connected region (Region 2). Whenever a general Wigner crystal is formed, the carriers in Region 2 can not flow into Region 1, so the intralayer exciton reflectance signal change is zero (Fig. 6.1b, bottom). In addition to optical techniques with a spatial resolution of spot size (∼ 1 μm), traditional scanning probe techniques such as microwave impedance microscopy (MIM)[111] or single electron transistor (SET)[112] can detect correlated electronic states with a ∼100 nm spatial resolution. MIM measures the imaginary part of impedance to determine whether the sample is conductive or insulating (Fig. 6.1c), whereas SET measures the ac modulated local electrostatic potential to derive the local charge compressibility. The above detection tools probe over tens to several thousand moiré unit cells and lack the spatial resolution needed to study local fluctuations of charge and spin order. Besides higher resolution scanning probe STM/S for local sensing[38], vdW materials offer an all-2D approach wherein localized charge and spin sensors in one moiré lattice spatially sample correlated electronic states in a different moiré lattice of the same heterostructure, from which a global picture can be reconstructed.

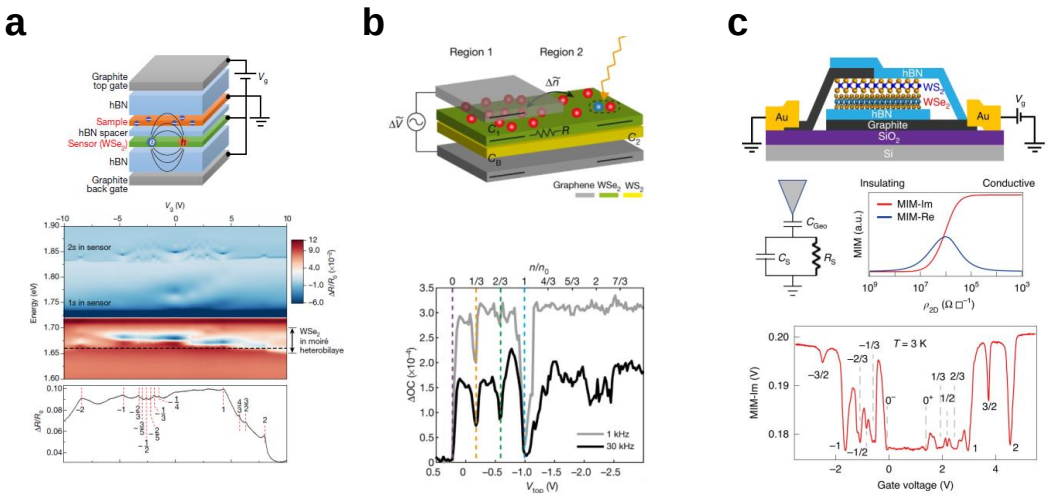

Figure 6.1: Examples of detection techniques for correlated insulating states at fractional fillings. **a.** 2s exciton sensor [Reprinted from [35]]. **b.** Optically-detect resistance and capacitance [Reprinted from [59]]. **c.** Microwave impedence microscopy [Reprinted from [111]]. All top panels are the sample structure and bottom panels are the carrier filling dependent spectra.

6.1.2 Previous study on strongly correlated interlayer excitons and electrons

To optically detect the charge-ordered states using the PL spectra, we exploit interactions between IXs and correlated electrons. A well-established system for correlated electrons is WSe_2/WS_2 heterobilayers[113, 114]. In a WSe_2/WS_2 heterobilayer, integer and fractional fillings are identified by the moiré intralayer excitons doping behavior. At integer or fractional fillings, charges become incompressible and increase the optical contrast (Fig. 6.2c). The filling dependent PL emission of delocalized IXs (Fig. 6.2a) is then conducted in the same sample with the same gate configurations. It shows sudden energy shifts at all integer fillings or certain fractional fillings, arising from interactions between IXs and correlated electrons. Their corresponding PL DCP is greatly enhanced after electron doping $\nu = 1$ and hole doping $\nu = -1$. We remark that the non-monotonic behaviors of energy shifts, DCP and reflectance contrast are

highly interconnected with respect to fillings. For example, $\nu = \pm 1$ exhibit a large PL energy blue-shifts (30-40 meV), PL DCP and reflectance contrast enhancement, which can help us identify fillings. A more recent study on strongly correlated IXs and electrons is light-induced ferromagnetism observed in WSe_2/WS_2, where optically injected untrapped IXs mediate the magnetic interactions between holes trapped in moiré potentials[115].

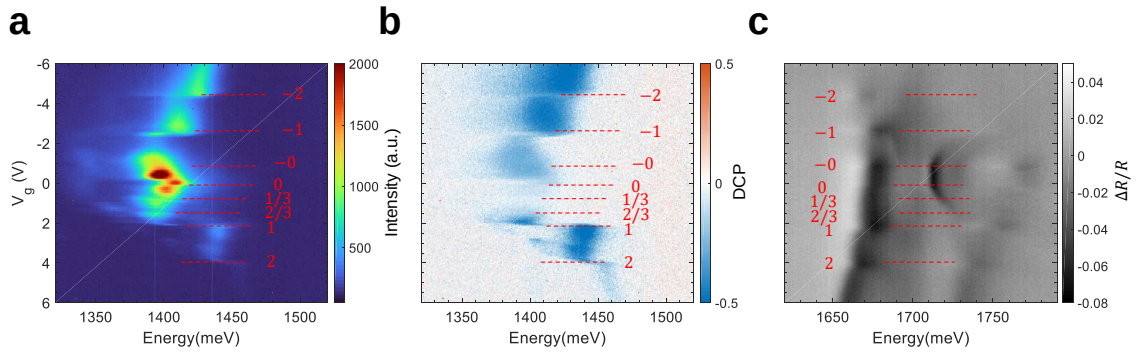

Figure 6.2: Correlated excitons and electrons in a WSe_2/WS_2 heterobilayer. The doped carrier density dependent PL intensity (**a**), DCP (**b**) and reflectance contrast (**c**) reveal integer and fractional fillings. Negative fillings denote hole doping and position fillings denote electron doping.

6.1.3 Previous study on doping dependence of localized interlayer excitons

The untrapped IXs provide the information within 1 μm of the laser spot size. To have a higher spatial resolution, localized IXs in $WSe_2/MoSe_2$ heterobilayers are good candidates with ~10 nm resolution. The doping dependence of delocalized IXs in Fig. 6.3a, b show a 6-7 meV redshift for both electron and hole doping in two $WSe_2/MoSe_2$ samples, where the interlayer trions are formed. After we reduce the power from μW to nW, we observe abundant sharp peaks, a typical feature of localized IXs (Fig. 6.3c). If localized IXs are moiré excitons, the sharp peaks in the electron/hole doping

region, red-shifted by 6-7 meV from the neutral region, are moiré trions[116][117][118].

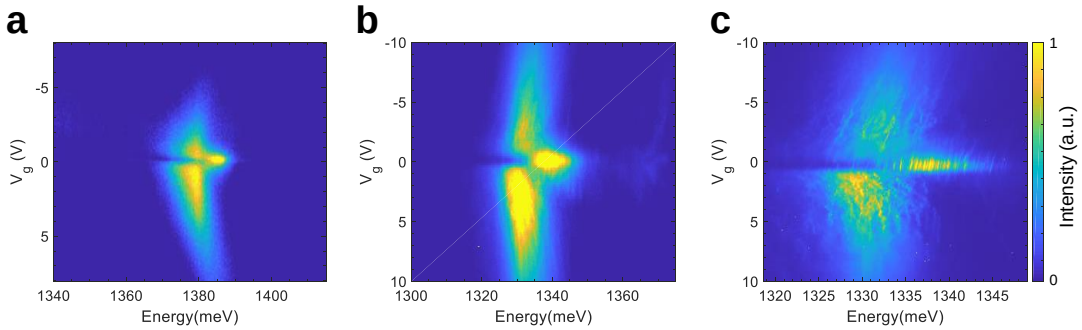

Figure 6.3: Moiré trions. **a, b.** The doping dependence of the IX PL emission energy in $WSe_2/MoSe_2$ Sample 1 (**a**) and Sample 2 (**b**). There is a 6-7 meV redshift for both electron and hole doping, where the interlayer trions are formed. **c.** The low power and high-resolution version of the data in (**b**), which shows many sharp spectral peaks, a typical feature of localized IXs.

6.2 Experimental details

Taking a first step towards this all-2D high spatial resolution approach, we fabricate a dual-moiré $WSe_2/MoSe_2/WSe_2$ heterotrilayer which features different moiré superlattices for electrons and dipolar interlayer excitons, owing to different twist angles of the top and bottom heterobilayers [119]. The dual-gated transition metal dichalcogenide heterotrilayer devices were fabricated via layer-by-layer dry transfer method using a polycarbonate (PC) stamp [89]. The WSe_2 and $MoSe_2$ monolayers, few-layer graphene and thick hBN were first mechanically exfoliated from bulk crystals on 300 nm SiO_2/Si substrates. The thickness of flakes was then determined by their optical contrast, from which we estimated the hBN thickness to be around 200 nm, consistent with atomic force microscopy measurements. The reason we selected thick hBN was to reduce the effect of charge fluctuations near the sample. To produce small twist angles between the top WSe_2 and the middle $MoSe_2$ layers, as well as between the bottom WSe_2 and middle $MoSe_2$, we used the tear-and-stack method [120] to pick up

half of a WSe_2 flake, align with the $MoSe_2$ layer within 1° uncertainty and pick up the other half of the WSe_2 flake with a rotation angle of 3°. To tune the charge density ($V_{bg} = V_{tg} = V_g$) or apply an electric field to the sample ($V_{bg} = -V_{tg} = V_E$), voltages are applied to the graphene top gate and graphene bottom gate through Keithley 2400 source meters while the graphene contact is grounded. The top and bottom gates are nearly symmetric with 180-200 nm hBN gate dielectrics, so negligible electric field was measured with symmetric gating voltages.

Figure 6.4a shows the device consisting of hBN encapsulated $WSe_2/MoSe_2/WSe_2$ heterotrilayer with dual graphite gates which allow for independent control of electron density and out-of-plane displacement field (Fig. 6.4b). The type-II band alignment in $MoSe_2/WSe_2$ heterobilayer results in the lowest energy state for electrons (holes) in the $MoSe_2$ (WSe_2) layer such that the top (bottom) IX formed in the top (bottom) heterobilayer has a dipole moment pointing up (down), which responds to an out-of-plane electric field (E). In the low temperature photoluminescence (PL) spectra (Fig. 6.4c), we identify the two species of IX with opposite dipoles by their opposite Stark shifts under E. As bottom IXs are abundant in our sample, in the following we focus primarily on them.

6.3 Sharp and non-jittering localized dipolar excitons as electric and magnetic field sensors

To characterize localized IXs in the trilayer, we conduct low-temperature PL spectra at low power to show several localized emitters in the IX energy range, which are non-jittering with an extremely narrow, instrument-limited linewidth of $\sim$ 26 μeV (Fig. 6.5a, b). Such a sharp linewidth enables the detection of a small electric field ($\sim$ 40 μV/nm). In addition to sensing electric fields through changes in their energy, IX can sense magnetic fields (B) as small as 10 mT. As shown in Fig. 6.5d, DCP

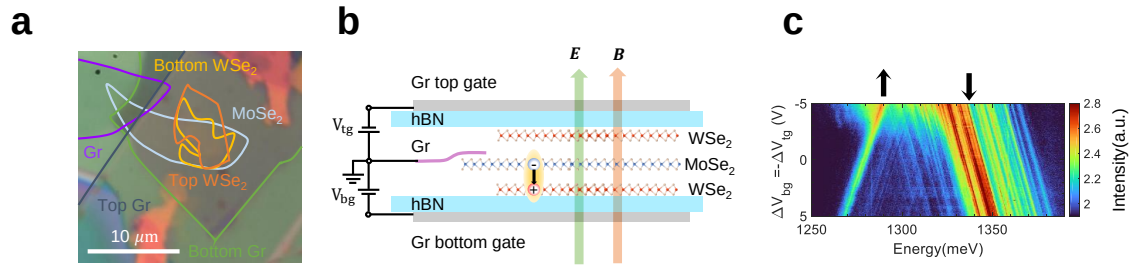

Figure 6.4: Dual-gate WSe2/$MoSe_2$/WSe_2 heterotrilayer device. **a.** Optical microscope image and **b.** Side-view illustration of the trilayer heterostructure. The bottom WSe_2 layer is rotated by 3° relative to the top WSe_2 layer. **c.** Gate dependence of dipolar IX emission. The electric field from the asymmetric gating induces blueshift (redshift) of the IXs in the bottom (top) heterobilayer denoted by downward (upward) from -5 V to 5 V. The black arrows represent the dipole directions of the corresponding excitons. The intensity colorbar is logarithmic.

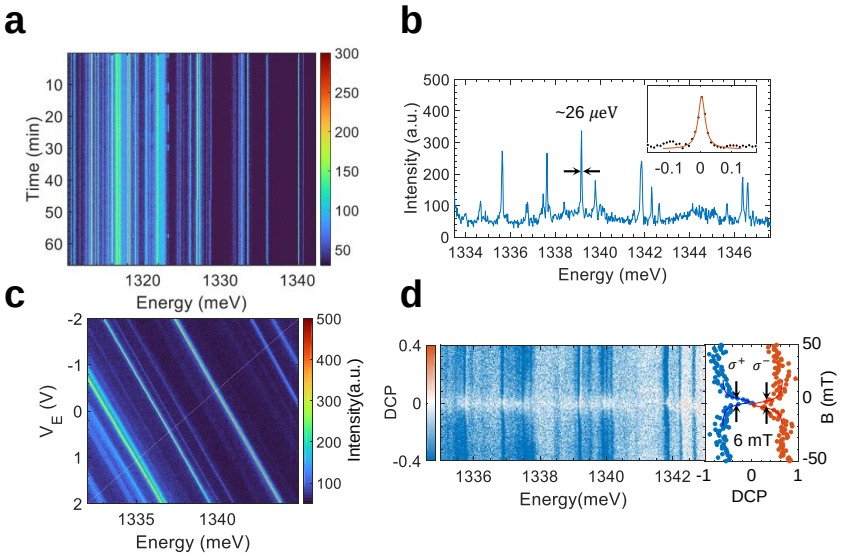

Figure 6.5: Sharp, non-jittering localized dipolar excitons in WSe_2/$MoSe_2$/WSe_2 heterostructures as electric and magnetic field sensors. **a.** The time-trace photoluminescence (PL) emission of localized interlayer excitons (IXs), showing sharp and stable peaks. The energies of the excitons are consistent with IX energies. **b.** The PL spectra of IXs show instrument resolution-limited linewidths as narrow as ~ 26 μeV. **c.** Electric field dependent sharp localized IX emission energy shift. **d.** Polarization-resolved magneto-PL of IXs with σ^+ excitation. The degree of circular polarization (DCP) increases with both positive and negative magnetic fields B. The Lorentzian fitting of the DCP versus B gives a 6 mT width.

under circularly polarized excitation rapidly increases from zero to unity with B. This effect can be used to sense the local spin or valley configuration of electrons and enable probing of quantum magnetism.

6.4 Probing charge order reconfiguration with tunable carrier density

As localized IXs are sensitive electric field sensors, we explore their application to sense local electric field from neighboring ordered electrons in Fig. 6.6. The effect of our trilayer with different top and bottom twist angles is shown in Fig. 6.6a, which plots the calculated moiré potentials for an IX in the bottom heterobilayer and an electron in the $MoSe_2$ layer for twist angles of $1°/4°$, representative of our sample. While an IX experiences only the bottom moiré potential, an electron sees the interference of the top and bottom moiré potentials resulting in a multi-orbital (multi-minima) electron moiré potential [119]. Therefore, trapped IXs, as localized dipoles, are sitting at different potential minima from the electrons, which sample the correlated electronic state efficiently. Figure 6.6b shows a cartoon depiction of our local charge sensing scheme – strong electron-electron interactions (U_{e-e}) result in correlated, charge-ordered states at fractional fillings of the electronic moiré lattice as carrier density is changed, which are then sensed through energy shifts of localized IX arising from electron-dipole interactions (U_{e-d}). U_{e-d} consists of the repulsion between the electrons and attraction between the electron and hole as in Fig. 6.6c. The energy shift of a dipole by one electron at r_{eff} is given by

$$U_{e-d} = \frac{1}{4\pi\epsilon_r\epsilon_0}\left(\frac{1}{r_{\text{eff}}} - \frac{1}{\sqrt{r_{\text{eff}}^2 + d^2}}\right), \tag{6.1}$$

which is a blueshift. Next, we consider energy shifts of localized IXs with respect to the charge-ordered states. As the carrier density (n_e) is increased, electrons in charge-ordered states reconfigure and induce a red (Fig. 6.6d) or blue shift (Fig. 6.6e) of IX energy. The blue shifts can be explained by adding electrons without redistribution of already-present electrons or by pushing already-present electrons closer to the exciton by redistribution. In contrast, the redshifts with increasing electron density can only be explained by reducing the number of electrons close to the exciton by redistribution of electrons.

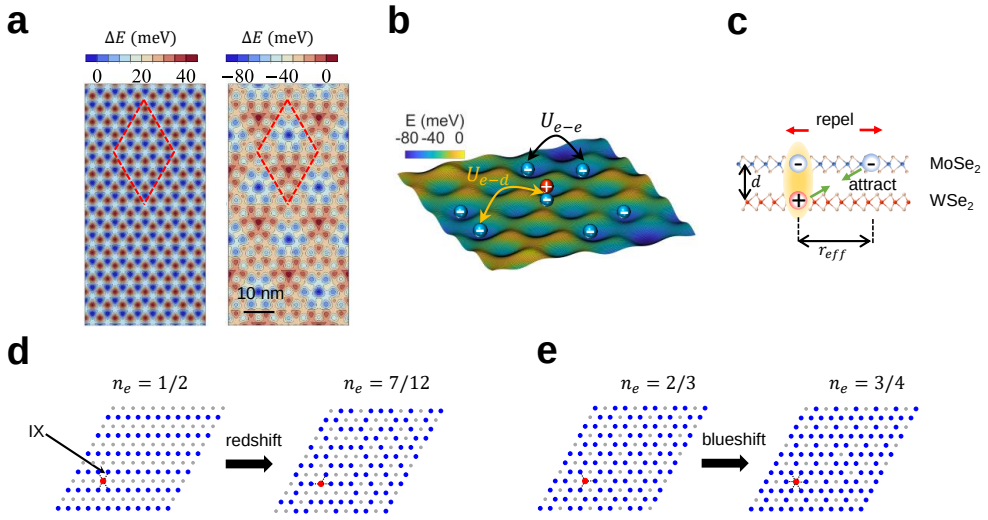

Figure 6.6: Localized dipole as a probe of electronic crystal. **a.** The calculated bottom exciton potential (left) and electron potential in the middle $MoSe_2$ layer (right) in a 1°/4° trilayer heterostructure [119]. The electron moiré unit cell is outlined by the red dashed lines. **b.** Schematic of our charge-order sensing scheme using localized IXs. The Coulomb interaction between electrons (U_{e-e}) with the moiré potential gives rise to electronic crystallization, while the IXs can sense the electrons by the Coulomb interaction between electrons and dipoles (U_{e-d}). **c.** Electrostatic model for the dipolar exciton energy change caused by the electron. With the repulsion between the electrons and attraction between the electron and hole, the form of exciton energy shift is given by $(1/r_{\text{eff}} - 1/\sqrt{r_{\text{eff}}^2 + d^2})\ /4\pi\epsilon_r\epsilon_0$, which is a blueshift. **d.** Dipolar exciton (IX) energy red shifts from filling n_e= 1/2 to n_e= 7/12. **e.** Dipolar exciton energy blue shifts from filling n_e= 2/3 to n_e= 3/4. n_e is the number of electrons per unit cell. Red dots are interlayer excitons, blue dots are occupied sites by electrons, and grey dots are unoccupied sites. The black dotted lines indicate the nearest neighbor (NN) interactions.

To examine our local sensing scheme, we increase the electron density in the sample under $E = 0$. Stable and sharp emission of localized IX (Fig. 6.7a) starts exhibiting several seemingly random spectral jumps, however, upon reversing the gate voltage (V_g), even the minutest spectral jumps ($\sim 50\ \mu$eV) are remarkably reproduced (Fig. 6.7a). We have performed V_g scans over a period of several months and the spectral jumps are perfectly reproduced. Thus, we can conclude that spectral jumps of IX, caused by the addition of electrons to the sample, are not random but highly deterministic in V_g and arise due to the change in charge configuration near localized IXs. In other words, electrons are being added to a potential landscape that is static and can be reproducibly populated with V_g. More importantly, we observe that in addition to an overall blue shift, jumps occur as both red and blue shifts, which is inconsistent with a simple picture where a monotonic increase of the electronic density in the middle $MoSe_2$ layer only increases the emission energy of IX [121]. Instead, the reproducible red- and blue-shifts of IX energies with electron doping are expected for our local sensing picture.

An important feature of charge-ordered states is global reconfiguration due to long-range electron-electron interactions. To reveal any correlations in the jump behavior and signatures of order in the potential landscape, we perform simultaneous V_g scans over two different regions (spot A and B) of the sample, separated by $\sim 4\ \mu$m, several times the excitation spot size. As shown in Fig. 6.7b, after starting with stable emission, we find that the PL qualitatively changes in both spots at a V_g marked by the dotted line L_I, followed by a sudden redshift of about 6-7 meV for several IXs in both regions at a V_g marked by the dotted line L_T. L_I marks the end of the intrinsic region whereas the redshift at L_T is consistent with the recently observed moiré trion [118, 117, 116] where the excess electron resides in the same moiré unit cell as the IX. At higher electron densities, PL from both regions broadens and becomes weak. Besides these global features, we also find several V_g values where spectral

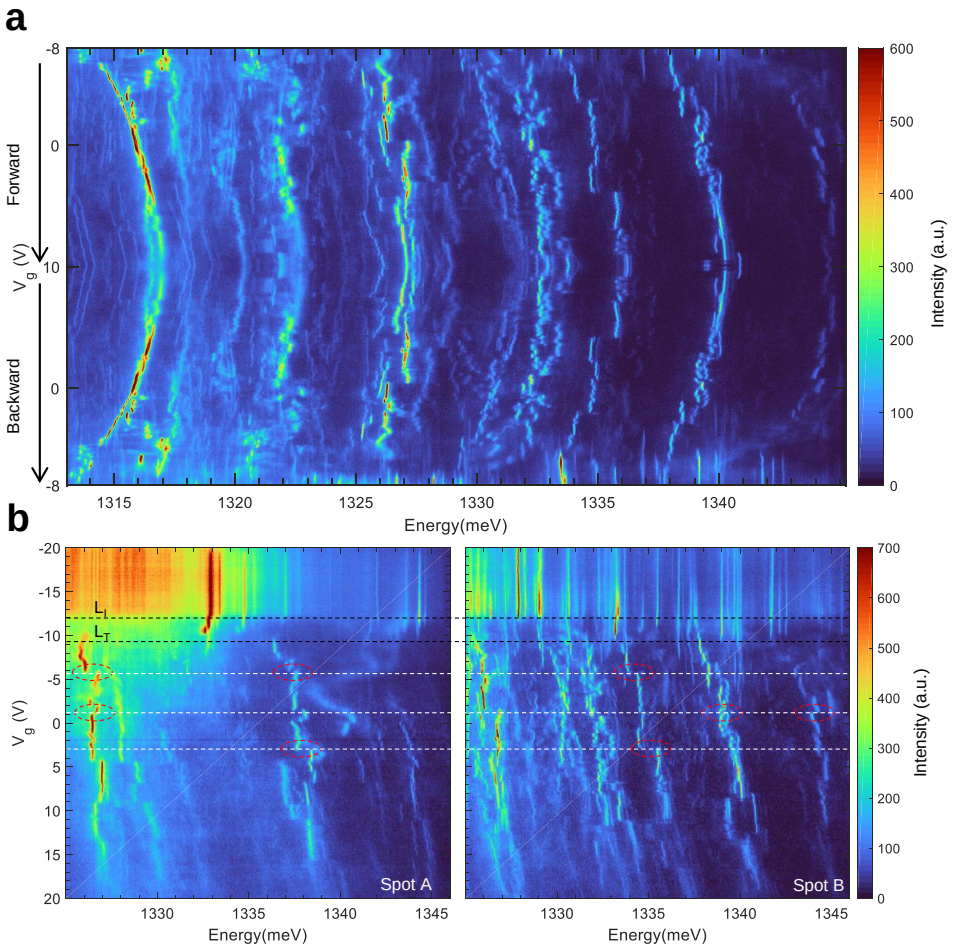

Figure 6.7: Features of correlated electrons in the doping-dependent energy shifts of IXs. **a.** Reproducible red- and blue-shifts of IX energies with electron doping. The symmetric gating V_g from -8 to 10 V (forward) introduces electrons into the system without electric field. Sudden spectral jumps of IX energies and overall blue-shift are caused by changes in Coulomb interactions between electrons and dipoles (U_{e-d}). The spectral jumps are remarkably well reproduced when V_g is reversed from 10 V to -8 V (backward), excluding the possibility of random jumps. **b.** Correlation of energy shifts between different IXs and different sample positions. Simultaneous PL gate scan of spot A (left) and spot B (right), which are separated by 4 μm, shows similar global features: no energy shift above line L_I, appearance of red-shifted peaks after line L_T and broadening of peaks after 10 V. The spectral jumps occur at the same voltages (white dashed lines) for different IXs at the same spot and across different spots, as shown by the energy shifts outlined by the red dashed ellipses. The bottom four PL gate scans with asymmetric gating show similar correlated energy shifts, now with both electric field and doping serving to stretch and therefore increasing the resolution of each energy shift.

jumps occur simultaneously, indicated by dashed white lines and dashed red ellipses in Fig. 6.7b, both within the same spot and across the two spots. These correlations imply the global reconfiguration of the charge-ordered states. In the following, we analyze whether these correlations occur at fractional fillings.

We convert the gate voltages into fillings by relabelling the voltage axis in fractions of the voltage interval defined by $\nu^* = 0$ and $\nu^* = 1$ (Fig. 6.8). $\nu^* = 1$ is traced by combining a kink feature in the reflectance together with a spectral jump in the PL spectra (see Fig.D1 in Appendix D), reminiscent of similar features in WSe_2/WS_2 heterobilayer. Remarkably, this simple relabeling of the axis shows that several jumps for both spots occur at gate voltages corresponding to integer multiples of $\nu^* = 1/12$. Our choice of 1/12 as the minimum fraction is much larger than the step size of the gate voltage scan which is $\sim$1/400, ruling out accidental correlations in jumps. As shown in Fig. 6.8a, b, the jumps which do not fall on 1/12 graduations (marked by dashed white lines) are often separated by other such jumps by a voltage interval equal to 1/3 or 1 in units of $\nu^* = 1$. To further confirm that this trend is statistically significant, we plot occurrences of ν^* modulo 1/12 of $\sim$ 330 jumps in a histogram. If most of the jumps occur at integer multiples of 1/12, we expect a peak at zero. As shown in Fig. 6.8c, there is indeed such a peak for both spots A and B. The probability of obtaining the observed peak value at zero from a completely random distribution of jumps is estimated to be $\sim$5 % ($\sim$10%) for spot A (B). Moreover, no statistically significant peak at zero is observed choosing other fractions such as 1/11 and 1/13 (Fig. 6.8d). Thus, we conclude that the spectral jumps of IX occur at certain rational fillings of the electronic moiré lattice which are in correspondence with ν^*, in other words, sudden and global redistribution of interaction-induced crystalline electrons. This is in agreement with the recent observation of correlated electronic states in $MoSe_2/WSe_2$ bilayer by reflectance[122].

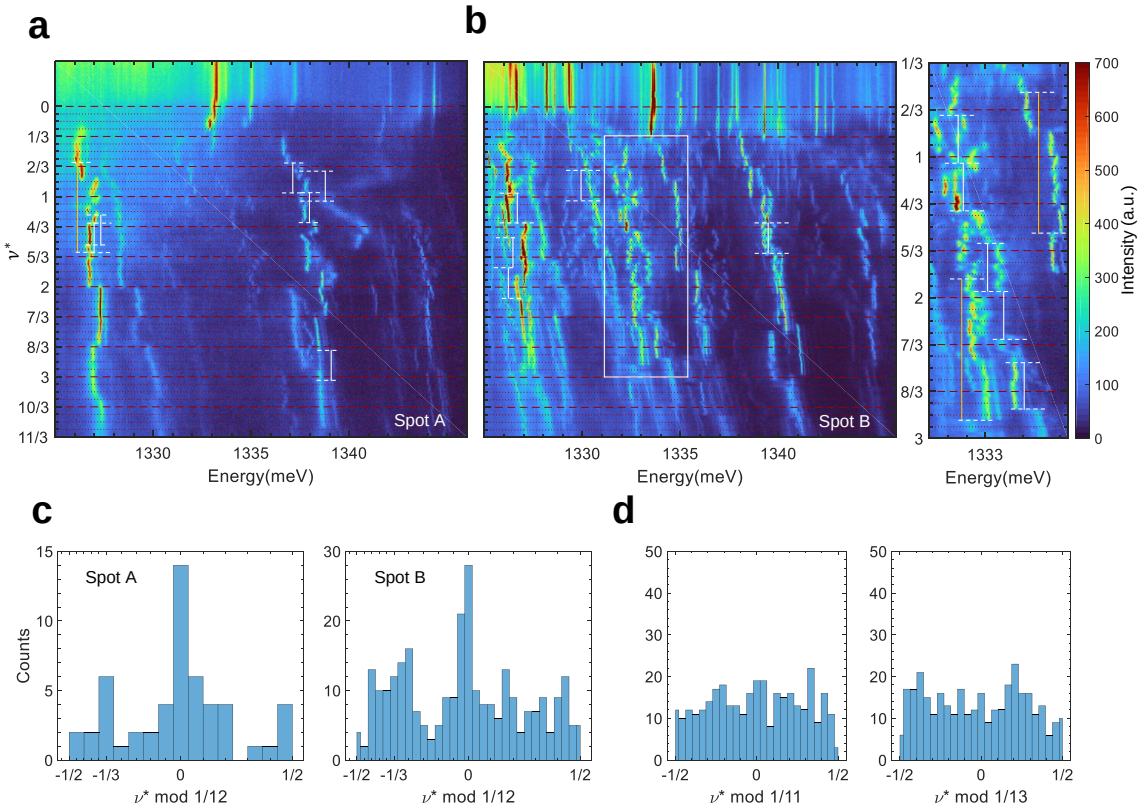

Figure 6.8: Filling-fraction assignment of the correlated electronic states. **a.** Doping dependence of PL emission at spot A with respect to the filling fractions ν^*. The dashed dark red lines indicate fractional fillings of the electronic moiré superlattice at multiples of $\nu^* = 1/12$. Most of the spectral jumps fall on these lines. The horizontal white dashed lines denote the energy shifts not falling on 1/12 fractions, however, they are often separated from each other by intervals corresponding to $\Delta\nu^* = 1/3$ (vertical white solid line) or $\Delta\nu^* = 1$ (vertical yellow solid line). **b.** Doping dependence of PL emission at spot B with respect to ν^* (left) with zoomed-in view for the white box (right). **c.** Histograms of ν^* corresponding to spectral jumps in spot A (left) and spot B (right) modulo 1/12. **d.** Histograms of jump positions modulo 1/11 (left) and 1/13 (right). Only modulus 1/12 gives a peak at 0, which means fractions with denominator 12 are the main filling fractions.

6.5 Monte-Carlo simulation of charge orders in multi-orbital lattices

To confirm the salient features of our observations and the explanation provided in the previous paragraph, we simulate the jump behavior of IXs trapped in a moiré potential (Fig. 6.6a, left) by calculating their energies at various symmetry-broken electronic crystalline states (Fig. 6.9a) of the heterotrilayer moiré lattice (Fig. 6.6a, right). We perform a classical Monte-Carlo simulation based on minimizing the electrostatic energy of electrons that we employ for the classical charges on multi-orbital lattices. The interaction between electrons is described by a screened Yukawa-like potential in the form of $V(r_{ij}) = \frac{e^2}{4\pi\epsilon_r\epsilon_0 r_{ij}} e^{-r_{ij}/r_0}$. Here $r_0 = \mathrm{N}/2$ is the interaction length scale, where N is the length of the supercell that we consider. For the 1°/4° trilayer (Fig. 6.6a), the electron moiré potential is calculated by $V_e = -(D^t(\mathbf{R}) + D^b(\mathbf{R}))/2$. Here $D^{t/b}(\mathbf{R})$ is the top/bottom exciton potential, given by $D^{t/b}(\mathbf{R}) = D_0 f_0^{t/b}(\mathbf{R}) + D_{+1} f_{+1}^{t/b}(\mathbf{R}) + D_{-1} f_{-1}^{t/b}(\mathbf{R})$, where $f_m^{t/b}(\mathbf{R}) = \frac{1}{9}\left| e^{-iK^{t/b}\cdot\mathbf{R}} + e^{-i(\hat{C}_3\mathbf{K}^{t/b}\cdot\mathbf{R} - m\frac{2\pi}{3})} + e^{-i(\hat{C}_3^2\mathbf{K}^{t/b}\cdot\mathbf{R} + m\frac{2\pi}{3})} \right|^2$ with $\mathbf{K}^{t/b}$ being the wavevector at the corner of top and bottom Brillouin zones. The three parameters are (D_0, D_{+1}, D_{-1}) = (20, -8, 83) meV for $WSe_2/MoSe_2$ heterostructure [119]. The calculated electron moiré potential shows the degenerate local minima for each unit cell, which implies the moiré potential is a multi-orbital lattice. To avoid boundary effects, we surround the simulated region with 9×9 replicas for the electron total energy calculations. The simulated electron configurations are shown in Fig. 6.9a, supporting that the electrons with interactions form crystal-like structures. For the dipolar exciton spectral jumps, we consider the excitons at bottom exciton potential minima in 1°/4° trilayers. The simulated exciton energy is achieved by summing the electron-dipole energy over all filled electrons, capturing the experimental features of red- and blue-shifts with overall blueshift (Fig. 6.9b).

We note that we do not observe complete melting of Mott-Wigner crystals away from fractional fillings. This might be explained by the creation of domain-walls between regions of commensurate electronic crystals which are energetically favorable over delocalized single-particle states (melting) due to long-range interactions [60]. In addition to a qualitative comparison, we analyze statistics of the red and blue shifts for spots A and B, as shown in Fig. 6.9c (left panel), which also agrees very well with the spectral jump statistics of our simulation (Fig. 6.9c, right panel). Finally, we convert the size of spectral jumps into an effective length r_{eff} using a charge sensing model (Fig. 6.6c). Figure 6.9d shows that r_{eff} is peaked at 7-8 nm for both data and simulation.

6.6 Interplay between charge order state and LIX valley polarization

Figure 6.10 shows the DCP of PL as a function of electron density. We note that most localized IXs have negligible DCP in the intrinsic region below 10 mT, very likely due to a residual electron-hole (e-h) exchange interaction, J_{eh} which mixes the K and -K valleys [73]. As electrons are added, the DCP jumps to a finite value once moiré trions are created. This can be explained by the singlet configuration of the two electrons in moiré trion, which quenches J_{eh} [123]. At the highest doping before which the emission broadens and disappears, DCP remains large. However, for certain moiré trions, we see a non-monotonic behavior of DCP with doping. Dashed boxes in Fig. 6.10 a to c show that the DCP suddenly vanishes at certain filling while the PL is still strong and recovers at a later fractional filling.

Moreover, as shown in Fig. 6.11a, like the neutral IX, the negligible DCP in this intermediate electron density becomes finite with a tiny magnetic field of 50 mT, because magnetic field breaks the energy degeneracy and recovers the valley

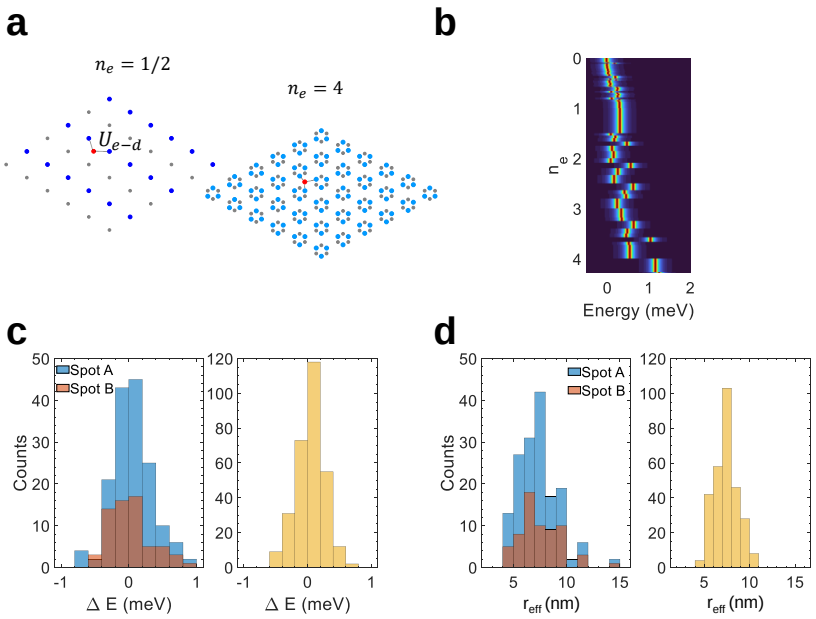

Figure 6.9: Monte-Carlo simulation of the correlated electronic states. **a.** Charge-ordered states from classical simulated annealing simulation in 1°/4° electron potential for filling factors $n_e = 1/2$ and $n_e = 4$, where n_e is the number of electrons per unit cell with a periodicity of 18 nm. The deep (light) blue dots in the left (right) panel are the first (second) orbital sites occupied by electrons and grey dots are unoccupied sites. The localized dipolar excitons (red dots) sense electron-dipole interaction (U_{e-d}) from occupied electrons. **b.** Calculated energy of the localized dipolar exciton shows red- and blue-shifts and an overall blueshift, consistent with experimental features. **c.** Histograms of spectral jump size ΔE from the experiment (left) and simulation (right). **d.** Histograms of effective length scale for the experiment (left) and simulation (right) obtained by a procedure described in Experimental details and Fig. 6.6. Both experimental and simulated results give an effective length of 7-8 nm. The ν^* where spectral jumps occur and jump size (ΔE) are manually determined for all distinguishable IX peaks.

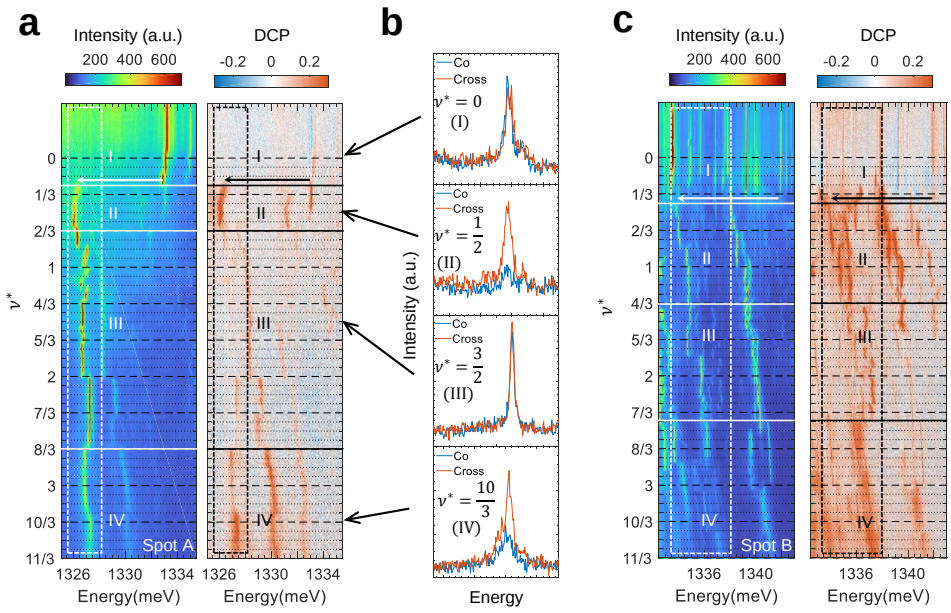

Figure 6.10: Doping dependent valley polarization of moiré excitons. **a.** PL intensity (left) and degree of PL circular polarization DCP (right) as a function of fractional fillings at spot A. The filling for the DCP data is separated by white dashed lines into four regions: (I) unpolarized intrinsic region; (II) cross-polarized trion region red-shifted by 7 meV from intrinsic counterparts; (III) unpolarized doped region; (IV) cross-polarized doped region with broad linewidth and weak intensity. The arrows indicate the 7 meV redshift and the boxes outline excitons that we focus on. **b.** Helicity-resolved PL spectra at four fillings, $\nu^* = 0$, 1/2, 3/2, 10/3. **c.** PL intensity (left) and DCP (right) change with fractional fillings at spot B, showing similar behavior as spot A.

indices[124]. To explain the disappearance of DCP at intermediate doping, we invoke a resonant tunneling-induced recovery of e-h exchange, as shown in Fig. 6.11b. At intermediate filling ν, $0 < \nu < 1$, when a moiré site spatially close to the moiré trion is singly occupied with its energy close to the electrons comprising the trion, there can be strong resonant tunneling (t) resulting in an effective e-h exchange interaction (Fig. 6.11b). This process requires spin-valley conserving tunnelings of trion electrons and the crystal electron together with J_{eh} and is equivalent to an effective spin flip-flop process between the trion hole and a crystal electron which gives a tunnel-dependent exchange of $\sim t^2 J_{\mathrm{eh}}/\delta^2$ (see Appendix D). Such a process requires sufficient proximity of the electron to the moiré trion, a condition that may not be satisfied by all localized IXs. Although this process is second order in t, it can become large at resonance. Crucially, this process requires half-filling of the participating moiré site to enable spin-flipping of the electron. At higher doping densities, when the moiré site has double occupancy, this resonant tunneling-induced exchange is either Pauli blocked or the resonance condition is lost due to additional repulsion energy, which causes the recovery of DCP. This explanation is consistent with our observations that the recovery of DCP occurs above $\nu > 1$.

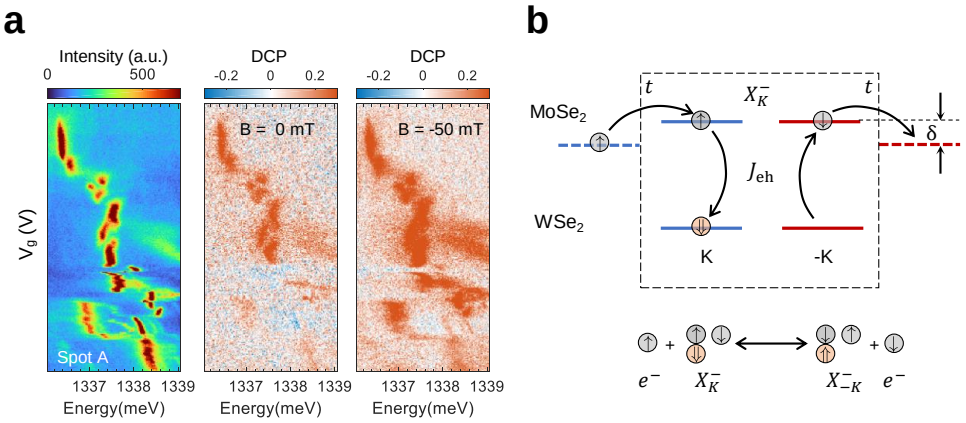

Figure 6.11: Valley mixing process for moiré trions. **a.** The PL intensity (left) and DCP at 0 T (middle) and -50 mT (right). The small magnetic field recovers the DCP, which is a signature of e-h exchange interaction quenching. **b.** Schematic of resonant tunneling induced exchange process of a K-valley moiré trion with a nearby singly-occupied moiré site at intermediate doping. The valley-conserving resonant tunnelings of moiré electron and trion electrons, denoted by tunneling amplitude t, together with e-h exchange J_{eh} enable an effective exchange interaction that reduces the DCP. The amplitude of this process, which is second-order in t, is enhanced at resonance when $\delta \approx 0$. The net effect of this process is a spin flip-flop process between the moiré electron and the trion hole. The (hermitian) conjugate of this process is not depicted here for brevity

6.7 Probing charge order reconfiguration with external electric field

Except for doping charge carriers into the sample, another tuning knob is to apply electric field by anti-symmetric gating. It has been proposed that electric field can modify the moiré potential landscape[76], which consequently changes the charge-ordered states. As shown in Fig. 6.12, certain spectral jumps (white dashed circles) disappear while other spectral jumps appear, implying that the electronic crystal is modified by the E. The electric field tunability of the electron potential landscape rules out the defect potential as the origin of electronic crystals.

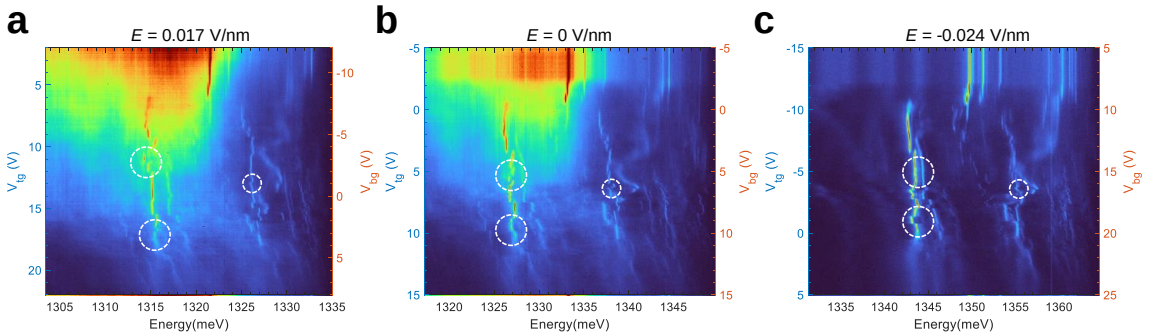

Figure 6.12: Modification of electron potential landscape by electric field. With the electric field changed from positive (**a**) to zero (**b**) and to negative (**c**), certain spectral jumps (white dashed circles) disappear while other spectral jumps appears, implying the electronic crystal modified by the E.

6.8 Reproducibility of the localized IXs-based quantum sensing technique

As we mention, disorders are hard to avoid during the fabrication of vdW heterostructure, for example, the twist angle variation from lattice reconstruction or local strain from polymer residue. Therefore, the reproducibility of the localized IXs-based quan-

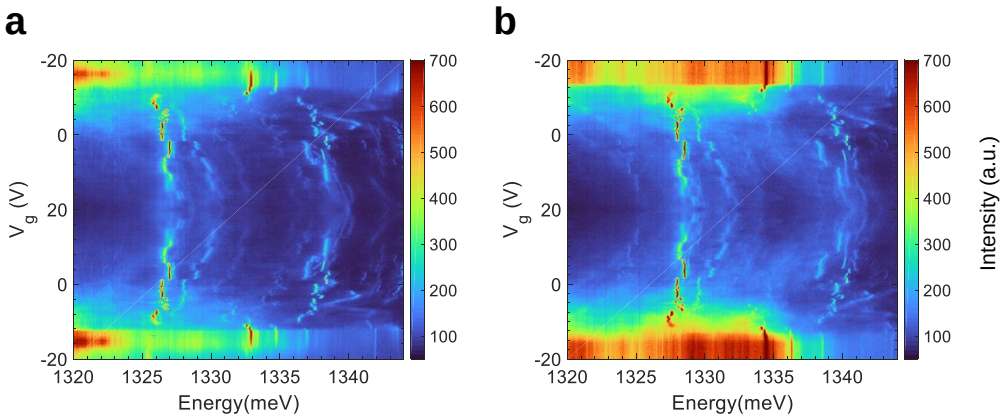

Figure 6.13: Reproducible energy shifts with electron doping at another position spot B. PL intensity of localized interlayer excitons change with V_g in the first (**a**) and second (**b**) thermal cycles. When the applied gate voltage is reversed, the energy shifts and corresponding DCP are reversed.

tum sensing technique is very important aspect for further application. We first check that the thermal cycle of warming up and cooling down the cryostat has no effect on the spectral jump behaviors (Fig. 6.13). Next, we fabricate another dual-gate $WSe_2/MoSe_2$ heterobilayer and a WSe_2/WS_2 heterobilayer samples. We observe sharp-localized IXs with doping dependent reproducible spectral red- and blue-shifts in both samples (Fig. 6.14a and Fig. 6.15a). In the $WSe_2/MoSe_2$ heterobilayer, spectral jumps agree reasonably well with assigned filling fractions (Fig. 6.14). The non-monotonic carrier density dependent DCP behaves similar to previous trilayer data6.10. In the WSe_2/WS_2 heterobilayer, which has been extensively studied for correlated states[35, 113, 114], we establish direct correspondence between such spectral jumps and the correlated electronic features detected by delocalized IXs PL and intralayer exciton reflectance contrast spectra at both electron doping $\nu_e = 1$ and hole doping $\nu_h = -1$ (Fig. 6.15b). The delocalized IXs PL DCP also show a non-monotonic DCP behavior regarding both electron and hole doping, with almost the same filling range as the $WSe_2/MoSe_2$ sample (Fig. 6.14b). Furthermore, after determining $\nu^* = 0$ and $\nu^* = 0$ for the localized IXs, all reproducible spectral jumps

land on the fractions as expected.

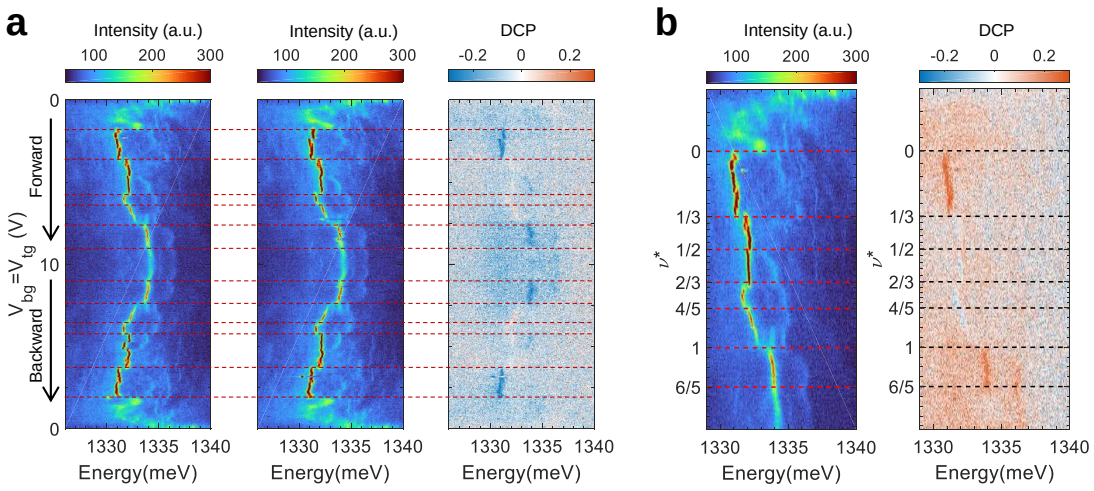

Figure 6.14: Reproducible spectral jumps and filling-fraction assignment in another $WSe_2/MoSe_2$ sample. **a.** Reproducible spectral jumps in doping dependent PL intensity spectra with σ^- (left), σ^+ (middle) excitations and DCP with σ^+ excitation (right), indicated by the red dashed lines. **b.** Assigned fractional fillings ν^* for reproducible spectral jumps. The spectral jumps agree well with the filling fractions in the PL intensity spectra (left). DCP spectra with σ^- excitation (right) show cross-polarized emission in $\nu^* \in [0, 1/3]$. With further doping, IXs become non-polarized in $\nu^* \in [1/3, 1]$ and finally recover their circular polarization after $\nu^* = 1$.

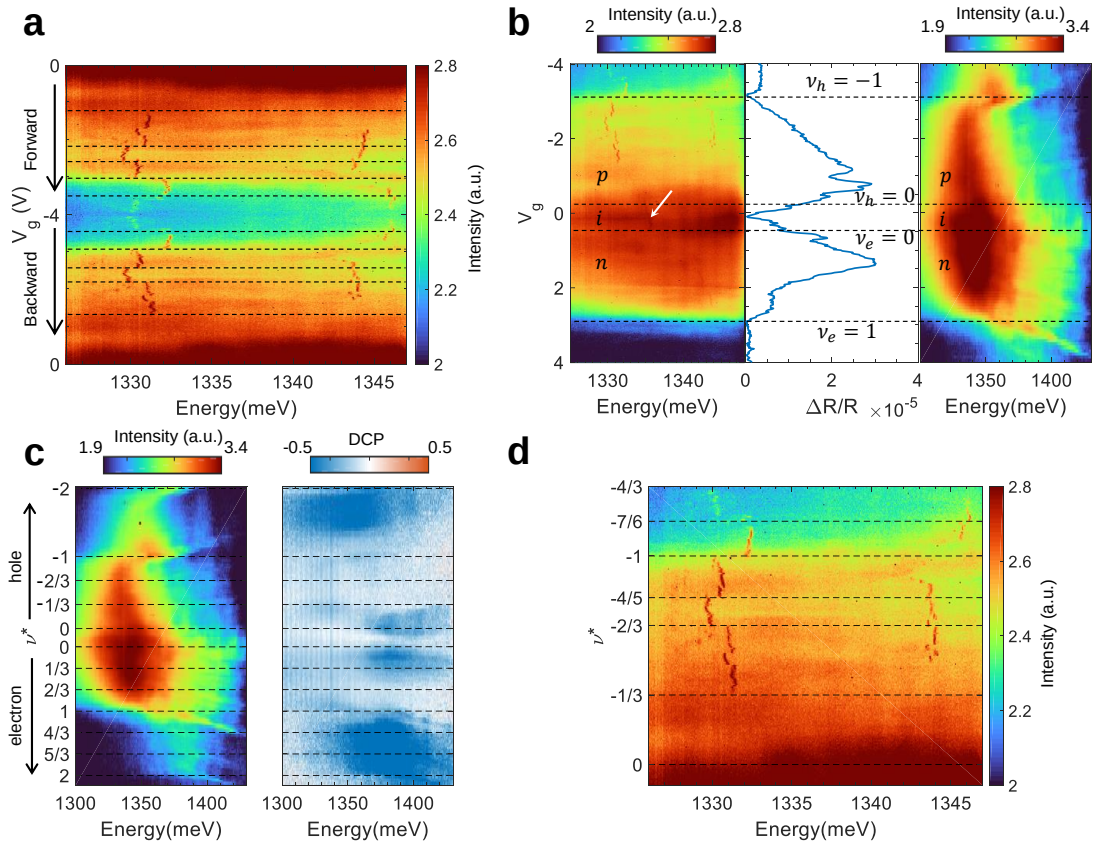

Figure 6.15: Reproducible spectral jumps and filling-fraction assignment in a WSe_2/WS_2 sample. **a.** Reproducible spectral jumps in doping dependent PL intensity spectra with linear excitation, indicated by the black dashed lines. **b.** Correlation between doping-dependent localized IX PL (left), intralayer exciton reflectance contrast spectra (middle) and broad IX PL (right). The black dashed lines separate the doping dependent spectra into hole-doped p, neutral i, and electron-doped n regions. The existence of sharp peak indicated by the defines the neutral region. The reflectance contrast spectra are acquired by lock-in technique, where a dip indicates an incompressible (insulating) state. **c.** Assigned fractional fillings ν^* for broad IX PL intensity (left) and DCP (right) with σ^+ excitation. DCP spectra show cross-polarized emission in $\nu^* \in [0, 1/3]$. With further electron doping, IXs become non-polarized in $\nu^* \in [1/3, 1]$ and finally recover their circular polarization after $\nu^* = 1$. **d.** Assigned fractional fillings ν^* for reproducible spectral jumps. The spectral jumps agree well with the filling fractions in the PL intensity spectra. All PL intensity spectra are plotted using a logarithmic scale.

6.9 Conclusion and Outlook

In conclusion, we have introduced a moiré-based local sensing scheme for correlated electronic behavior in a monolithic dual-moiré heterostructure, relying on sampling rather than scanning of the sample. Data from several localized sensors, each probing $\sim$ 10 nm, is used to uncover long-ranged charge-ordered electronic states as a function of electron density. In addition, the spin-valley degree of dipolar sensors yields information about the local spin behavior which could be used to detect quantum magnetism in the future. Our scheme, also based on optical spectroscopy, complements the recently employed techniques such as reflectance spectroscopy, and is more sensitive by not averaging over disorder or local domains. The reproducibility of such a scheme has been proved in versatile type-II van der Waals heterostructures. In addition to vdW heterostructures, proximity sensing using 2D dipolar excitons could be used to study dynamics from local charge and spin fluctuations, which are enhanced near quantum phase transitions in strongly correlated materials such as unconventional superconductors and quantum magnets. Finally, in addition to being passive sensors, localized dipolar IXs can strongly couple to other many-body systems and act as quantum impurities with an optical readout.

Chapter 7

Hybridized Quadrupolar Excitons with Tunable Oscillation Strength

In this chapter, I will introduce the creation of a new quasiparticle – quadrupolar exciton, arising from hybridization between oppositely oriented dipolar excitons. The experimental results relevant to the properties of quadrupolar excitons are reported in an arXiv preprint[4].

7.1 Previous work on exciton hybridization

An exciton, which comprises of a Coulomb-correlated electron-hole pair, is an elementary excitation of a semiconductor resembling a hydrogen atom albeit with possible modifications arising from lattice effects [125]. In addition to atom-like neutral excitons, excitonic complexes such as trions and biexcitons, resembling ions and molecules, add further richness to exciton physics [126]. In vdW heterostructures of 2D semiconductors, the layer degree of freedom can endow excitons with additional internal structure, such as a static dipole moment in interlayer excitons of heterobilayers with type-II band alignment, affecting their interactions and light-matter coupling [40, 127]. The existence of interlayer and intralayer excitons in the same

structure enables mixing of them so that layer-hybridized excitons are formed via interlayer resonant tunneling of electrons or holes. This has been observed in AB stacked WS_2/WSe_2, arising from the hole tunneling between WS_2 higher valence band and WSe_2 lower valence band with the same spin indices and similar energies (Fig. 7.1a)[128]. The oscillation strength is then redistributed between the interlayer and intralayer excitons in the coupling regime. Such exciton hybridization is however not allowed in AA stacked WS_2/WSe_2, because the energy nearly-degenerate bands have opposite spin indices and forbid the resonant tunneling of electrons or holes (Fig. 7.1b). In other vdW heterostructures hosting interlayer and intralayer excitons with similar energies and spin indices, such as type-I $WS_2/MoSe_2$ heterobilayer (Fig. 7.1c) and $MoSe_2/MoSe_2$ homobilayer (Fig. 7.1d), the hybridization between them are also observed as expected[33, 39]. Nevertheless, the hybridization between two interlayer excitons have not been realized. Here, using a $WS_2/WSe_2/WS_2$ heterotrilayer, we create a quantum superposition of oppositely oriented dipolar interlayer excitons – a quadrupolar exciton – wherein an electron is layer-hybridized in two WS_2 layers while the hole localizes in the middle WSe_2 layer. The quadrupolar exciton wavefunction is characterized by nonlinear Stark shift and modified electron-hole overlap (oscillation strength) under electric field. Moreover, the presence of the additional layer, in comparison to heterobilayers, enriches exciton-exciton interactions, enabling a many-body, interaction-driven transition to dipolar excitons.

7.2 Experimental details

We fabricate dual-gated $WS_2/WSe_2/WS_2$ heterotrilayer device using PC-based transfer technique [89]. WSe_2 and WS_2 monolayers, few-layer graphene and thick hBN are mechanically exfoliated from bulk crystals onto 300 nm SiO_2/Si substrates. We use the tear-and-stack method [120] to pick up half of a WS_2 flake, align with the WSe_2

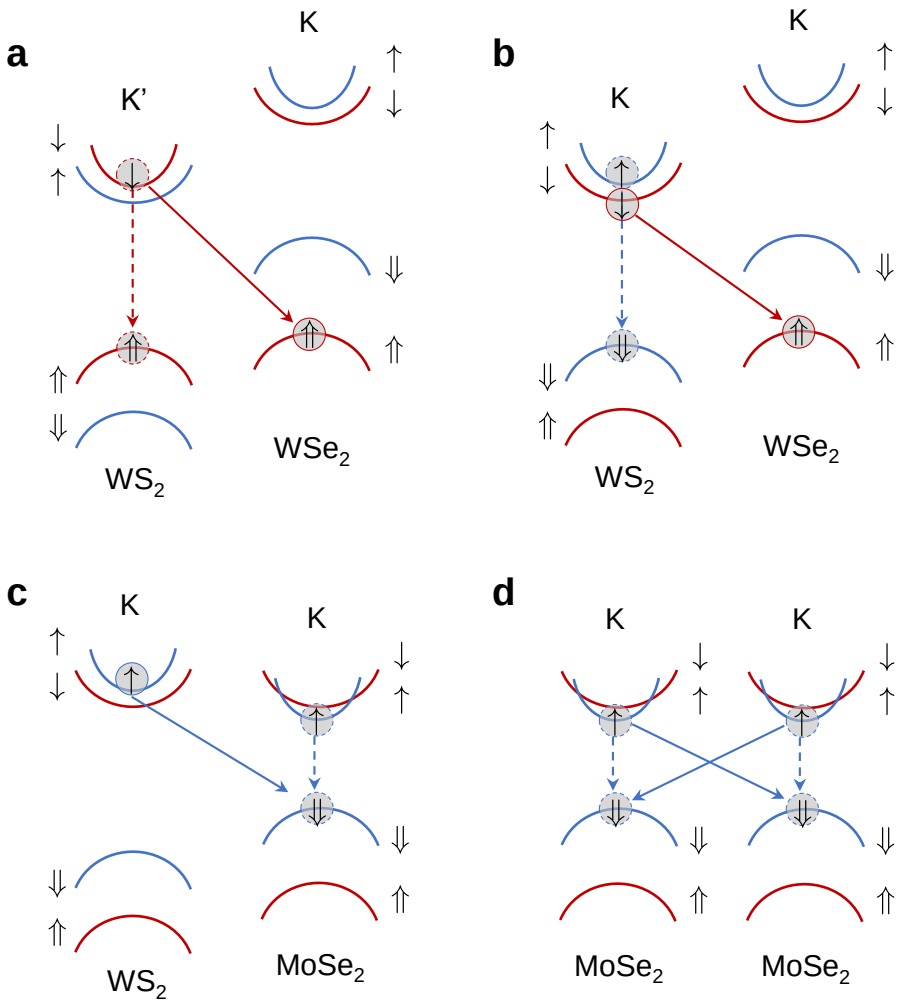

Figure 7.1: Hybridized interlayer and intralayer excitons. **a.** Hybridization between interlayer (solid line) and intralayer (dashed line) excitons by hole tunneling for AB-stacked type-II TMD heterobilayer WS_2/WSe_2. **b.** No hybridization for AA-stacked WS_2/WSe_2 as a result of spin conservation. **c.** Hybridization between interlayer and intralayer excitons for AA-stacked type-I TMD heterobilayer $WS_2/MoSe_2$. **d.** Mixing of interlayer and intralayer excitons for homobilayer $MoSe_2/MoSe_2$.

layer within 1° uncertainty and pick up the other half of the WS_2 flake without rotation (AA stacking, Device 1, 2, 4 in the main text, Device 5 in the Appendix E) and with 60° rotation (AB stacking, Device 3 in the main text) relative to the top WS_2 in order to protect/break the mirror symmetry in AA/AB samples. AA/AB stacking is defined based on the outer two WS_2 layers. We fabricate 5 devices to show the reproducible properties of the quadrupolar excitons. All data in the Fig. 7.3, 7.4, 7.5 are from Device 1 with the exception of Fig. 7.5a,c, which are from Device 2, and Fig. 7.4g from Device 3. The data in Fig. 7.6, 7.7 are acquired in Device 4. Figure 7.2a show a microscope image of one of our heterotrilayer samples. The sample is encapsulated in 20-40 nm hBN with dual gates for independent control of displacement field and carrier doping (Fig. 7.2b). The heterostructure consists of both heterotrilayer and heterobilayer to directly compare trilayer and bilayer exciton properties. The stacking order is chosen to be AA for the outer WS_2 layers because AB stacking has negligible hybridization with spin-valley conserving tunneling [14]. AA stacked heterotrilayers hosting quadrupolar excitons actually have a 60° twist angle between WS_2 and middle WSe_2 (see Appendix E).

The schematic of our AA $WS_2/WSe_2/WS_2$ sample illustrates the possible exciton species existing in the heterostructure (Fig. 7.2c). If the outer layers are uncoupled, this heterostructure can be expected to host oppositely oriented dipolar interlayer excitons because of type-II band alignment between WSe_2 and WS_2. However, in the presence of a finite tunnel coupling, the electron is layer-hybridized between WS_2 layers, whereas the hole resides in the middle WSe_2 layer. The strength of tunneling determines the energy difference between the lower energy symmetric (Fig. 7.2d) and higher energy antisymmetric (Fig. 7.2e) hybridized electronic states. More importantly, the symmetric (antisymmetric) electronic state has a finite (vanishing) weight in the WSe_2 layer. Together with the hole in the middle layer, the resulting excitonic states have no net dipole moment but a quadrupole moment. In other words, elec-

tron tunneling hybridizes the two degenerate, oppositely oriented dipolar excitons into symmetric and antisymmetric quadrupolar excitons. However, quadrupolar excitons in heterotrilayers should be contrasted with earlier reports on hybridized interlayer and intralayer excitons in bilayers [33, 39, 67, 128], which have a dipolar character due to broken mirror symmetry.

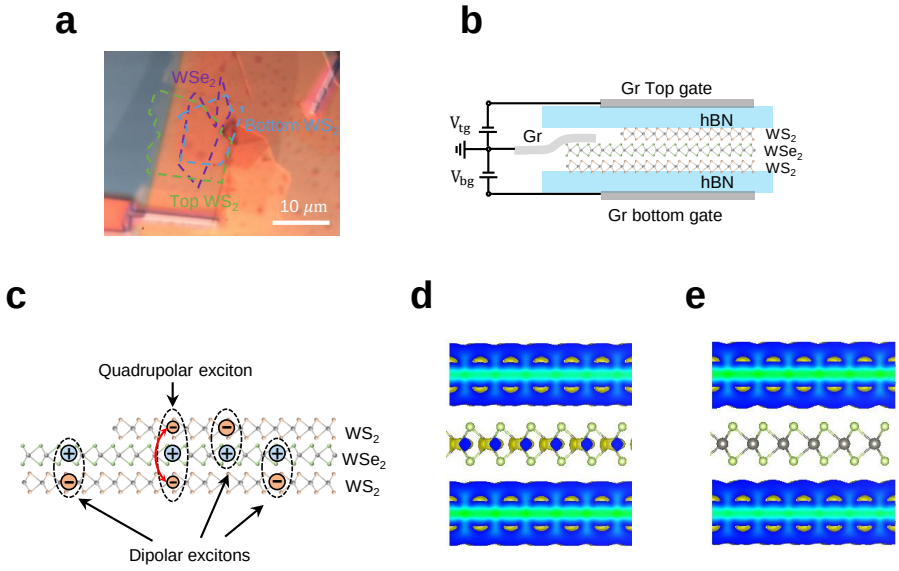

Figure 7.2: Quadrupolar and dipolar excitons in a TMD heterostructure. **a, b.** Sample picture (**a**) and schematic geometry (**b**). The dual gates allow independent application of doping and electric field to the sample. **c.** Schematics of exciton species in bilayer and trilayer heterostructures. The bilayer region hosts one species of dipolar excitons, while the trilayer region can host two antiparallel dipolar excitons, as well as the quadrupolar exciton, which is a hybridized state of the two dipolar excitons. **d.** Electron wavefunction distribution in symmetric quadrupolar excitons, which is delocalized across the two WS_2 layers with a finite weight in the middle WSe_2 layers. **e.** Electron wavefunction distribution in antisymmetric quadrupolar excitons, which is delocalized across the two WS_2 layers with a vanishing weight in the middle WSe_2 layers.

The theoretical argument of hybridization and wavefuction modification in the paper is based on DFT ab initio calculation done by our collaborators. The ab initio calculations are performed within the Vienna Ab initio Simulation Package (VASP)[129] using a projector-augmented wave (PAW) pseudopotential in conjunction with the

Perdew–Burke–Ernzerhof (PBE)[130] functionals and a plane-wave basis set with an energy cutoff at 400 eV. The unit cells are chosen to consist of $WS_2/WSe_2/WS_2$ trilayers with a lattice constant of 3.154 Å and interlayer spacing of 5.9 Å or 6.2 Å. A vacuum region of 20 Å is applied to avoid artificial interaction between the periodic images along the vertical direction. The first Brillouin zone of the heterostructure was sampled using a 15×15×1 k-point grids. The structures at ground states were fully relaxed until the force on each atom was < 0.01 eV Å^{-1}. The van der Waals interactions were included using the opt88 functional[131]. For the structures with modified interlayer hybridizations, the interlayer distances were artificially modulated to get insight into the influence of various stackings. Spin-orbital couplings are included in the calculations of electronic structures.

7.3 Observation of quadrupolar excitons in heterotrilayers

Photoluminescence spectroscopy at cryogenic temperature has been proved to be a power tool to study excitons in the previous chapters. Figure 7.3a, b show low temperature ($\sim$ 6K) PL spectra of the trilayer and bilayer regions together with the corresponding photoluminescence excitation (PLE) spectra. Both the emission energy and excitation resonance energy are redshifted in the trilayer region compared to the bilayer region. The trilayer spectra are dominated by three peaks which we assign to, in order of decreasing energy, a spin-triplet IX, a spin-singlet IX and the spin-singlet IX phonon replica, based on earlier reports in WSe_2/WS_2 heterobilayer [132, 133]. The three peak structure is robust across different AA stacked samples with similar energy and linewidth, implying that they are free excitons (see Fig. E1 Appendix E).

To distinguish between quadrupolar and dipolar excitons, the out-of-plane electric field ($\mathbf{E} = E_z\hat{z}$) response of PL is explored here. As shown in Fig. 7.4a, the PL from

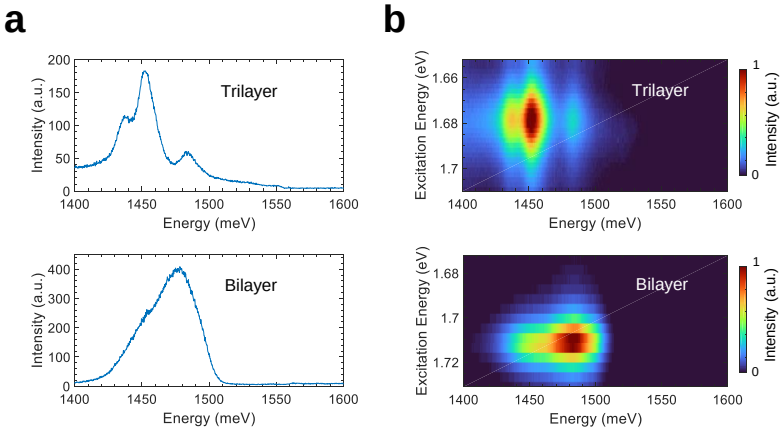

Figure 7.3: Trilayer and bilayer PL emissions. **a.** Representative photoluminescence (PL) spectra from the trilayer (top) and bilayer sample regions (bottom). The trilayer shows a three-peak structure, different than the bilayer emission. Excitation was 40μW at 1.68 eV (1.71 eV) for the trilayer (bilayer). The bilayer peak is bluer than the strongest trilayer peak. **b.** Photoluminescence excitation spectroscopy of the trilayer and bilayer region at $\mathbf{E} = 0$. Both regions show one resonance, which is 1.68 eV (1.71 eV) for the trilayer (bilayer).

the bottom bilayer region shifts linearly, displaying both red and blueshifts depending on the direction of $\mathbf{E}$. Thus, the bilayer emission behaves as expected for dipolar excitons with an energy shift $\delta\mathcal{E} = -\mathbf{d}\cdot\mathbf{E}$ [42]. Moreover, the sign of the slope of the energy shift, $d\mathcal{E}/dE_z$, which is proportional to the dipole moment, is consistent with the layer ordering in the bilayer region. In stark contrast, the PL from the trilayer region redshifts for either direction of $\mathbf{E}$, with a characteristic nonlinear shape (Fig. 7.4b). While we measure $\mathbf{E}$-dependence of the PL with opposite voltages applied to the top and bottom gates so as to not dope carriers in the sample, imperfections in gate configurations can lead to a small amount of unintentional doping which could also result in energy shifts. By monitoring the reflectance of intralayer excitonic resonances, which remain unchanged with $\mathbf{E}$, we conclude that accidental doping, if any, is not sizable enough to cause the observed energy shifts of tens of meV (see Fig. E2 in Appendix E). However, we note that the PL in both the bilayer and trilayer regions for $E > 0.046$ V/nm displays slight broadening and reduction in intensity

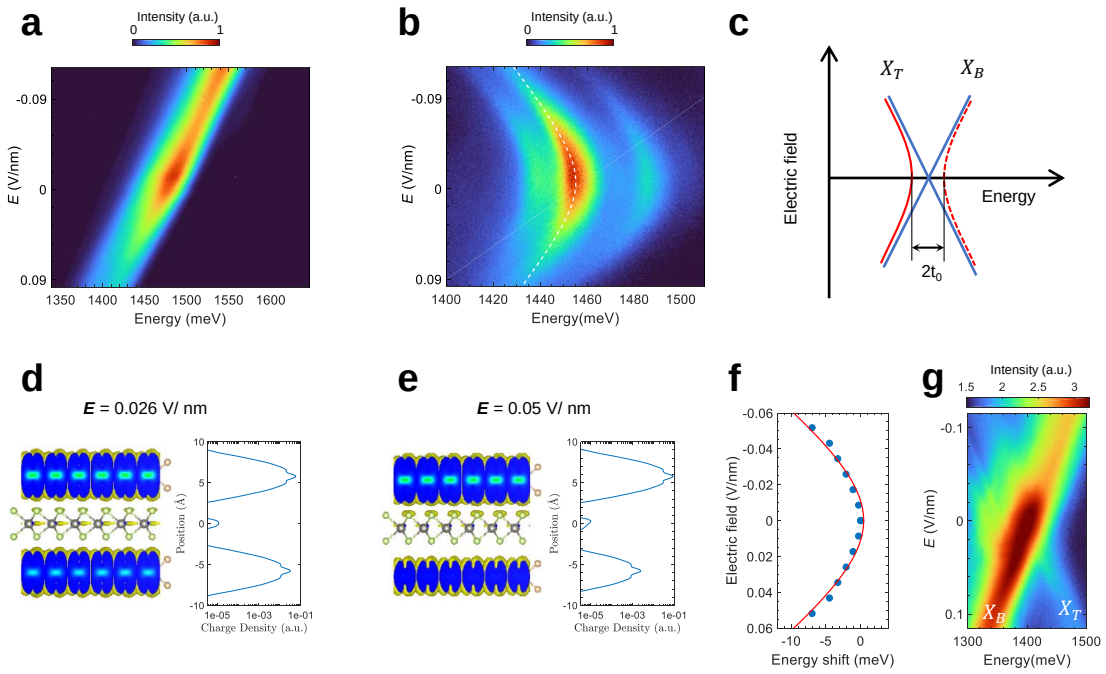

Figure 7.4: Electrical field tunable dipole hybridization in quadrupolar excitons. **a.** Electric field (**E**) dependent PL of bilayer excitons. The peak blueshifts or redshifts depend on the direction of the out-of-plane electric field. **b.** **E**-dependent PL of trilayer excitons. The dashed white line is a hyperbolic fit of the main peak. The three-peak structure only redshifts with the electric field. **c.** Hybridization of the top and bottom dipoles. X_B (X_T) is the bottom (top) dipole and t_0 is the tunnelling strength at zero electric field. The solid red line is the lower energy symmetric branch, and the dashed red line is the higher energy antisymmetric branch. **e, d.** DFT calculation of the electron charge density across the layers at $\mathbf{E} = 0.026$V/nm (**e**) and $\mathbf{E} = 0.05$V/nm (**d**). When **E** is increased, the electron density is shifted from the bottom layer to the top layer, and the electron density in the middle layer is reduced. **f.** The solid blue dots represent the DFT calculated shifts of the quadrupolar exciton interband transition energy as a function of **E**. The red line shows the hyperbolic fit in **(b)**. **g.** **E**-dependent PL of an AB stacked trilayer (Device 3). The top and bottom dipoles do not hybridize. The excitation power is 40μW for **(a)** and **(b)**, and the excitation energies are 1.71 eV and 1.68 eV, respectively. The excitation power is 5μW for **(g)** with energy 1.685 eV.

compared to $E <$ -0.046 V/nm. We attribute this to small, unintentional doping for $E >$ 0.046 V/nm, which causes a slight asymmetry in the nonlinear redshift about **E** = 0 in the trilayer region. Finally, we observe similar **E**-dependent nonlinear redshift of PL in three other samples which leads us to conclude that it is a generic feature of $WS_2/WSe_2/WS_2$ heterotrilayers (see Fig. E3 in Appendix E). Unlike the dipolar exciton in the bilayer region, $d\mathcal{E}/dE_z$ (or the magnitude of dipole moment) in the trilayer region steadily increases from zero with increasing $|\mathbf{E}|$, for small $|\mathbf{E}|$. This behavior is consistent with that of a quadrupolar exciton, which has not a dipole moment but a quadrupolar moment instead at zero **E**.

To gain a qualitative understanding of the nonlinear redshift, we start by considering uncoupled top and bottom dipolar excitons with opposite dipole moments. Under an applied **E**, the energy of the two dipolar excitons should shift in opposite directions, resulting in 'X'-shaped dispersing branches (Fig. 7.4c). If we assume a finite hybridization of the two branches due to resonant tunneling of electrons, the intersecting 'X'-like branches should turn into an avoided crossing where the lower (higher) energy branch corresponds to the symmetric (antisymmetric) superposition of top and bottom dipolar excitons – quadrupolar excitons [134]. In this case, the lower (higher) energy symmetric (antisymmetric) branch only redshifts (blueshifts), asymptotically merging with the dipolar branch (Fig. 7.4c). Thus, we conclude that the redshifting of PL in the trilayer region is consistent with a symmetric quadrupolar exciton. The antisymmetric quadrupolar branch is at higher energy and is expected to be much weaker in emission under non-resonant excitation due to relaxation to the symmetric branch. Furthermore, oscillator strength, which is characterized by electron-hole overlap, is drastically reduced for the antisymmetric quadrupolar exciton because of the presence of a node in the electronic wavefunction at the location of the hole in the WSe_2 layer (Fig. 7.2e). The combination of these two effects possibly renders the antisymmetric quadrupolar exciton optically dark in our experiments.

To estimate the hybridization or tunnel coupling strength t_0 from the nonlinear redshift (Fig. 7.4b), we need to quantitatively describe quadrupolar exciton energy shift behavior under an out-of-plane electric field. If we assume that t_0 remains constant in the accessible $\mathbf{E}$ range, the quadrupolar exciton can be considered as a hybridized state of two possible dipolar excitons - top ($|\Psi_t\rangle$) and bottom ($|\Psi_b\rangle$). Therefore, the dipolar basis can be written as:

$$\begin{pmatrix} |\Psi_t\rangle \\ |\Psi_b\rangle \end{pmatrix}$$

Assuming the external $\mathbf{E}$ points along the direction of the top dipole, the Hamiltonian in this basis is:

$$H_d = \begin{pmatrix} \Delta E_{\mathrm{t}} & -t_0 \\ -t_0 & \Delta E_{\mathrm{b}} \end{pmatrix}$$

where the dipolar excitons' Stark shifts ΔE_{t} and ΔE_{b} are given by:

$$\Delta E_{\mathrm{t}} = -\alpha(e\mathbf{E}\cdot\mathbf{d_0}), \Delta E_{\mathrm{b}} = +\alpha(e\mathbf{E}\cdot\mathbf{d_0}),$$

where e is the elementary charge of the electron, $\mathbf{E}$ is the external $\mathbf{E}$, $\mathbf{d_0}$ is the bare dipole moment of the dipolar excitons, and α is a parameter that accounts for the effects of screening inside the material. Upon diagonalization, we find two eigenstates, the symmetric ($|\Psi_s\rangle$) and antisymmetric ($|\Psi_a\rangle$) quadrupolar excitons:

$$\begin{pmatrix} |\Psi_s\rangle \\ |\Psi_a\rangle \end{pmatrix} = \begin{pmatrix} \frac{1}{\sqrt{2}}(|\Psi_t\rangle + |\Psi_b\rangle) \\ \frac{1}{\sqrt{2}}(|\Psi_t\rangle - |\Psi_b\rangle) \end{pmatrix} \tag{7.1}$$

with the Hamiltonian:

$$H_q = \begin{pmatrix} -\sqrt{\alpha^2(e\mathbf{E}\cdot\mathbf{d_0})^2 + t_0^2} & 0 \\ 0 & +\sqrt{\alpha^2(e\mathbf{E}\cdot\mathbf{d_0})^2 + t_0^2} \end{pmatrix}. \tag{7.2}$$

As argued before, we observe only the symmetric branch of the quadrupolar exciton due to its lower energy and higher oscillator strength, and therefore the characteristic hyperbolic Stark shift of the quadrupolar exciton is given by:

$$\Delta E_s = -\sqrt{\alpha^2(e\mathbf{E}\cdot\mathbf{d_0})^2 + t_0^2}. \tag{7.3}$$

Since we convert the voltage into $\mathbf{E}$ using the Stark shift of dipolar excitons in the bilayer region, $\alpha = 1$ for the bilayer. For the trilayer, $\alpha = 0.58$ by fitting the asymptotic line using the same $\mathbf{E}$ as the bilayer, which is found to be similar in both Device 1 and Device 4. Using the above parameters, we can get a rough estimate of the strength of hybridization or tunnel coupling, $t_0 = 16 \pm 5$ meV.

While the above analysis is performed assuming a constant hybridization, t_0, of opposite dipolar excitons, we can obtain a more accurate picture by considering how the layer-hybridized electronic wavefunction evolves with $\mathbf{E}$. Under an out-of-plane electric field, we can assume that the hole distribution remains unchanged and hence the excitonic energy shift is primarily determined by the changes to the electronic wavefunction. To this end, we performed DFT simulations to calculate the electronic wavefunction of the symmetric state as a function of $\mathbf{E}$. Figure 7.4d-e show the electronic charge distribution at two values of $\mathbf{E}$. As expected, with increasing $|\mathbf{E}|$, the electronic charge distribution becomes asymmetric about the hole in the middle WSe_2 layer, resulting in an increased dipole moment. We calculate the energy shift for $\mathbf{E}$-dependent symmetric quadrupolar exciton as shown in Fig. 7.4f, in very good agreement with our experimental results at the level of DFT calculation, due to

similar binding energy of symmetric and antisymmetric branches [134]. We also note that our DFT calculations neglect moiré potential-related effects, suggesting that the latter do not play an essential role in the formation of quadrupolar excitons.

To further confirm that the observed behavior in the trilayer region is indeed due to tunnel coupling, we fabricated a sample with AB stacking order of the outer WS_2 layers, which should suppress layer hybridization due to spin-conserving tunneling. As shown in Fig. 7.4g, we observe dipolar exciton-like response under **E** with the PL displaying linear red and blueshift depending on the direction of **E**, as expected from a lack of tunnel coupling. As a result, the AB stacked trilayer is decoupled into bilayers, consistent with DFT calculations (see Fig. E4, Note 2 in Appendix E).

7.4 Electric field tunable oscillation strength of quadrupolar excitons

Having established the existence of quadrupolar excitons in heterotrilayers, we study the implications of the quadrupolar exciton wavefunction on light-matter coupling. A key quantity in determining the latter is the overlap of electron and hole wavefunction, i.e., the oscillation strength, which determines the radiative lifetime of the exciton. Owing to the tunneling of electrons through the WSe_2 barrier which hosts holes, the symmetric quadrupolar exciton has a larger electron-hole overlap compared to the dipolar exciton. As the electron-hole overlap in the symmetric quadrupolar exciton depends sensitively on **E**, it can be tuned to control excitonic radiative lifetime and hence light-matter coupling.

To test this hypothesis, we performed time-resolved PL lifetime measurement of the emission from bilayer and trilayer regions as a function of **E**. As shown in Fig. 7.5a and c, with increasing $|\mathbf{E}|$, PL lifetime of the heterotrilayer steadily increases from ~ 0.4 to 0.7 ns. As the PL lifetime depends on both radiative and non-radiative

lifetimes, an increase in PL lifetime could arise from a reduction in non-radiative processes or an increase in radiative lifetime, or a combination thereof. The presence of a small out-of-plane electric field should have a minor effect on the non-radiative lifetime. In fact, any unintentional doping under **E** will only decrease the non-radiative lifetime by carrier-induced relaxation. Thus, we attribute this increase in lifetime to a reduction in electron-hole overlap of the quadrupolar exciton with a polarizing $|\mathbf{E}|$. If Eq.(7.1) ideally describes the symmetric quadrupolar wavefunction, the overlap between electron and hole (oscillation strength) should be twice that of the dipolar one, in other words, quadrupolar exciton radiative lifetime should be half of dipolar exciton radiative lifetime at zero **E**. Reasonably high **E** de-hybridizes quadrupolar excitons to be either top or bottom dipolar excitons, which should increase the lifetime of quadrupolar excitons by twice, consistent with Fig. 7.5c. The trilayer region of Device 1 also shows an increased lifetime with **E** but by a smaller amount (see Fig. E6 in Appendix E). In contrast, Fig. 7.5b and d show that the bilayer region lifetime has negligible change for $E < 0$. The decrease in PL lifetime of bilayer region for $E > 0.03$ V/nm is consistent with the observed reduction in PL intensity in Fig. 7.4a and possibly arises from non-radiative relaxation due to unintentional carrier doping. As the bilayer exciton is longer lived, it is expected to be more sensitive to carrier-induced non-radiative channels.

7.5 Many-body interaction driven quadrupolar to dipolar transitions

As neutral quasiparticles, excitons in general interact weakly, but dipolar excitons can interact strongly via dipole-dipole interactions at sufficiently large excitonic densities [1, 41, 135]. Whereas interlayer dipolar excitons in heterobilayers interact repulsively, repulsive quadrupolar interactions between hybridized excitons in heterotrilay-

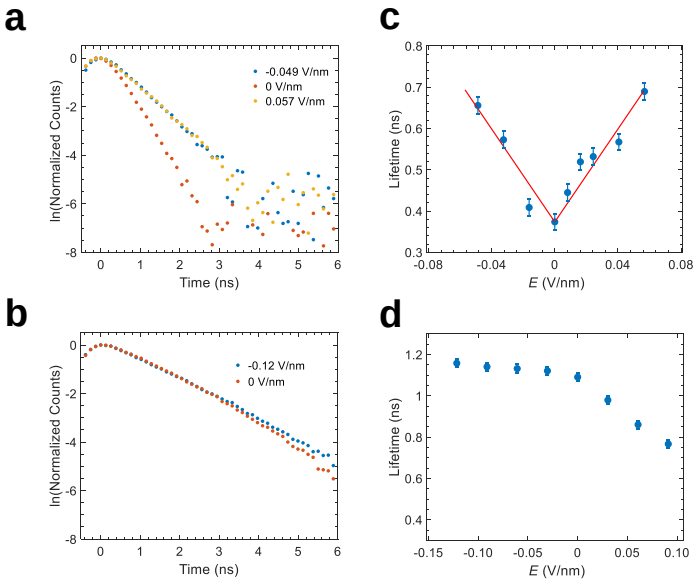

Figure 7.5: Electrical control of quadrupolar and dipolar exciton lifetimes. **a.** Time-resolved PL of the trilayer exciton with a positive, negative and zero **E**. **b.** Time-resolved PL of the bilayer exciton as a function of **E**. **c.** Fitted lifetime of the trilayer exciton as a function of **E**. The trilayer exciton lifetime increases with **E** in either direction. The red line is the linear fit of lifetime versus **E**, which gives a slope of 5.7 $\pm$ 0.6 ns/(V/nm) at negative voltage and a slope of 5.7 $\pm$ 0.5 ns/(V/nm) at positive voltage. **d.** Fitted lifetime of the bilayer exciton as a function of **E**. The bilayer lifetime has negligible **E** dependence.

ers are expected to be weaker. However, the additional WS_2 layer can qualitatively modify the picture such that exciton-exciton interactions and excitonic internal structure couple strongly resulting in correlated excitonic phases and quantum phase transitions between them [134]. Exciton-exciton interactions can be studied by varying the steady-state excitonic density, n_{ex}, which can be efficiently varied, for example, by changing the intensity of the excitation laser resonant with the intralayer excitonic resonance.

Figure 7.6 shows **E**-dependence of PL spectra in trilayer regions of Device 4 as the excitation laser intensity is increased. At a low power of 35 μW (Fig. 7.6a), the electric field dependence of PL energy has the characteristic nonlinear redshift of the hybridized quadrupolar exciton, as discussed above. However, the electric field dependence at a high power of 1 mW exhibits a linear shift, reminiscent of dipolar excitons (Fig. 7.6b). To quantitatively visualize the evolution of quadrupolar excitons to dipolar excitons, we extract the slope of the energy shift versus **E**, which is proportional to the average dipole moment. Fig. 7.6c shows that the slope increases with power and saturates around 1 mW with a maximum slope of $\sim$370$\pm$10 meV/(V/nm), which is comparable to the slope (380$\pm$10 meV/(V/nm)) at low powers in the large **E** limit (see Fig.E12 in Appendix E). The transition from quadrupolar excitons to dipolar excitons with increased power suggests that the two anti-parallel dipoles become de-hybridized with increased n_{ex}. Further evidence for de-hybridization is provided by blueshift of decoupled top and bottom dipoles with respect to the symmetric quadrupolar excitons, consistent with the hybridization picture of Fig. 7.4c. The PL spectra at different powers in Fig. 7.6d track the blue-shift of the trilayer excitons from low to high power at a finite **E** (8.4 mV/nm above the turning point). The peak energies are extracted and plotted in Fig. 7.6e, showing a blueshift of $\sim$6 meV.

As repulsive quadrupolar interactions are weak, the blueshift likely arises from Pauli exclusion owing to the fermionic nature of electron and hole comprising the

exciton. In particular, our model to explain de-hybridization, which is based on excitonic phase-space filling and weakening of electron-hole interaction with increasing n_{ex} [136, 137], captures the blueshift (Fig. 7.6e) reasonably well. Our model agrees with the data for $n_{ex} \sim 10^{12}\text{cm}^{-2}$ at 1 mW of excitation power. Only the lower energy branches for either **E**-direction are observed, since the electron in de-hybridized dipolar excitons still has the layer degree of freedom and it is energetically favorable to layer-polarize with finite **E**.

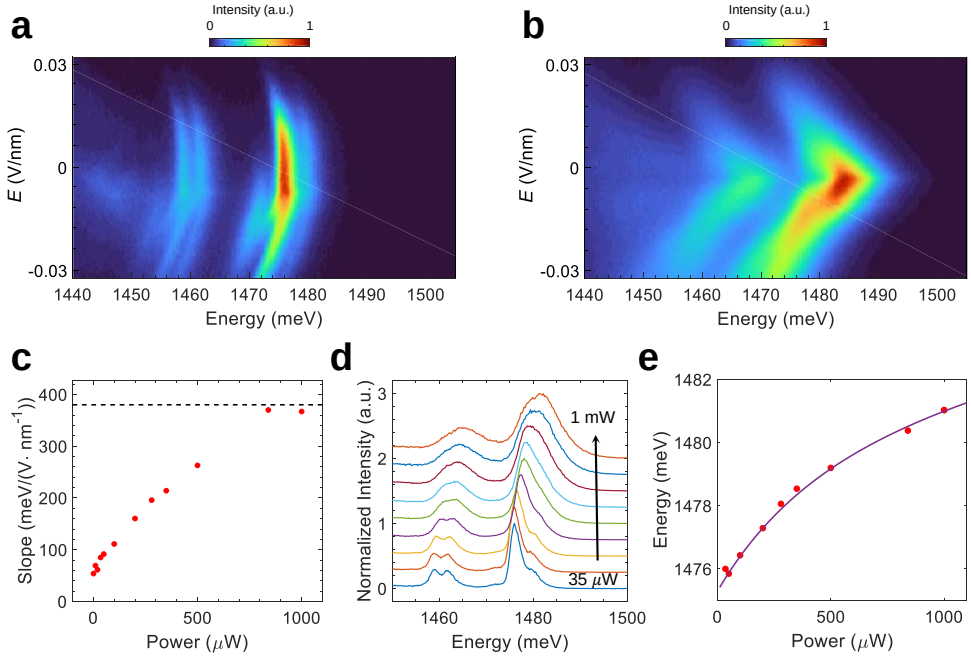

Figure 7.6: Density-driven quadrupolar to dipolar exciton transition. **a.** Electric field dependence of PL with a low excitation power of 35 μW. Peak energies have a hyperbolic dependence on the electric field. **b.** Electric field dependent PL with a high power of 1 mW. Peak energies have a linear dependence on the electric field. The laser excitation energy for both **(a)** and **(b)** is 1.696 eV. **c.** Fitted quadrupolar exciton energy shift slope of the top half branches as a function of incident power. The slope increases with the power. The dashed horizontal line is the asymptotic line slope of low power at high **E**. **d.** Normalized spectra from 8.4 mV/nm under excitation power of 35, 50, 100, 200, 280, 350, 500, 840, and 1000 μW. **e.** Extracted energies of the strongest peaks from panel **(d)**. The peak energies blue-shift under increased power. The peak energy error bar is ± 0.03 meV. The purple curve is the fitted line using a multi-exciton interaction model projected on a two-exciton basis.

Having demonstrated an interaction-induced transition from quadrupolar to dipolar excitons at finite $\mathbf{E}$, we consider the nature of the excitonic phase near $\mathbf{E} \sim 0$ and high n_{ex}. When the hybridization is overcome by many-body interactions, the degenerate layer-pseudospin recovers full SU(2) symmetry. Based on a classical electrostatic model, Ref. [134] predicts an antiferroelectric staggered phase wherein quadrupolar excitons can reduce their energy by spontaneously breaking layer pseudospin and translation symmetries at sufficiently high densities. However, it is not clear whether quantum fluctuations, which are large in 2D, destroy such long-range order. Moreover, the underlying triangular moiré lattice, if present, could frustrate the antiferroelectric state. On the other hand, fluctuating antiferroelectric correlations could develop even in the absence of long-range order. As depicted in Fig. 7.7a, the reduced overlap of electrons, due to their localization in opposite layers in the antiferroelectric configuration of dipolar excitons, suppresses the exchange interaction compared to parallel dipolar and quadrupolar excitons. Such antiferroelectric correlations alter the wavefunction of excitons and thereby modify the excitonic exchange interactions, which can be detected through many-exciton exchange-induced valley splitting [2]. Fig. 7.7b shows the valley splitting of co- and cross-polarized emission as a function of $\mathbf{E}$ under circularly polarized excitation, which creates valley-polarized excitons. Indeed, below a small $\mathbf{E}$ of $\sim$ 4 mV/nm of either polarity, we observe a reduction in exchange splitting from 2.5 meV to 0.5 meV consistent with an antiferroelectric configuration. Incidentally, PL in this $\mathbf{E}$ range displays a 'kink' where the behavior is qualitatively different, marked by suppression of red tail (see Fig.E8 in Appendix E), an effect that is not entirely clear and left for future studies.

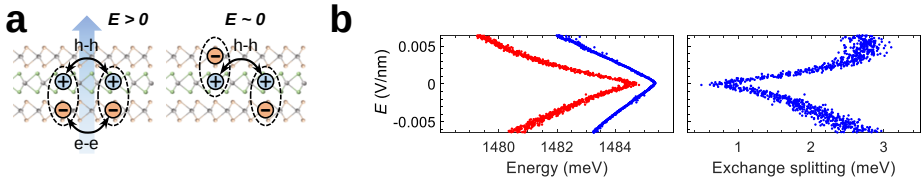

Figure 7.7: Signature of antiferroelectric ordering in electric field dependent exchange interactions. **a.** Schematics of exchange interactions at $\mathbf{E} > 0$ and $\mathbf{E} \sim 0$. Both electron-electron and hole-hole exchange interactions exist for $\mathbf{E} > 0$ whereas only hole-hole exchange interactions exist for $\mathbf{E} \sim 0$. **b.** Zoomed-in electric field dependence of co- (blue dot) and cross-polarized (red dot) strongest peak energies (left) and their energy splitting (right) at 1 mW.

7.6 Conclusion and Outlook

In conclusion, we have observed a hybridized exciton formed as symmetric coherent superposition of oppositely oriented dipolar excitons in a vdW heterotrilayer and featuring a quadrupolar moment. An external electric field can modify the wavefunction of the quadrupolar exciton wavefunction and change its dipole moment to achieve tunable light-matter interactions. The sizable oscillator strength of symmetric quadrupolar excitons allows for efficient coupling to optical cavity modes and the resulting quadrupolar polaritons can be used for electrically tunable light-matter coupling and polariton-polariton interactions [138, 127, 102]. Moreover, many-exciton interactions driven de-hybridization enables the existence of antiferroelectric correlations between excitons, paving the way for intriguing staggered excitonic lattice.

Chapter 8

Summary and Outlook

The main experimental results of this dissertation were obtained in vdW semiconductor transition metal dichalcogenides heterostructures with dual-gate control. Such a highly tunable platform can provide charge (electron/hole), spin-valley (spin-up K valley/ spin-down K' valley), and layer (top/bottom) degree of freedom. Mixing and interplay among them give rise to rich physics about interactions, which are optically detectable due to strong light-matter coupling. The fundamental optical response is determined by layer resolved electron-hole pairs – interlayer excitons (IXs), so that interactions manifested in the optical measurements can then be either exciton-exciton interactions or exciton-electron interactions. For exciton-exciton interactions, combining charge and layer degree of freedom, IXs possess static, out-of-plane dipole moment, which enables us to study spin-independent repulsive dipole-dipole interactions. Furthermore, taking into account indistinguishable spin-valley indices, we examine the spin-dependent exchange interactions between valley polarized IXs, which induce an out-of-equilibrium magnetic field. Regarding exciton-electron interactions, they provide the possibility to investigate correlated electronic states through exciton resonance and emission. We demonstrate localized IXs as sensitive optical probes for charge-order-states with $\sim$ 10 nm resolution. Finally, with additional layer degree of

freedom in a heterotrilayer, hybridized quadrupolar excitons are formed by a quantum superposition of IXs with oppositely orientated dipoles fixed by the layer indices. A transition from quadrupolar excitons to dipolar excitons is achieved by many-body interactions.

To conclude, this dissertation provides insight into interacting excitons and electrons by characterizing their optical response. Our research shows 2D TMDs as an attractive platform to study interactions because interactions inside are strongly enhanced and highly tunable compared to 3D materials. They can further couple to light, providing a non-invasive method to study and create new interacting phases of many particles. In condensed matter physics, many interactions related problems remain unexplored and require either new techniques or new material systems to be solved. I will list a few of them relevant to this dissertation and promising to be solved in 2D materials:

First, I comment on the possibility of the existence of excitonic order driven by the interactions between excitons. Whereas the existence of dipolar and exchange interactions between IXs is now well-established, there is no strong evidence for the formation of exciton lattice by spontaneous translation symmetry breaking. Although IXs are long-lived, they are still excited states in a driven-dissipative scheme, distinct from electronic ground states. If we can achieve such ordered excitons, we can use them to simulate many-body bosonic models.

Second, the artificial creation of high density programmable quantum emitter arrays: Each localized interlayer exciton is a quantum emitter, which has been proposed for quantum computation. If they are trapped by moiré potential, they form a quantum emitter triangular lattice with a high density of 10^4 μm^{-2}. However, the localized IXs in vdW heterostructures are actually not deterministically created with proper pattern. Instead, they are randomly distributed over the whole sample, possibly due to the disorder of fabrication. In order to check the origin of localized IXs, near-field

scanning probe technique is required to correlate their positions with moiré potential minima.

Third, the phase diagram of Bose-Fermi mixture at high-density limit: Excitons (bosons) and electrons (fermions) can be easily added to vdW heterostructures by optical or electrical injections. We have shown that there are interactions between them, which are promising to realize Bose–Fermi mixtures consisting of strongly interacting dense excitons and electrons, beyond what is achievable with ultracold atoms.

Last, the detection of topologically ordered states: Topologically ordered states feature long-range entanglement. For example, chiral spin liquids and fractional Chern insulators have globally entangled constituents. To prove entanglement between particles in the solid state system is challenging, because there is no rigorous protocol for how to detect the states of two distant particles at the same time. Our spatially distributed localized IXs can in principle simultaneously probe global charge and spin order, which is reconstructed from the local information acquired by separate localized IXs. Photon statistics between two distant localized IXs could contain the information of entanglement.

Of course, there are many other important and intriguing questions not listed here. Though identifying a promising research direction in physical science is not easy, I hope the results in this dissertation can be beneficial to broader areas of physics, beyond 2D materials.

Appendix A

Supplementary Information for moiré band calculation

The moiré hole bands in the Chapter 2 are calculated by solving the equation

$$\mathcal{H}(\mathbf{k})\psi_{\mathbf{k}} = \begin{pmatrix} -\frac{\hbar^2(\mathbf{k}+\mathbf{G}_i)^2}{2m^*} & V(\mathbf{G}_i - \mathbf{G}_j) \\ V^*(\mathbf{G}_i - \mathbf{G}_j) & -\frac{\hbar^2(\mathbf{k}+\mathbf{G}_j)^2}{2m^*} \end{pmatrix} \psi_{\mathbf{k}} = E_{\mathbf{k}}\psi_{\mathbf{k}} \tag{A.1}$$

where $E_{\mathbf{k}}$ is the eigenenergy and $\psi_{\mathbf{k}}$ is the eigenstate. The number of moiré reciprocal vectors $\mathbf{G}_i$ involved in the calculation decides the number of energy bands. I calculate 7 bands in Fig. 2.7b and 37 bands in both Fig. 2.9a and 2.9c. The optical absorption shown in Fig. 2.9b is calculated by projecting the eigenstate into intralayer valley K_α exciton eigenstates, which are

$$|K_+\rangle = \begin{pmatrix} 1 \\ 0 \end{pmatrix}, |K_-\rangle = \begin{pmatrix} 0 \\ 1 \end{pmatrix} \tag{A.2}$$

Above calculation gives the isolated flat band in Fig. 2.7b. On the other hand, Hubbard model with hopping t describes the topmost flat band as

$$E(\mathbf{k}) = E_0 + \left| t_1 \sum_{j=1}^{6} exp(i\mathbf{k}\cdot\mathbf{r}_{1,j}) + t_2 \sum_{j=1}^{6} exp(i\mathbf{k}\cdot\mathbf{r}_{2,j}) + t_3 \sum_{j=1}^{6} exp(i\mathbf{k}\cdot\mathbf{r}_{3,j}) \right|,$$

where $\mathbf{r}_{1,j}$, $\mathbf{r}_{2,j}$, and $\mathbf{r}_{1,j}$ are the nearest-neighbor, next nearest-neighbor, and third nearest-neighbor coordinates, respectively. Plugging the coordinates into the equation, we can get

$$\begin{aligned} E(k_x, k_y) &= E_0 + t_1[2\cos(k_y) + 2\cos(\frac{\sqrt{3}}{2}k_x - \frac{1}{2}k_y) + 2\cos(\frac{\sqrt{3}}{2}k_x + \frac{1}{2}k_y] \\ &+ t_2[2\cos(\sqrt{3}k_x) + 2\cos(\frac{\sqrt{3}}{2}k_x - \frac{3}{2}k_y) + 2\cos(\frac{\sqrt{3}}{2}k_x + \frac{3}{2}k_y)] \\ &+ t_3[2\cos(2k_y) + 2\cos(\sqrt{3}k_x - k_y) + 2\cos(\sqrt{3}k_x + k_y)]. \end{aligned} \tag{A.3}$$

The hopping t is then fitted to be the nearest-neighbor (NN) hopping t_1 = 2.57 meV, next nearest-neighbor (NNN) hopping t_2 = -0.52 meV and the third nearest-neighbor hopping t_2 = -0.27 meV.

Appendix B

Extended data for few-body interaction studies

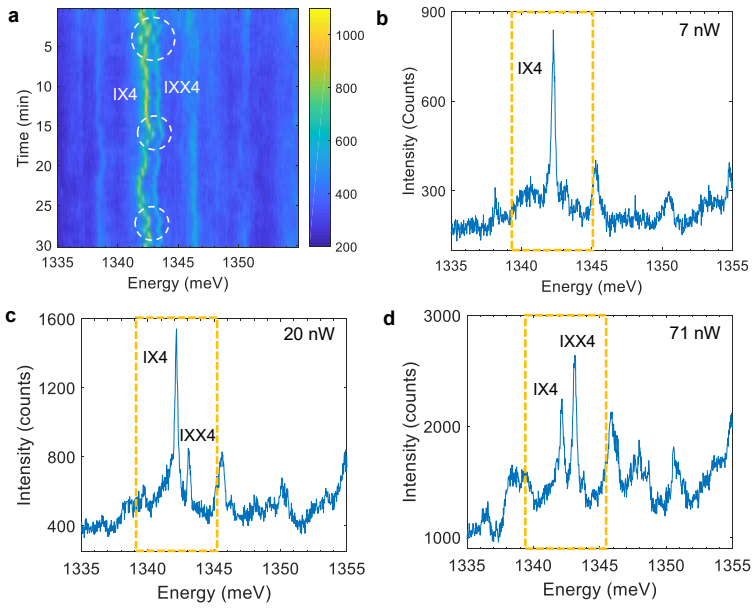

Figure B1: Localized interlayer exciton IX4 and biexciton IXX4. a, Time-trace PL emission of localized interlayer exciton IX4 and biexciton IXX4. Dashed circles highlight the same spectral jittering patterns, which implies that IX4 and IXX4 are correlated. **b-d** PL spectra of IX4-IXX4 under different excitation powers, 7 nW (b), 20 nW (c) and 71 nW (d). Only exciton IX4 appears at low power (7 nW). Biexciton IXX4 shows up at intermediate power (20 nW) and becomes stronger than IX4 at high power (71 nW). Excitation laser is linearly-polarized, with wavelength λ = 745 nm. Incident power P = 50 nW in panel **a**.

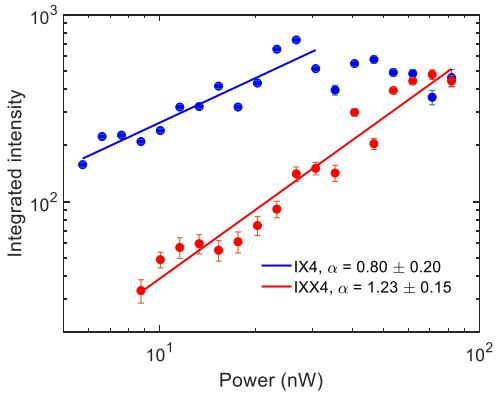

Figure B2: Power-dependent integrated intensities of localized interlayer exciton IX4 and biexciton IXX4. The fitting was done with a power law function, $I \propto P^{\alpha}$. Error bars for both extracted intensities and power-law scaling coefficients arise from fitting. Excitation is linearly-polarized, with wavelength $\lambda = 745$ nm.

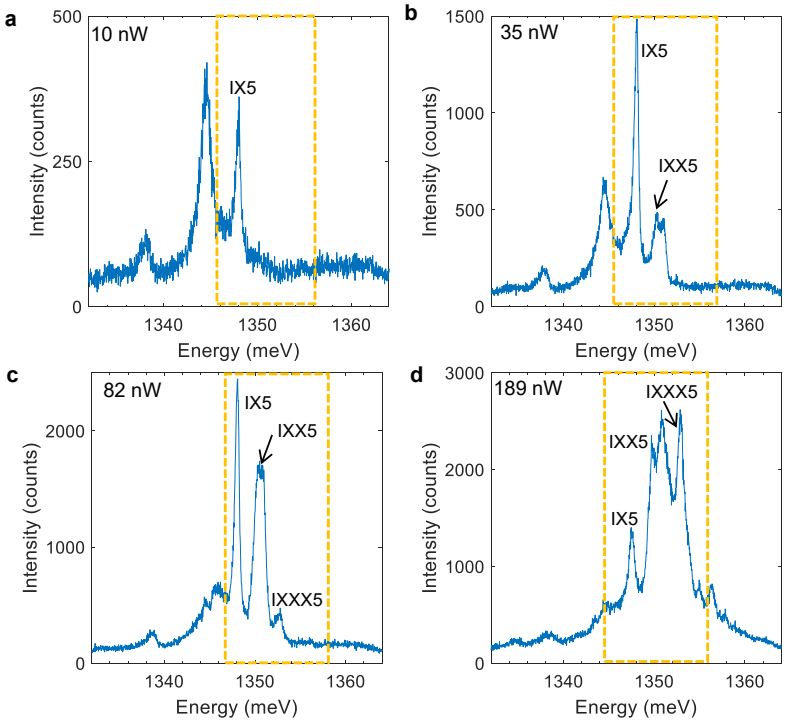

Figure B3: PL emission of IX5 group under difference excitation powers. Yellow dashed rectangles highlight the IX5 group. Only exciton IX5 shows up at low power, 10 nW(a). Biexciton IX5 starts to appear at $P = 35$ nW (b), and triexciton IXXX5 is activated at higher power 82 nW (c). At $P = 189$ nW (d), triexciton IXXX5 is stronger than biexciton IXX5, and exciton IX5 is the weakest. Excitation is linearly-polarized, with wavelength $\lambda = 745$ nm.

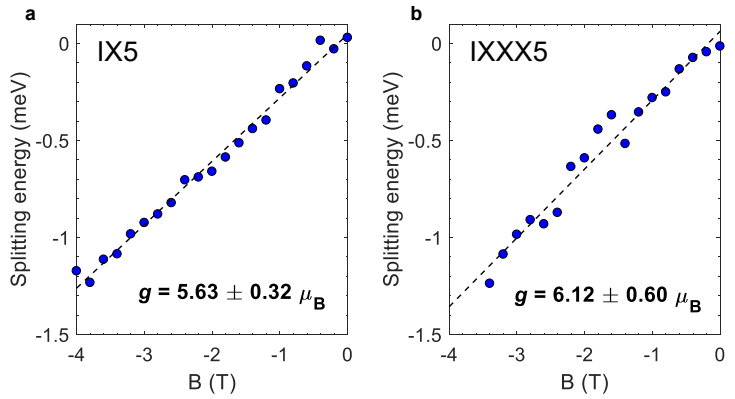

Figure B4: g-factors of localized interlayer excitons in IX5 group. Exciton IX5 (a) and triexciton IXXX5 (b) exhibit the same value of g-factor. Excitation is linearly-polarized, with wavelength $\lambda = 745$ nm. Incident power $P = 180$ nW.

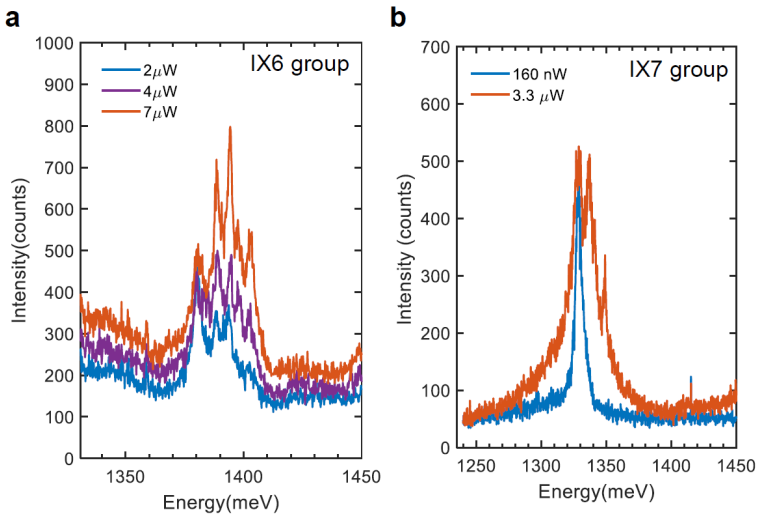

Figure B5: PL spectra of IX6 and IX7 groups under different excitation powers. The red peak, which corresponds to exciton emission, dominates at low power (**a,** $P = 2$ μW for IX6 group; **b,** $P = 160$ nW for IX7 group).With increasing excitation power, systematic appearance of peaks to the higher energy of the parent red peak appear and dominate at the highest power, which is consistent with dipolar repulsion present in multi-excitonic states. Excitation is linearly-polarized, with wavelength $\lambda = 765$ nm.

Appendix C

Extended discussions for many-body interaction studies

Note 1: Discussion of valley polarization on resonance and spin valley configuration for interlayer excitons.

As shown in the main text, interlayer excitons are resonant to WSe_2 and $MoSe_2$ exciton states (Fig. 5.5a); however, robust valley polarization is only observed at WSe_2 resonance (Fig. 5.5b), which is consistent with a former report [90]. The negligible valley polarization of interlayer excitons at $MoSe_2$ resonance may be understood based on the formation process. The difference between two resonances is consistent with the fact that monolayer $MoSe_2$ shows less valley polarization than monolayer WSe_2. In other words, carriers are more depolarized before transferring to the other layer (i.e., before forming interlayer exciton) in $MoSe_2$ resonance. Nevertheless, it can still not explain the complete lost of valley polarization on $MoSe_2$ resonance, especially resonantly excited monolayer $MoSe_2$ showing valley polarization [139].

Another possible explanation is that the carriers are depolarized during the carrier transfer process at $MoSe_2$ resonance, different from the WSe_2 resonance. According to the g factor of -13.41, the twist angle of the heterobilayer is close to 60°, i.e., AB

stacking. The valley configuration is that K (-K) valley of WSe_2 is aligned with -K (K) valley of $MoSe_2$ as shown in Fig. C1. When we pump the sample with σ^+ light at WSe_2 resonance (Fig. C1a), electrons are excited in K valley of WSe_2 and then transferred to -K valley of $MoSe_2$ via spin-conserving (spin-flip) process, forming singlet (triplet) interlayer excitons without intervalley scattering. In contrast, σ^+ excitation at $MoSe_2$ resonance requires intervalley scattering process to form the interlayer excitons, no matter for the singlet or triplet states (Fig. C1b). The intervalley scattering process at $MoSe_2$ resonance may cause valley depolarization and thus the interlayer excitons have negligible valley polarization.

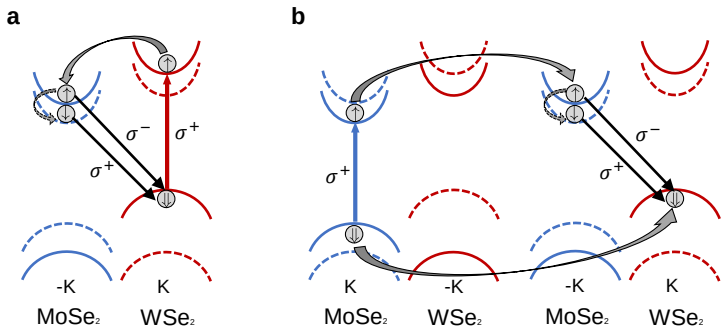

Figure C1: Interlayer exciton configurations for WSe_2 and $MoSe_2$ resonances in AB-stacking heterobilayers. a, σ^+ excitation for WSe_2 resonance. For the heterobilayer with a twist angle of 60°, K valley in the WSe_2 layer is aligned with -K valley in the $MoSe_2$ layer. When WSe_2 is excited by σ^+ light (red arrow), electrons from WSe_2 are tunneled to $MoSe_2$ via spin-conserving process (solid grey arrow) and are thermalized to lower-energy band edge (dashed grey arrow). The solid (dashed) lines in the band structures are spin up (down) states. **b,** σ^+ excitation for $MoSe_2$ resonance. Due to the time reversal symmetry, K valley in the $MoSe_2$ layer is aligned with -K valley in the WSe_2 layer. When σ^+ light excites at $MoSe_2$ resonance (blue arrow), the interlayer excitons must be formed by both spin-flipped process and intervalley scattering, which may cause valley depolarization.

Note 2. Discussion on negligible optical Stark effect at WSe_2 resonance for interlayer excitons.

Optical Stark effect (OSE) describes coherent (reversible and unitary) light-matter coupling and is important when incoherent processes (irreversible, non-unitary with

loss of information and/or energy) are less dominant [140, 141]. This coherent coupling is described by OSE when the light and matter states are off-resonance and finite detuning between the two allows for a perturbative treatment in the parameter (coupling/detuning). Following standard perturbation theory, the result is often expressed for the matter states as a dispersive shift of magnitude (coupling)^2/detuning. The strength of the coupling is given by the Rabi energy which is $\Omega = d \cdot E$ with d being the dipole matrix element between the initial and final states coupled by light, which is described classically here by its electric field E.

As for excitation in resonant with the WSe_2 transition, OSE is considered for the interlayer exciton such that the detuning (300 meV) is between the WSe_2 energy at 1.7 eV and IX emission energy at 1.4 eV. Next, we estimate Ω given our excitation intensity (I) of up to 10 μW/μm^2 and d for IX transition. Ω scales as $\sqrt{I}$, and we could simply compare our intensity to that of previous report [141] which reported OSE in WS_2. d for IX can be estimated to be that for WS_2 which can only be an overestimation. We find that our laser intensities are 6-7 orders of magnitude smaller and hence our Ω is more than 3 orders of magnitude smaller than their value of 87 meV. Thus, the expected OSE in our case will be less than $(0.0872)^2/300 \sim 25$ neV which is negligibly small compared to incoherent process with energy scale of a few meV (estimated from linewidth). In other words, as far OSE of interlayer exciton is concerned, the coherent coupling is negligible.

Another coherent effect that can be excluded in our system is the dressed state. We can consider the case when the light and matter states are in resonance. Such a situation is described (semi-classically) by considering the so-called dressed picture or "Floquet" dressed picture. At resonance, when detuning is zero, the light-matter coupling is simply the Rabi frequency Ω which in our case is less than 0.087 meV. In other words, the original states will be shifted (due to "dressing") by an amount which is much smaller than their linewidth (arising from incoherent processes) and

once again, any coherent effects can be safely ignored.

To put it simply, we are in extreme incoherent limit precisely because a large number of interlayer excitons are created when pumped at WSe_2 resonance. This generation of IX is fundamentally incoherent as it is an irreversible process - IX excitons do not get converted back to WSe_2 excitons - and takes place on a timescale (50-100 fs) due to efficient charge transfer in type-II vdW heterostructures. This timescale is orders of magnitude faster than the timescale of coherent processes ($\sim$ 100 ps for resonance and >100 ns for OSE).

Note 3: Estimation of the exciton-exciton annihilation rate from the power dependent integrated intensity.

Saturation of the power dependent integrated intensities is an important factor to consider, as it may account for the saturated splitting at high power. Two kinds of possible mechanisms are discussed here, exciton-exciton annihilation (EEA) and absorption saturation. The EEA is mainly non-radiative Auger recombination, which has been observed in various transition metal dichalcogenide monolayers [142, 143, 144, 145, 146, 147]. This process has the probability of kn^2, where k is the Auger coefficient and n is the exciton density. Therefore, the rate equation for EEA under continuous wave excitation is given by,

$$\frac{dn}{dt} = -\frac{n}{\tau} - kn^2 + g.$$

Here τ is the lifetime and g is the exciton generation rate scaled as bP_{exc}, where P_{exc} is the excitation power and b is the generation efficiency. Solving the equation for the steady state, the PL intensity is equal to $I(P_{exc}) = c_E A\frac{n}{\tau} = c_E A\frac{\sqrt{(\frac{1}{\tau})^2+4kbP_{exc}}-\frac{1}{\tau}}{2k\tau}$. $c_E = 6.8\times10^{-6}$ is the effective collection efficiency, and A is the laser spot size (1 μm^2) for our measurements. Considering the absorption to be 40%, the scaling factor $b = 1.45\times 10^{20}\mu J^{-1}\text{cm}^{-2}$ in the fitting curve presented in Fig. C2a and C2b. Fitting parameters $k = 5.5\times 10^{-4}$ cm^2/s and $\tau = 10$ ns. Both the linear scale (Fig. C2a)

and logarithmic scale (Fig. C2b) show the quantitative match between the fitting and experimental data.

Next, we discuss the absorption saturation mechanism [40]. For the resonant excitation, the absorption is proportional to $1/(1+P_{exc}/P_s)$, where P_s is the saturation power. Therefore, the rate equation becomes,

$$\frac{dn}{dt} = -\frac{n}{\tau} + g.$$

g is proportional to $\alpha P_{exc}/(1+P_{exc}/P_s)$ and α is the linear absorption (11.5%). Making $\frac{dn}{dt} = 0$, the steady-state PL intensity is

$$I(P_{exc}) = \frac{c_A}{h\nu}\frac{\alpha P_{exc}}{1 + P_{exc}/Ps}.$$

Here c_A is the collection efficiency for the absorption saturation model and $h\nu$ is the photon energy (1.72 eV). Using this formula, the fitting results are shown in Fig. C2c, C2d with $\alpha = 11.5\%$, $c_A = 6.8\times10^{-6}$, $Ps = 6.3$ μW. Although the linear scale fitting matches well, the logarithmic scale fitting shows that the absorption saturation model deviates from the experimental results in the low power regime, implying that the absorption saturation is not the mechanism for saturation behavior in the experiment.

Comparing these two mechanisms, the exciton-exciton annihilation is a more possible explanation for the saturation behavior. It is consistent with previous report that EEA is negligible in TMD heterobilayers with an exciton density lower than 5×10^{11} cm^{-2}[148]. A low EEA rate also indicates that optical doping is negligible in our experiments. As Fig. C3a, C3b shows, we did not observe any change in $MoSe_2$ absorption feature with the pump laser on versus off. In addition, we can conclude that our sample does not have enough free charge carriers to form exciton-polaron. We remark that we do observe a blueshift which is expected to arise from phase filling effect [70]. As shown in Fig. C3c, we find that there is no change in the reflection

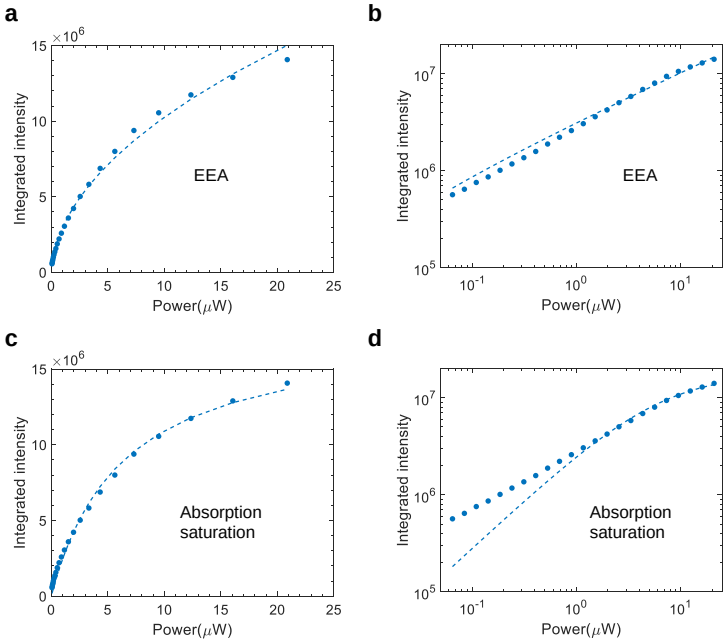

Figure C2: Calculated power dependence of the integrated intensity. a, b, Experimental data (blue circles) and fitting (blue dashed lines) using the exciton-exciton annihilation (EEA) model in the linear scale (a) and logarithmic scale (b). **c, d,** Experimental data (blue circles) and fitting (blue dashed lines) using the absorption saturation model in the linear scale (c) and logarithmic scale (d). The logarithmic scale shows that the EEA model fits better than the absorption saturation model, implying the saturation behavior is probably from the EEA process.

spectra for linear and circular excitation at 1.72 eV, suggesting that the phase filling is valley independent and the splitting is unobservable for intralayer excitons in our system.

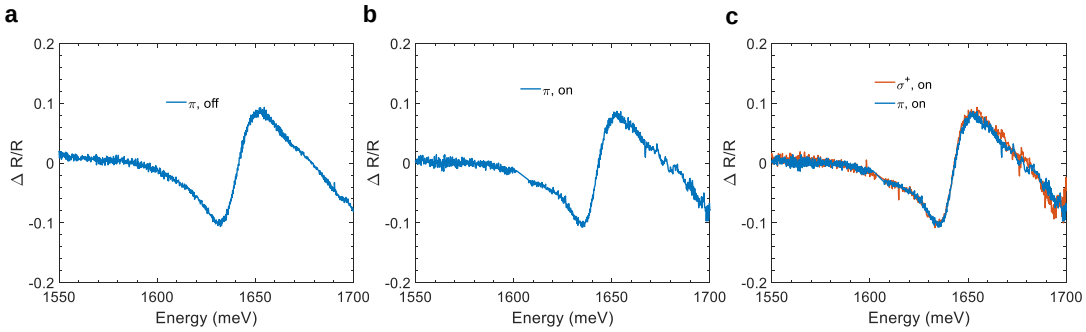

Figure C3: Reflectance contrast spectra of $MoSe_2$ resonance in $WSe_2/MoSe_2$ heterobilayer. a, b, Reflectance contrast for pump laser off (a) and on (b) for linear excitation (π). No obvious change of reflectance contrast except for a 2 meV blueshift from the phase filling. **c,** Reflectance contrast for linear (π) and circular excitation (σ^+). The polarization independent reflectance contrast indicates the phase filling is a valley independent effect in our system. The pump laser is at 1.72 eV and 5 μW.

Appendix D

Extended data for quantum sensing

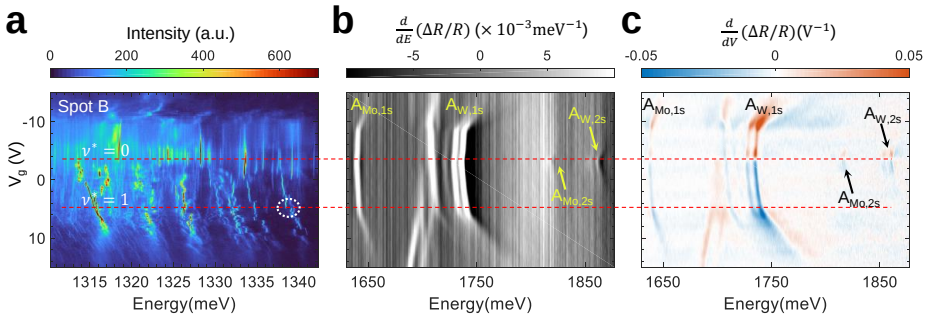

Figure D1: Correlation between doping-dependent PL (a) and reflectance contrast spectra (b, c) for Spot B. $A_{Mo,1s}$, $A_{W,1s}$, $A_{Mo,2s}$ and $A_{W,2s}$ are the $MoSe_2$ and WSe_2 intralayer 1s and 2s exciton resonances, respectively. The first red dashed line, which is at the charge neutral point, is assigned as $\nu^* = 0$. The second red dashed line, where the reflectance shows a kink and localized IX PL shows a blueshift (white dashed circle), is assigned as $\nu^* = 1$.

Exchange Hamiltonian for moiré trions

The valley mixing process for moiré trions includes the valley flip of exciton by the electron-hole exchange interaction J_{eh}, and valley-conserving resonant tunneling t of both an electron occupying a nearby moiré site and the trion electron. δ is the difference in energy of the electron occupying the moiré site and that in the trion, including interactions. The Hamiltonian of the process is $\mathcal{H} = J_{eh}t^2/\delta^2 \left(\hat{X}^+_{-K}\hat{c}^+_{-K}\,\hat{c}_K\hat{X}_K + h.c.\right)$

where $\hat{X}_K = \hat{e}_{-K}\,\hat{e}_K\hat{h}_K$ is the annihilation operator for the K-valley trion with the annihilation of K-valley exciton $\hat{e}_K\hat{h}_K$ and -K-valley trion electron $\hat{e}_{-K}$. $\hat{c}_K$ is the annihilation operator for the electron in the moiré site. The amplitude of the process is $J_{eh}t^2/\delta^2$, which depends on both t and δ. If the detuning δ is close to zero, the effect is enhanced to reduce the DCP of trion. The net effect of this process is a spin flip-flop process between the moiré electron and the trion hole.

Correction for the doping dependence after subjecting to high voltage

Though the gate dependence range of Device 1 was permanently changed after applying V_g = 40 V to the sample, the spectral jump dynamics remain the same as shown in Fig. D2. Mapping the voltage before the 40 V gate scan (Fig. D2a) to the voltage after the 40 V gate scan (Fig. D2b) for each spectral jump, the replotted gate scan after 40 V scan (Fig. D2c) is almost the same as before. Fig. D2e to g have different scan ranges after the 40 V scan but also show the same energy shifts at similar voltages. Therefore, we conclude that the application of 40 V changed the gate instead of sample properties, or in other words, the electronic crystal states are unchanged. For the assignment of filling fraction to particular jumps throughout the work, we use the data before 40 V scan.

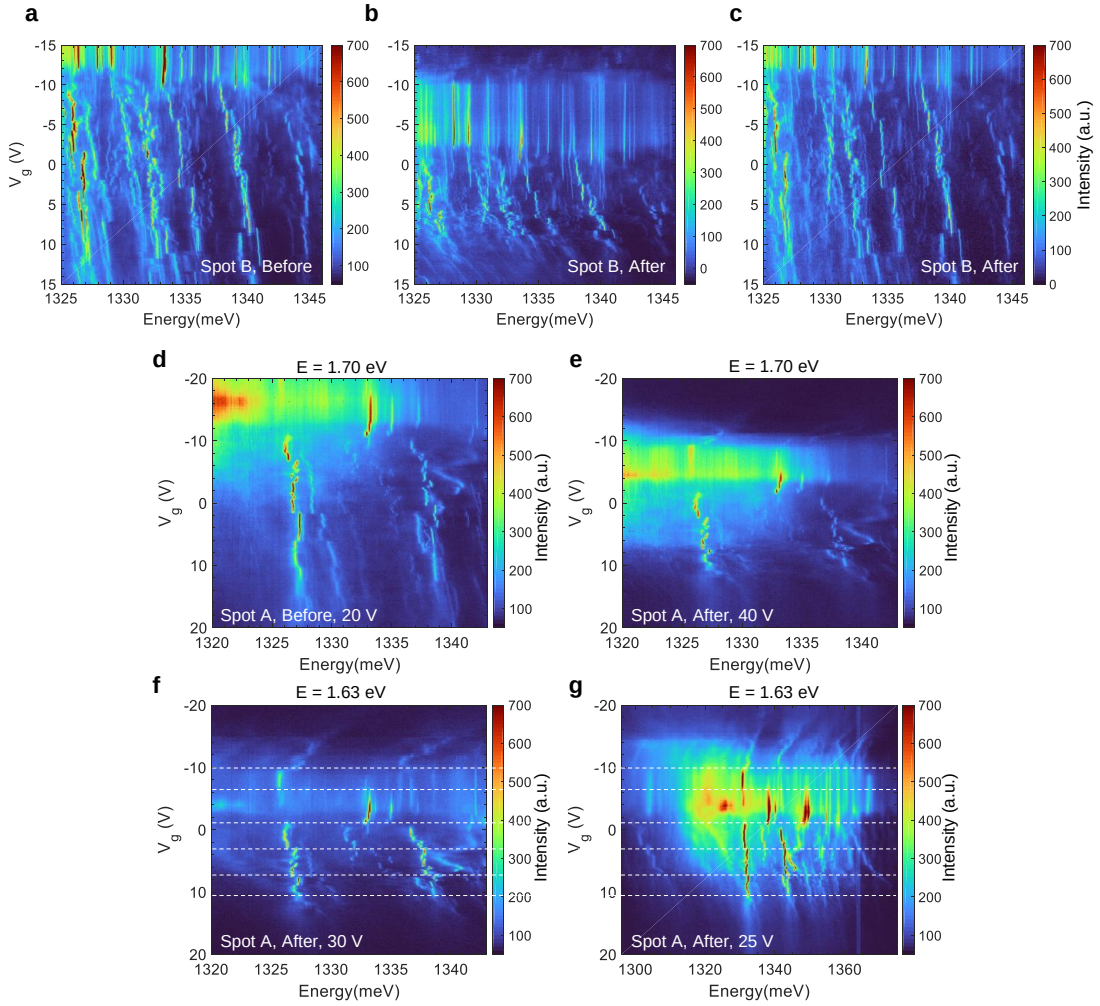

Figure D2: Correction for the gate dependence after high voltage scan. a. Gate dependence at spot B before applying 40 V to the sample. **b.** Gate dependence at spot B after applying 40 V to the sample. The charge neutral point is shifted and voltage range for electron doping is smaller compared to before. **c.** Reconstructed gate dependence from (**b**) via one-to-one mapping between voltages for spectral jumps in (**a**) and (**b**). For further details, see Methods. Gate dependence at spot A before applying 40 V (**d**) and after applying 40 V to the sample (**e-g**). The voltage scan range is +/- 20 V (**d**), +/- 40 V (**e**), +/- 30 V (**f**), +/- 25 V (**g**), respectively. Similar energy shifts occur in (**f**) and (**g**) at the white dashed lines. The excitation laser is at 1.70 eV (WSe_2 resonance) and 70 nW for (**d**)(**e**) while it is at 1.63 eV ($MoSe_2$ resonance) and 100 nW for (**f**)(**g**). The spectral resolution is 1200 grooves/mm for (**d-f**) and 300 grooves/mm for (**g**).

Appendix E

Extended data for quadrupolar excitons

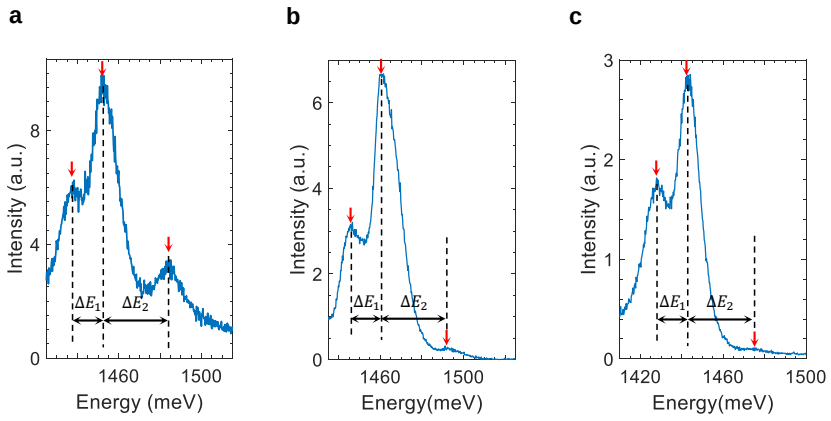

Figure E1. Robust three-peak structure in AA stacked samples. a. PL spectrum of quadrupolar excitons at another position in Device 1 at $\mathbf{E} = 0$. **b.** PL spectrum of quadrupolar excitons in Device 2 at $\mathbf{E} = 0$. **c.** PL spectrum of quadrupolar excitons in Device 5 at $V_{bg} = 2$ V, $V_{tg} = 4.4$ V. Both show three peak structures with $\Delta E_1 \sim 15$ meV and $\Delta E_2 \sim 30$ meV.

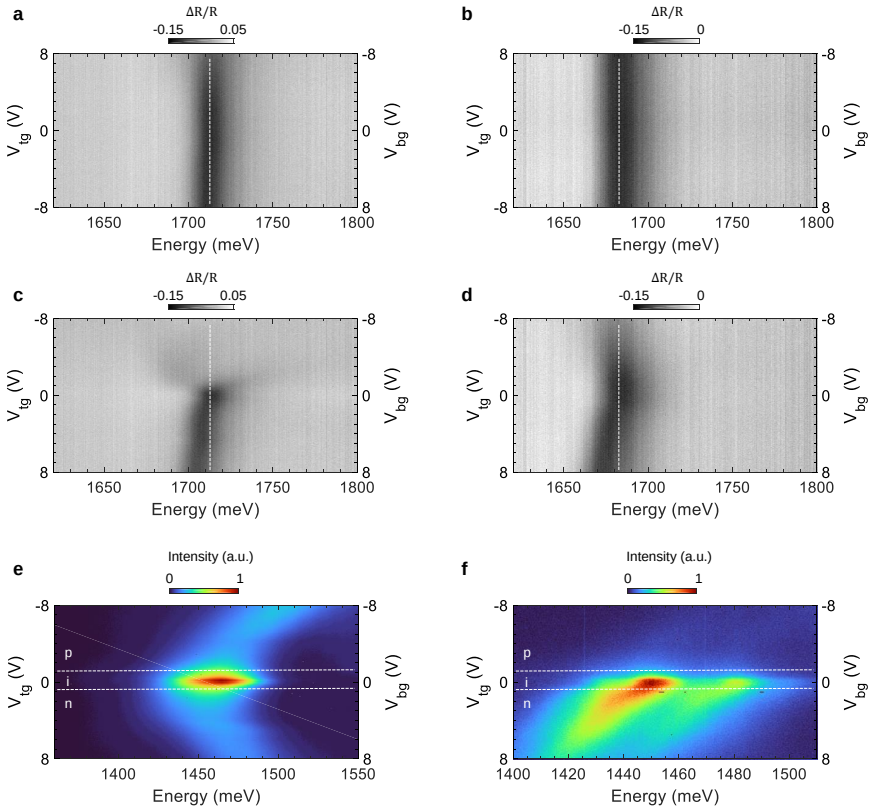

Figure E2. Reflectance and photoluminescence spectra under electric field and doping configurations in Device 1. a, b. Electric field dependent reflectance contrast spectra of the bilayer **(a)** and trilayer **(b)**. **c, d.** Doping dependent reflectance contrast spectra on the bilayer **(c)** and trilayer **(d)**. **e, f.** Doping dependent PL spectra on the bilayer **(c)** and trilayer **(d)**. The vertical white dashed lines indicate the exciton resonance has negligible change with the electric field, while the doped charges make the resonance red shifted and weaker. This confirms the electric field gate configuration is almost charge neutral. In the charge neutral region (i) of PL spectra, the energy shifts are negligible.

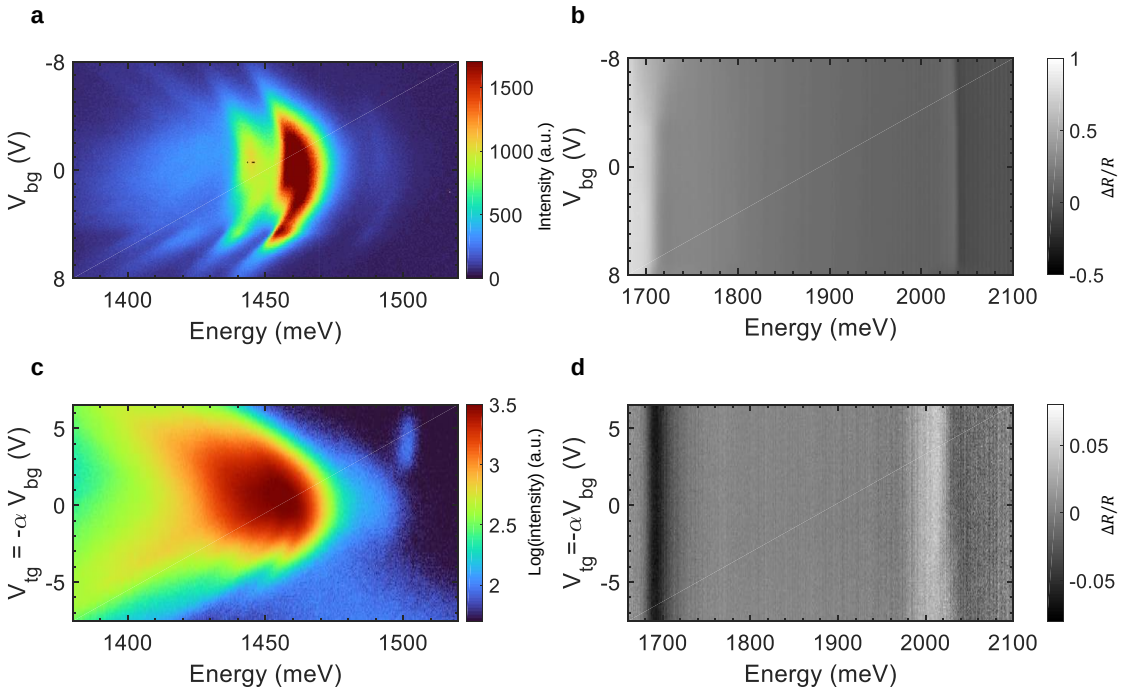

Figure E3. Gate dependence of reflectance and photoluminescence spectra in Devices 2 and 5. Device 2 and 5 both are AA stacked sample with 0° twist angle between the top and bottom WS_2 monolayers. The gate dependent PL of the trilayer in Device 2 **(a)** and Device 5 **(c)** show only red shifts with opposite electric field, i.e., "C"-shape, similar to Figure. 2b from the Device 1 in the main text. The gate dependent reflectance contrast spectra of Device 2 **(b)** and Device 5 **(d)** suggest the "C"-shape dependence is not from doping. α is 0.7 for the electric field configuration. The excitation energies are 1.72 and 1.69 eV for panel **(a)** and **(c)**, respectively.

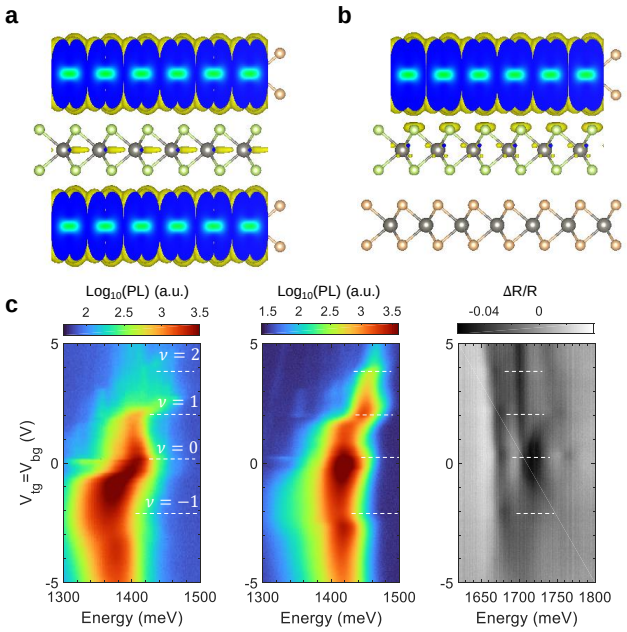

Figure E4. DFT calculated charge distribution in different trilayer configurations. a. Charge distribution in outer two WS_2 layer AA stacked sample at zero electric field. **b.** Charge distribution in outer two WS_2 layer AB stacked sample. **c.** Doping dependent PL spectra in the outer layer AB trilayer (left) and bilayer regions (middle) and corresponding reflectance contrast in the bilayer region (right). Sudden changes in PL and reflectance indicate the presence of correlated electronic states in the bilayer region [113, 114].

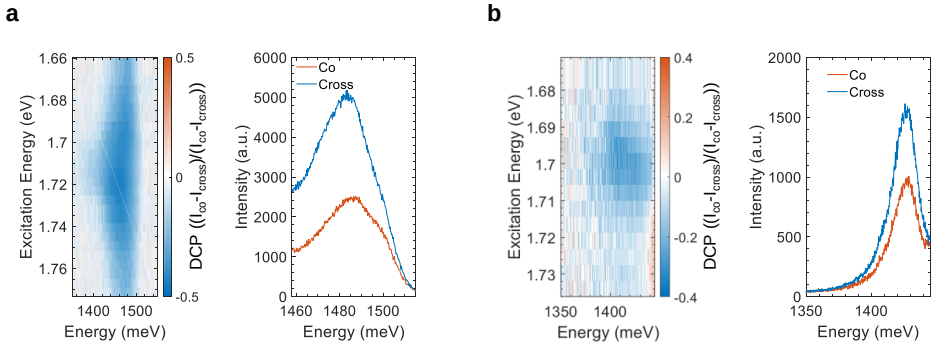

Figure E5. Polarization-resolved photoluminescence excitation spectra for dipolar excitons. The dipolar exciton emissions from Device 1 **(a)** and Device 2 **(a)** bilayer regions are cross-polarized, which is consistent with 60° twist angle WSe_2/WS_2 [113, 80]. The spectra on the right are excited at 1.70 eV.

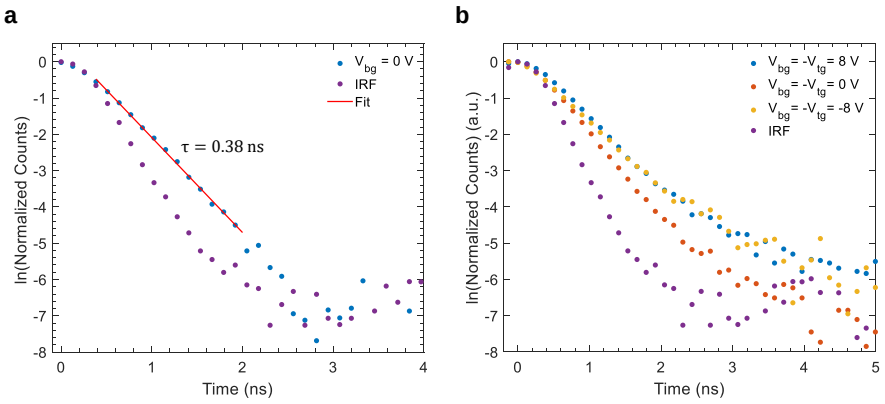

Figure E6. Lifetime measurements of quadrupolar excitons. a. Lifetime of the quadrupolar excitons in Device 2 at zero gate voltage. The fitted lifetime is 0.38±0.02 ns. **b.** Electrical control of quadrupolar exciton lifetime in Device 1. The fitted lifetime at V_{bg} = 8, 0, -8 V is 0.53, 0.43, 0.55 with an error bar of ±0.02 ns, respectively. Both directions of the electric field increase the lifetime of the quadrupolar exciton. All the lifetime measurements are above the IRF of 0.27±0.02 ns.

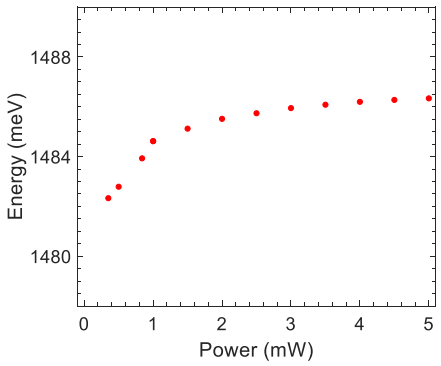

Figure E7. Energy shifts of quadrupolar excitons at higher power and zero electric field.

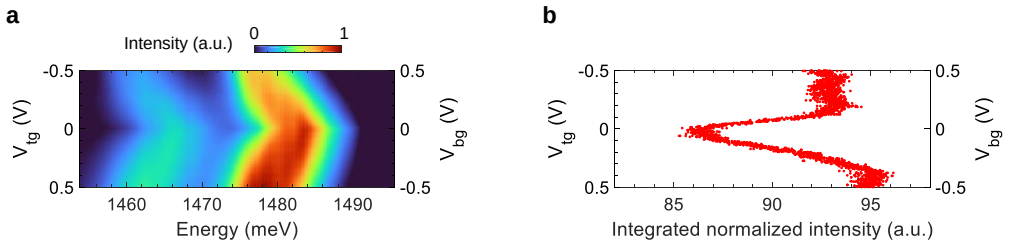

Figure E8. Zero electric field states for trilayer excitons. a. Electric field dependence of trilayer exciton PL emission at 1 mW with fine voltage steps. The PL emission shows an absent red tail around zero field. **b.** Integrated red tail intensity of the normalized spectra in panel **(a)** shows a dip near zero field. The excitation is linearly-polarized.

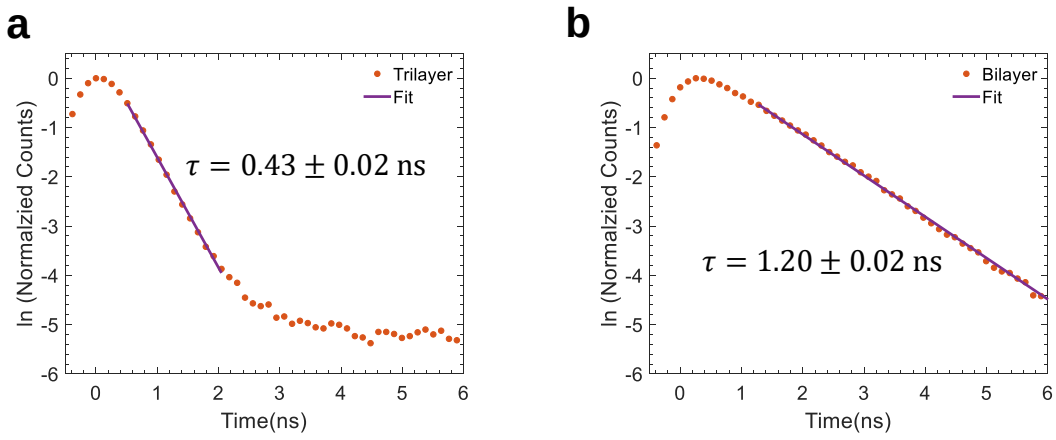

Figure E9. Trilayer and bilayer exciton lifetime comparison in Device 1.

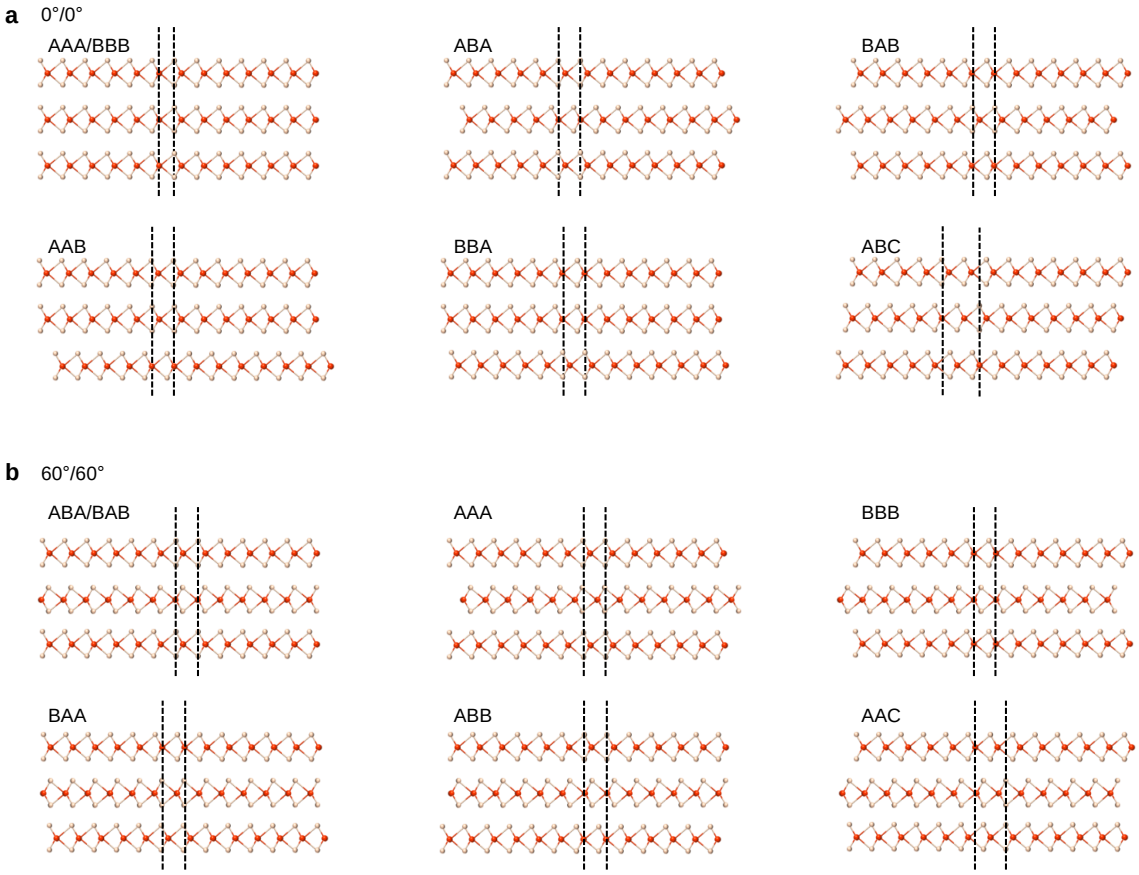

Figure E10. Stacking configurations for AA stacked samples. a. Stacking configurations for 0° twist angle both between top and middle layers and between middle and bottom layers (0° /0°). **b.** Stacking configurations for 60° twist angle both between top and middle layers and between middle and bottom layers (60° /60°). A is the chalcogenide atoms (S or Se) and B is the transition metal atom W. The black dashed lines indicate the aligned atoms.

Figure E11. DFT calculation of electron distribution for AA stacked samples. a. Electron distribution in 0°/0° samples. **b.** Electron distribution in 60°/60° samples. The red highlighted ABA in 0°/0° and ABA/BAB in 60°/60° are the lowest energy states.

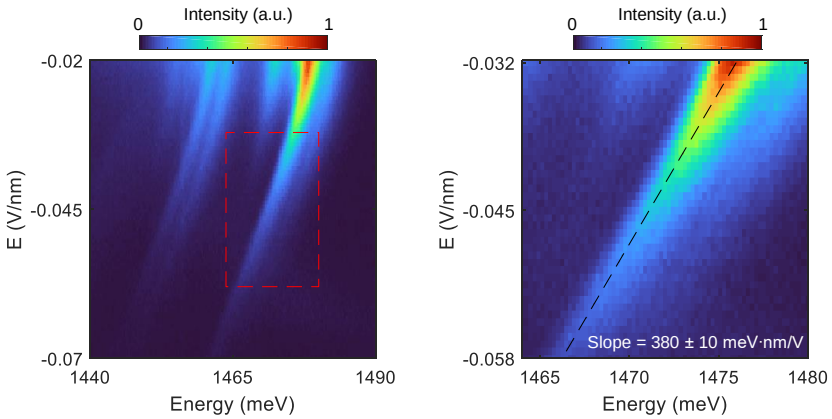

Figure E12. Extraction of the quadrupolar exciton PL energy slope at low power and high E-field. The left panel shows the PL of trilayer excitons under 35 uW excitation of 1.696 eV laser. The red dashed line shows the region where the slope becomes saturated. The region under the dashed line is shown in the right panel, as well as the linear fit of the saturated dipole moment. This value is shown in Fig. 4c as the black dashed line.

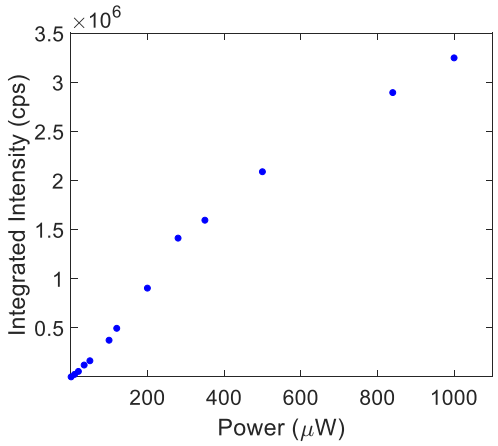

Figure E13. The power dependence of the integrated intensity of trilayer emission. The integrated intensity has a linear dependence on the excitation power up to 1 mW, which implies no saturation induced heating or photo-doping.

Note 1. Discussion on the possible trilayer configurations hosting quadrupolar excitons.

The trilayer configurations can be sorted into two cases, depending on the twist angle between the top and bottom WS_2 monolayers, that is, 0° (AA, Device 1, 2, 4, 5) and 60° (AB, Device 3). As shown in Fig. E4a, b, for a AA stacked trilayer, the DFT calculations show electrons has hybridization and finite weight in the middle, whereas the electrons in a AB stacked trilayer tend to localize at one WS_2 layer due to the broken mirror symmetry. This explains no hybridization and one dipole emission being much stronger than the other dipole emission in the AB stacked sample as shown in main Fig. 7.4g. Another evidence for no hybridization in the AB stacked sample is the trilayer has similar correlated electronic states as the bilayer (Fig. E4c). In other words, the AB stacked trilayer is decoupled and functions as a bilayer.

Next, we further discuss the moiré registry of AA stacked samples. As we have zero-degree twist angle between top and bottom WS_2 layers for hybridized electrons, we can have two sets of configurations depending on the middle layer WSe_2 alignment. One is 0° relative twist angle between WSe_2/WS_2(0°/0°), and the other one is 60° relative twist angle between WSe_2/WS_2 layer (60°/60°). All the configurations are shown in Fig. E10, with atom alignments highlighted by black dashed lines. For 0°/0° configurations, there are three configurations with mirror symmetry (AAA/BBB, ABA, BAB), and three configurations without mirror symmetry (AAB, BBA, ABC) where A is the chalcogenide atoms (S or Se) and B is the transition metal atom W. ABC is when top S atom is aligned with middle W atom while the middle Se atom is aligned with bottom W atom. For 60°/60° configurations, there are three configurations with mirror symmetry (ABA/BAB, AAA, BBB), and three configurations without mirror symmetry (BAA, ABB, AAC). AAC is when the top W atom is aligned with the middle W atom while the middle Se atom is aligned with the bottom S atom. It should be noted that we ignore the mirror images of asymmetric cases because they

have the same properties.

We calculated the electron distributions for all the above cases using DFT calculations as shown in Fig. E11. We can conclude that only electron distributions in the configurations with mirror symmetry will be symmetric and the hybridization (electron weight in the middle layer) is different for different symmetric structures. According to a previous report[119], for 0°/0° case, ABA (red highlighted) will be the lowest energy registry, 100 meV lower than AAA/BBB, while for 60°/60° case, ABA/BAB (red highlighted) will be the lowest energy registry. Based on cross-polarized emission (Fig. E5)[113, 80] and g factor of 14 in our bilayer WSe_2/WS_2 [149], we can conclude that 60°/60° is the configuration of our AA stacked trilayer with quadrupolar excitons, where the electron weight in the middle is larger than that in the 0°/0° sample. This is the reason why we only present DFT simulations (including E-field dependence) in Fig. 7.4 for ABA/BAB structure.

References

[1] Li, W., Lu, X., Dubey, S., Devenica, L. & Srivastava, A. Dipolar interactions between localized interlayer excitons in van der waals heterostructures. *Nature Materials* **19**, 624–629 (2020).

[2] Li, W., Lu, X., Wu, J. & Srivastava, A. Optical control of the valley zeeman effect through many-exciton interactions. *Nature Nanotechnology* **16**, 148–152 (2021).

[3] Li, W. *et al.* Local sensing of correlated electrons in dual-moiré heterostructures using dipolar excitons. *arXiv preprint arXiv:2111.09440* (2021).

[4] Li, W. *et al.* Quadrupolar excitons in a tunnel-coupled van der waals heterotrilayer. *arXiv preprint arXiv:2208.05490* (2022).

[5] Zhang, C. *et al.* Systematic study of electronic structure and band alignment of monolayer transition metal dichalcogenides in van der waals heterostructures. *2D Materials* **4**, 015026 (2016).

[6] Bistritzer, R. & MacDonald, A. H. Moiré bands in twisted double-layer graphene. *Proceedings of the National Academy of Sciences* **108**, 12233–12237 (2011).

[7] Cao, Y. *et al.* Unconventional superconductivity in magic-angle graphene superlattices. *Nature* **556**, 43 EP – (2018). URL `https://doi.org/10.1038/nature26160`.

[8] Cao, Y. *et al.* Correlated insulator behaviour at half-filling in magic-angle graphene superlattices. *Nature* **556**, 80 EP – (2018). URL `https://doi.org/10.1038/nature26154`.

[9] Manzeli, S., Ovchinnikov, D., Pasquier, D., Yazyev, O. V. & Kis, A. 2d transition metal dichalcogenides. *Nature Reviews Materials* **2**, 1–15 (2017).

[10] Li, R., Cheng, Y. & Huang, W. Recent progress of janus 2d transition metal chalcogenides: from theory to experiments. *Small* **14**, 1802091 (2018).

[11] Liu, G.-B., Shan, W.-Y., Yao, Y., Yao, W. & Xiao, D. Three-band tight-binding model for monolayers of group-vib transition metal dichalcogenides. *Phys. Rev. B* **88**, 085433 (2013). URL `http://link.aps.org/doi/10.1103/PhysRevB.88.085433`.

[12] Dresselhaus, G. Spin-orbit coupling effects in zinc blende structures. *Physical Review* **100**, 580 (1955).

[13] Bychkov, Y. A. & Rashba, É. I. Properties of a 2d electron gas with lifted spectral degeneracy. *JETP lett* **39**, 78 (1984).

[14] Xiao, D., Liu, G.-B., Feng, W., Xu, X. & Yao, W. Coupled spin and valley physics in monolayers of mos_2 and other group-vi dichalcogenides. *Phys. Rev. Lett.* **108**, 196802 (2012). URL `http://link.aps.org/doi/10.1103/PhysRevLett.108.196802`.

[15] Xiao, D., Chang, M.-C. & Niu, Q. Berry phase effects on electronic properties. *Rev. Mod. Phys.* **82**, 1959–2007 (2010). URL `http://link.aps.org/doi/10.1103/RevModPhys.82.1959`.

[16] Xu, X., Yao, W., Xiao, D. & Heinz, T. F. Spin and pseudospins in layered transition metal dichalcogenides. *Nat Phys* **10**, 343–350 (2014). URL `http://dx.doi.org/10.1038/nphys2942`.

[17] Zhang, X., Shan, W.-Y. & Xiao, D. Optical selection rule of excitons in gapped chiral fermion systems. *Physical review letters* **120**, 077401 (2018).

[18] He, K. *et al.* Tightly bound excitons in monolayer wse_2. *Phys. Rev. Lett.* **113**, 026803 (2014). URL http://link.aps.org/doi/10.1103/PhysRevLett.113.026803.

[19] Chernikov, A. *et al.* Exciton binding energy and nonhydrogenic rydberg series in monolayer ws_2. *Phys. Rev. Lett.* **113**, 076802 (2014). URL http://link.aps.org/doi/10.1103/PhysRevLett.113.076802.

[20] Sidler, M. *et al.* Fermi polaron-polaritons in charge-tunable atomically thin semiconductors. *Nat. Phys.* **13**, 255–261 (2016). URL http://dx.doi.org/10.1038/nphys3949.

[21] Liu, X. *et al.* Strong light–matter coupling in two-dimensional atomic crystals. *Nature Photonics* **9**, 30–34 (2015).

[22] Dufferwiel, S. *et al.* Exciton–polaritons in van der waals heterostructures embedded in tunable microcavities. *Nature communications* **6**, 8579 (2015).

[23] Zhang, L., Gogna, R., Burg, W., Tutuc, E. & Deng, H. Photonic-crystal exciton-polaritons in monolayer semiconductors. *Nature communications* **9**, 713 (2018).

[24] Srivastava, A. *et al.* Valley zeeman effect in elementary optical excitations of monolayer wse_2. *Nat Phys* **11**, 141–147 (2015). URL http://dx.doi.org/10.1038/nphys3203.

[25] Aivazian, G. *et al.* Magnetic control of valley pseudospin in monolayer wse_2. *Nat Phys* **11**, 148–152 (2015). URL http://dx.doi.org/10.1038/nphys3201.

[26] MacNeill, D. *et al.* Breaking of valley degeneracy by magnetic field in monolayer $mose_2$. *Phys. Rev. Lett.* **114**, 037401 (2015). URL http://link.aps.org/doi/10.1103/PhysRevLett.114.037401.

[27] Li, Y. *et al.* Valley splitting and polarization by the zeeman effect in monolayer $mose_2$. *Phys. Rev. Lett.* **113**, 266804 (2014). URL `http://link.aps.org/doi/10.1103/PhysRevLett.113.266804`.

[28] Srivastava, A. *et al.* Optically active quantum dots in monolayer wse_2. *Nature Nanotechnology* **10**, 491–496 (2015). URL `http://dx.doi.org/10.1038/nnano.2015.60`.

[29] He, Y.-M. *et al.* Single quantum emitters in monolayer semiconductors. *Nature Nanotechnology* **10**, 497–502 (2015). URL `http://dx.doi.org/10.1038/nnano.2015.75`.

[30] Jin, C. *et al.* Observation of moiré excitons in wse_2/ws_2 heterostructure superlattices. *Nature* **567**, 76–80 (2019). URL `https://doi.org/10.1038/s41586-019-0976-y`.

[31] Seyler, K. L. *et al.* Signatures of moiré-trapped valley excitons in $mose_2/wse_2$ heterobilayers. *Nature* **567**, 66 (2019).

[32] Tran, K. *et al.* Evidence for moiré excitons in van der waals heterostructures. *Nature* **567**, 71–75 (2019).

[33] Alexeev, E. M. *et al.* Resonantly hybridized excitons in moiré superlattices in van der waals heterostructures. *Nature* **567**, 81–86 (2019). URL `https://doi.org/10.1038/s41586-019-0986-9`.

[34] Tang, Y. *et al.* Simulation of hubbard model physics in wse_2/ws_2 moiré superlattices. *Nature* **579**, 353–358 (2020).

[35] Xu, Y. *et al.* Correlated insulating states at fractional fillings of moiré superlattices. *Nature* **587**, 214–218 (2020).

[36] Li, T. *et al.* Continuous mott transition in semiconductor moiré superlattices. *Nature* **597**, 350–354 (2021).

[37] Li, T. *et al.* Quantum anomalous hall effect from intertwined moiré bands. *Nature* **600**, 641–646 (2021).

[38] Li, H. *et al.* Imaging two-dimensional generalized wigner crystals. *Nature* **597**, 650–654 (2021).

[39] Shimazaki, Y. *et al.* Strongly correlated electrons and hybrid excitons in a moiré heterostructure. *Nature* **580**, 472–477 (2020).

[40] Rivera, P. *et al.* Observation of long-lived interlayer excitons in monolayer $mose_2$–wse_2 heterostructures. *Nature Communications* **6**, 6242 EP – (2015). URL `http://dx.doi.org/10.1038/ncomms7242`.

[41] Rivera, P. *et al.* Valley-polarized exciton dynamics in a 2d semiconductor heterostructure. *Science* **351**, 688–691 (2016). URL `http://science.sciencemag.org/content/351/6274/688`. `http://science.sciencemag.org/content/351/6274/688.full.pdf`.

[42] Jauregui, L. A. *et al.* Electrical control of interlayer exciton dynamics in atomically thin heterostructures. *Science* **366**, 870–875 (2019).

[43] Ciarrocchi, A. *et al.* Polarization switching and electrical control of interlayer excitons in two-dimensional van der waals heterostructures. *Nature photonics* **13**, 131–136 (2019).

[44] Unuchek, D. *et al.* Room-temperature electrical control of exciton flux in a van der waals heterostructure. *Nature* **560**, 340–344 (2018).

[45] Hong, X. *et al.* Ultrafast charge transfer in atomically thin mos_2/ws_2 heterostructures. *Nature nanotechnology* **9**, 682 (2014).

[46] Jin, C. *et al.* Imaging of pure spin-valley diffusion current in ws_2-wse_2 heterostructures. *Science* **360**, 893–896 (2018).

[47] Seyler, K. L. *et al.* Valley manipulation by optically tuning the magnetic proximity effect in wse_2/cri3 heterostructures. *Nano letters* **18**, 3823–3828 (2018).

[48] Ciorciaro, L., Kroner, M., Watanabe, K., Taniguchi, T. & Imamoglu, A. Observation of magnetic proximity effect using resonant optical spectroscopy of an electrically tunable $mose_2$/crbr 3 heterostructure. *Physical Review Letters* **124**, 197401 (2020).

[49] Kang, K. *et al.* Switchable moiré potentials in ferroelectric wte_2/wse_2 superlattices. *arXiv preprint arXiv:2209.04981* (2022).

[50] Woźniak, T., Junior, P. E. F., Seifert, G., Chaves, A. & Kunstmann, J. Exciton g factors of van der waals heterostructures from first-principles calculations. *Physical Review B* **101**, 235408 (2020).

[51] Maity, I., Maiti, P. K., Krishnamurthy, H. & Jain, M. Reconstruction of moiré lattices in twisted transition metal dichalcogenide bilayers. *Physical Review B* **103**, L121102 (2021).

[52] McGilly, L. J. *et al.* Visualization of moiré superlattices. *Nature Nanotechnology* **15**, 580–584 (2020).

[53] Rosenberger, M. R. *et al.* Twist angle-dependent atomic reconstruction and moiré patterns in transition metal dichalcogenide heterostructures. *ACS nano* **14**, 4550–4558 (2020).

[54] Wang, X. *et al.* Interfacial ferroelectricity in rhombohedral-stacked bilayer transition metal dichalcogenides. *Nature nanotechnology* **17**, 367–371 (2022).

[55] Weston, A. *et al.* Interfacial ferroelectricity in marginally twisted 2d semiconductors. *Nature nanotechnology* **17**, 390–395 (2022).

[56] Zhang, C. *et al.* Interlayer couplings, moiré patterns, and 2d electronic superlattices in mos_2/wse_2 hetero-bilayers. *Science advances* **3**, e1601459 (2017).

[57] Shabani, S. *et al.* Deep moiré potentials in twisted transition metal dichalcogenide bilayers. *Nature Physics* **17**, 720–725 (2021).

[58] Wu, F., Lovorn, T., Tutuc, E. & MacDonald, A. H. Hubbard model physics in transition metal dichalcogenide moiré bands. *Phys. Rev. Lett.* **121**, 026402 (2018). URL `https://link.aps.org/doi/10.1103/PhysRevLett.121.026402`.

[59] Regan, E. C. *et al.* Mott and generalized wigner crystal states in wse_2/ws_2 moiré superlattices. *Nature* **579**, 359–363 (2020).

[60] Jin, C. *et al.* Stripe phases in wse_2/ws_2 moiré superlattices. *Nature Materials* 1–5 (2021).

[61] Zhang, Z. *et al.* Flat bands in twisted bilayer transition metal dichalcogenides. *Nature Physics* **16**, 1093–1096 (2020).

[62] Li, H. *et al.* Imaging moiré flat bands in three-dimensional reconstructed wse_2/ws_2 superlattices. *Nature materials* **20**, 945–950 (2021).

[63] Wang, L. *et al.* Correlated electronic phases in twisted bilayer transition metal dichalcogenides. *Nature materials* **19**, 861–866 (2020).

[64] Wu, F., Lovorn, T., Tutuc, E., Martin, I. & MacDonald, A. Topological insulators in twisted transition metal dichalcogenide homobilayers. *Physical review letters* **122**, 086402 (2019).

[65] Cai, J. *et al.* Signatures of fractional quantum anomalous hall states in twisted mote2 bilayer. *arXiv preprint arXiv:2304.08470* (2023).

[66] Lee, C.-H. *et al.* Atomically thin p–n junctions with van der waals heterointerfaces. *Nature nanotechnology* **9**, 676–681 (2014).

[67] Hsu, W.-T. *et al.* Tailoring excitonic states of van der waals bilayers through stacking configuration, band alignment, and valley spin. *Science advances* **5**, eaax7407 (2019).

[68] Barré, E. *et al.* Optical absorption of interlayer excitons in transition-metal dichalcogenide heterostructures. *Science* **376**, 406–410 (2022).

[69] Chen, H. *et al.* Ultrafast formation of interlayer hot excitons in atomically thin mos_2/ws_2 heterostructures. *Nature Communications* **7**, 12512 EP – (2016). URL `http://dx.doi.org/10.1038/ncomms12512`.

[70] Kim, J. *et al.* Observation of ultralong valley lifetime in wse_2/mos_2 heterostructures. *Science Advances* **3** (2017). URL `http://advances.sciencemag.org/content/3/7/e1700518`. `http://advances.sciencemag.org/content/3/7/e1700518.full.pdf`.

[71] Unuchek, D. *et al.* Valley-polarized exciton currents in a van der waals heterostructure. *Nature nanotechnology* **14**, 1104–1109 (2019).

[72] Sun, Z. *et al.* Excitonic transport driven by repulsive dipolar interaction in a van der waals heterostructure. *Nature photonics* **16**, 79–85 (2022).

[73] Yu, H., Liu, G.-B., Gong, P., Xu, X. & Yao, W. Dirac cones and dirac saddle points of bright excitons in monolayer transition metal dichalcogenides. *Nat Commun* **5** (2014). URL `http://dx.doi.org/10.1038/ncomms4876`.

[74] Wu, F., Lovorn, T. & MacDonald, A. H. Topological exciton bands in moiré heterojunctions. *Phys. Rev. Lett.* **118**, 147401 (2017). URL https://link.aps.org/doi/10.1103/PhysRevLett.118.147401.

[75] Wu, F., Lovorn, T. & MacDonald, A. Theory of optical absorption by interlayer excitons in transition metal dichalcogenide heterobilayers. *Physical Review B* **97**, 035306 (2018).

[76] Yu, H., Liu, G.-B., Tang, J., Xu, X. & Yao, W. Moiré excitons: From programmable quantum emitter arrays to spin-orbit–coupled artificial lattices. *Science Advances* **3** (2017). URL http://advances.sciencemag.org/content/3/11/e1701696. http://advances.sciencemag.org/content/3/11/e1701696.full.pdf.

[77] Yu, H., Wang, Y., Tong, Q., Xu, X. & Yao, W. Anomalous light cones and valley optical selection rules of interlayer excitons in twisted heterobilayers. *Phys. Rev. Lett.* **115**, 187002 (2015). URL https://link.aps.org/doi/10.1103/PhysRevLett.115.187002.

[78] Yu, H., Liu, G.-B. & Yao, W. Brightened spin-triplet interlayer excitons and optical selection rules in van der waals heterobilayers. *2D Materials* **5**, 035021 (2018).

[79] Naik, M. H. *et al.* Intralayer charge-transfer moiré excitons in van der waals superlattices. *Nature* **609**, 52–57 (2022).

[80] Wang, X. *et al.* Intercell moiré exciton complexes in electron lattices. *Nature Materials* 1–6 (2023).

[81] Jérome, D., Rice, T. & Kohn, W. Excitonic insulator. *Physical Review* **158**, 462 (1967).

[82] Ma, L. *et al.* Strongly correlated excitonic insulator in atomic double layers. *Nature* **598**, 585–589 (2021).

[83] Chen, D. *et al.* Excitonic insulator in a heterojunction moiré superlattice. *Nature Physics* **18**, 1171–1176 (2022).

[84] Gu, J. *et al.* Dipolar excitonic insulator in a moiré lattice. *Nature Physics* **18**, 395–400 (2022).

[85] Zhang, Z. *et al.* Correlated interlayer exciton insulator in heterostructures of monolayer wse_2 and moiré ws_2/wse_2. *Nature Physics* **18**, 1214–1220 (2022).

[86] Tan, Q. *et al.* Layer-dependent correlated phases in wse2/mos2 moiré superlattice. *Nature Materials* 1–7 (2023).

[87] Zhang, Y.-H., Sheng, D. & Vishwanath, A. Su (4) chiral spin liquid, exciton supersolid, and electric detection in moiré bilayers. *Physical review letters* **127**, 247701 (2021).

[88] Castellanos-Gomez, A. *et al.* Deterministic transfer of two-dimensional materials by all-dry viscoelastic stamping. *2D Materials* **1**, 011002 (2014). URL `http://stacks.iop.org/2053-1583/1/i=1/a=011002`.

[89] Zomer, P., Guimarães, M., Brant, J., Tombros, N. & Van Wees, B. Fast pick up technique for high quality heterostructures of bilayer graphene and hexagonal boron nitride. *Applied Physics Letters* **105**, 013101 (2014).

[90] Brotons-Gisbert, M. *et al.* Spin–layer locking of interlayer excitons trapped in moiré potentials. *Nature Materials* **19**, 630–636 (2020).

[91] Baek, H. *et al.* Highly energy-tunable quantum light from moiré-trapped excitons. *Science advances* **6**, eaba8526 (2020).

[92] Saffman, M., Walker, T. G. & Mølmer, K. Quantum information with rydberg atoms. *Rev. Mod. Phys.* **82**, 2313–2363 (2010). URL https://link.aps.org/doi/10.1103/RevModPhys.82.2313.

[93] Brunner, K., Abstreiter, G., Böhm, G., Tränkle, G. & Weimann, G. Sharp-line photoluminescence and two-photon absorption of zero-dimensional biexcitons in a gaas/algaas structure. *Physical review letters* **73**, 1138 (1994).

[94] Sek, G., Musiał, A., Podemski, P. & Misiewicz, J. On the applicability of a few level rate equation model to the determination of exciton versus biexciton kinetics in quasi-zero-dimensional structures. *Journal of Applied Physics* **108**, 033507 (2010).

[95] Schinner, G. J. *et al.* Confinement and interaction of single indirect excitons in a voltage-controlled trap formed inside double ingaas quantum wells. *Phys. Rev. Lett.* **110**, 127403 (2013). URL https://link.aps.org/doi/10.1103/PhysRevLett.110.127403.

[96] Larentis, S. *et al.* Large effective mass and interaction-enhanced zeeman splitting of k-valley electrons in $mose_2$. *Physical Review B* **97**, 201407 (2018).

[97] Atatüre, M., Englund, D., Vamivakas, N., Lee, S.-Y. & Wrachtrup, J. Material platforms for spin-based photonic quantum technologies. *Nature Reviews Materials* **3**, 38 (2018).

[98] Guo, H., Zhang, X. & Lu, G. Moiré excitons in defective van der waals heterostructures. *Proceedings of the National Academy of Sciences* **118**, e2105468118 (2021).

[99] Zhang, L. *et al.* Highly valley-polarized singlet and triplet interlayer excitons in van der waals heterostructure. *Physical Review B* **100**, 041402 (2019).

[100] Wang, T. *et al.* Giant valley-zeeman splitting from spin-singlet and spin-triplet interlayer excitons in $wse_2/mose_2$ heterostructure. *Nano Letters* (2019).

[101] Zhao, S. *et al.* Excitons in mesoscopically reconstructed moiré heterostructures. *Nature Nanotechnology* 1–8 (2023).

[102] Tan, L. B. *et al.* Interacting polaron-polaritons. *Physical Review X* **10**, 021011 (2020).

[103] Back, P., Zeytinoglu, S., Ijaz, A., Kroner, M. & Imamoğlu, A. Realization of an electrically tunable narrow-bandwidth atomically thin mirror using monolayer mose 2. *Physical review letters* **120**, 037401 (2018).

[104] Scuri, G. *et al.* Large excitonic reflectivity of monolayer $mose_2$ encapsulated in hexagonal boron nitride. *Physical review letters* **120**, 037402 (2018).

[105] Barachati, F. *et al.* Interacting polariton fluids in a monolayer of tungsten disulfide. *Nature nanotechnology* **13**, 906–909 (2018).

[106] Nagler, P. *et al.* Giant magnetic splitting inducing near-unity valley polarization in van der waals heterostructures. *Nature Communications* **8**, 1551 (2017). URL `https://doi.org/10.1038/s41467-017-01748-1`.

[107] Kennes, D. M. *et al.* Moiré heterostructures as a condensed-matter quantum simulator. *Nature Physics* **17**, 155–163 (2021).

[108] Allain, A., Kang, J., Banerjee, K. & Kis, A. Electrical contacts to two-dimensional semiconductors. *Nature materials* **14**, 1195–1205 (2015).

[109] Li, T. *et al.* Charge-order-enhanced capacitance in semiconductor moiré superlattices. *Nature Nanotechnology* **16**, 1068–1072 (2021).

[110] Popert, A. *et al.* Optical sensing of fractional quantum hall effect in graphene. *Nano Letters* **22**, 7363–7369 (2022).

[111] Huang, X. *et al.* Correlated insulating states at fractional fillings of the ws_2/wse_2 moiré lattice. *Nature Physics* **17**, 715–719 (2021).

[112] Foutty, B. A. *et al.* Tunable spin and valley excitations of correlated insulators in γ-valley moiré bands. *Nature Materials* 1–6 (2023).

[113] Miao, S. *et al.* Strong interaction between interlayer excitons and correlated electrons in wse_2/ws_2 moiré superlattice. *Nature communications* **12**, 3608 (2021).

[114] Liu, E. *et al.* Excitonic and valley-polarization signatures of fractional correlated electronic phases in a wse_2/ws_2 moiré superlattice. *Physical Review Letters* **127**, 037402 (2021).

[115] Wang, X. *et al.* Light-induced ferromagnetism in moiré superlattices. *Nature* **604**, 468–473 (2022).

[116] Brotons-Gisbert, M. *et al.* Moiré-trapped interlayer trions in a charge-tunable $wse_2/mose_2$ heterobilayer. *Phys. Rev. X* **11**, 031033 (2021).

[117] Liu, E. *et al.* Signatures of moiré trions in $wse_2/mose_2$ heterobilayers. *Nature* **594**, 46–50 (2021).

[118] Wang, X. *et al.* Moiré trions in $mose_2/wse_2$ heterobilayers. *Nature Nanotechnology* 1–6 (2021).

[119] Tong, Q., Chen, M., Xiao, F., Yu, H. & Yao, W. Interferences of electrostatic moiré potentials and bichromatic superlattices of electrons and excitons in transition metal dichalcogenides. *2D Materials* **8**, 025007 (2020).

[120] Kim, K. *et al.* van der waals heterostructures with high accuracy rotational alignment. *Nano letters* **16**, 1989–1995 (2016).

[121] Baek, H. *et al.* Optical read-out of coulomb staircases in a moiré superlattice via trapped interlayer trions. *Nature Nanotechnology* 1–7 (2021).

[122] Campbell, A. J. *et al.* Exciton-polarons in the presence of strongly correlated electronic states in a $mose_2/wse_2$ moiré superlattice. *npj 2D Materials and Applications* **6**, 79 (2022).

[123] Lu, X. *et al.* Optical initialization of a single spin-valley in charged wse_2 quantum dots. *Nature nanotechnology* (2019).

[124] Smoleński, T. *et al.* Tuning valley polarization in a wse_2 monolayer with a tiny magnetic field. *Physical Review X* **6**, 021024 (2016).

[125] Yong, C.-K. *et al.* Valley-dependent exciton fine structure and autler–townes doublets from berry phases in monolayer $mose_2$. *Nature materials* **18**, 1065–1070 (2019).

[126] Wang, G. *et al.* Colloquium: Excitons in atomically thin transition metal dichalcogenides. *Reviews of Modern Physics* **90**, 021001 (2018).

[127] Zhang, L. *et al.* Van der waals heterostructure polaritons with moiré-induced nonlinearity. *Nature* **591**, 61–65 (2021).

[128] Tang, Y. *et al.* Tuning layer-hybridized moiré excitons by the quantum-confined stark effect. *Nature Nanotechnology* **16**, 52–57 (2021).

[129] Kresse, G. & Furthmüller, J. Efficient iterative schemes for ab initio total-energy calculations using a plane-wave basis set. *Physical review B* **54**, 11169 (1996).

[130] Perdew, J. P., Burke, K. & Ernzerhof, M. Generalized gradient approximation made simple. *Physical review letters* **77**, 3865 (1996).

[131] Klimeš, J., Bowler, D. R. & Michaelides, A. Van der waals density functionals applied to solids. *Physical Review B* **83**, 195131 (2011).

[132] Yu, J. *et al.* Observation of double indirect interlayer exciton in wse_2/ws_2 heterostructure. *Optics express* **28**, 13260–13268 (2020).

[133] Paradisanos, I. *et al.* Efficient phonon cascades in wse_2 monolayers. *Nature communications* **12**, 1–7 (2021).

[134] Slobodkin, Y. *et al.* Quantum phase transitions of trilayer excitons in atomically thin heterostructures. *Physical Review Letters* **125**, 255301 (2020).

[135] Kremser, M. *et al.* Discrete interactions between a few interlayer excitons trapped at a $mose_2$–wse_2 heterointerface. *npj 2D Materials and Applications* **4**, 1–6 (2020).

[136] Schmitt-Rink, S., Chemla, D. & Miller, D. A. Theory of transient excitonic optical nonlinearities in semiconductor quantum-well structures. *Physical Review B* **32**, 6601 (1985).

[137] Rochat, G. *et al.* Excitonic bloch equations for a two-dimensional system of interacting excitons. *Physical Review B* **61**, 13856 (2000).

[138] Gu, J. *et al.* Enhanced nonlinear interaction of polaritons via excitonic rydberg states in monolayer wse_2. *Nature communications* **12**, 1–7 (2021).

[139] Tornatzky, H., Kaulitz, A.-M. & Maultzsch, J. Resonance profiles of valley polarization in single-layer mos_2 and $mose_2$. *Physical review letters* **121**, 167401 (2018).

[140] Kim, J. *et al.* Ultrafast generation of pseudo-magnetic field for valley excitons in wse_2 monolayers. *Science* **346**, 1205–1208 (2014). URL `http://science.`

sciencemag.org/content/346/6214/1205. http://science.sciencemag.org/content/346/6214/1205.full.pdf.

[141] Sie, E. J. *et al.* Valley-selective optical stark effect in monolayer ws_2. *Nat Mater* **14**, 290–294 (2015). URL http://dx.doi.org/10.1038/nmat4156.

[142] Mouri, S. *et al.* Nonlinear photoluminescence in atomically thin layered wse 2 arising from diffusion-assisted exciton-exciton annihilation. *Physical Review B* **90**, 155449 (2014).

[143] Kumar, N. *et al.* Exciton-exciton annihilation in mose 2 monolayers. *Physical Review B* **89**, 125427 (2014).

[144] Sun, D. *et al.* Observation of rapid exciton–exciton annihilation in monolayer molybdenum disulfide. *Nano letters* **14**, 5625–5629 (2014).

[145] Yu, Y. *et al.* Fundamental limits of exciton-exciton annihilation for light emission in transition metal dichalcogenide monolayers. *Physical Review B* **93**, 201111 (2016).

[146] Hoshi, Y. *et al.* Suppression of exciton-exciton annihilation in tungsten disulfide monolayers encapsulated by hexagonal boron nitrides. *Physical Review B* **95**, 241403 (2017).

[147] Kulig, M. *et al.* Exciton diffusion and halo effects in monolayer semiconductors. *Physical review letters* **120**, 207401 (2018).

[148] Zhu, H. *et al.* Interfacial charge transfer circumventing momentum mismatch at two-dimensional van der waals heterojunctions. *Nano letters* **17**, 3591–3598 (2017).

[149] Montblanch, A. R.-P. *et al.* Confinement of long-lived interlayer excitons in ws2/wse2 heterostructures. *Communications Physics* **4**, 119 (2021).